UNIVERSITY COLLEGE LONDON

Theoretical Investigations of Surface Chemistry in Space

Davy Alain Adriaens

Thesis submitted to University College London
in the Faculty of Mathematical and Physical
Sciences for the degree of Doctor of Philosophy,
June 2009

After 3.5 years of research, I finally feel like
I contributed my one grain of sand to the Sahara Desert

It is obvious that this piece of work would never have come to be what it is without the help of so many colleagues, friends, random people who just happened to pass in my life. I would like to thank them all for being who they are, for having been in my life.

Many thanks to my supervisors Richard Catlow and Wendy Brown, and my friend and post-doctoral help Fedor Goumans.

Thanks to Crystal know-it-all's Christine Bailey, Adrian Wander, Barry Searle, Nic Harrison, Furio Corà, Eliska Krizkova and Sanda Botiş, and the Torino and Daresbury Crystal teams, computer genii Sarah Wilsey, Helen Tsui, Duncan Tooke, Ian Bush and Simon Clifford.

Thanks to my chemistry colleagues Clare Bishop, Bevan Sharma, Numaan Ahmed, Miguel José Mora Fonz, Keith Butler, Sheena Dungey, Martina Miskufova, Alan Lobo, Jamie Christie, John Edridge, Daren Burke, Jadranka Butorac, Emma Wilson, Kati Freimann, Farahjabeen Islam, Rosie Coates, Kate Woodhead, Andreas Kafizas, Madeeha Uppal, Sasja Steenvoorde, Elinor Dunn, Naomi Ruth Woolnough, Hitesh Bhalla, Elspeth Latimer, Milena Wobbe, Stephen Potts, Luke Thomas, Luanne Thomas, Naima Narband, Jenny Noble, Saima Haider, Simon Titley and Caroline Knapp, and my colleagues and friends in Belgium David Van den Daele, Karel Aelvoet, Michel Van Overschelde, Kris De Gussem.

Many thanks also to my astronomy and physics colleagues Serena Viti, Estelle Bayet, Magda Vasta, Julia Roberts, Ruth Ballesteros, Will Whyatt, and thanks to the Science Ambassadors team Jayne Shaw, Jodie Kirk, Dewi Lewis and David Rowley.

And thanks to some people just for being there: Carlijn, Olivia, Patty, Emily, Simon, Jessica, Wim, Walter, Ronny, Tim, Robyn, Caitlin, Jen, Katya, Joe, Emma, Ewelina, Cherry, Nancy, Elisaveth, Antonis, Bartek, Tinga, Olivier, Alex, Celine, Becky, Vera, Els and Betty.

Most thanks obviously go to my parents, who believed in me and supported me throughout the entire period.

Finally I would like to acknowledge the computer clusters which were used in this research: HPCx, SCARF, C^3, Columbus, Magellan, Bragg, and Faraday.

For Lien and Sam

I, Davy Alain Adriaens, confirm that the work presented in this thesis is my own. Where information has been derived from other sources, I confirm that this has been indicated in the thesis.

London, 8 June 2009

Abstract

In this Thesis, computational models for carbonaceous dust grains were examined and compared to known experimental data. Different formation routes of molecules, important to the astrochemical evolution of the universe, have been investigated and their relative energies were analysed with respect to the harsh conditions in interstellar dark clouds of extremely low pressure (10^{-17} bar) and temperature (10 – 20 K).

Dust grains are present in the universe, and evidence shows they are siliceous or carbonaceous, possible with an icy mantle surrounding the core. In this research, only carbonaceous surfaces were examined. Two models were used to represent polycyclic, aromatic carbonaceous surfaces: coronene, $C_{24}H_{12}$, representing a relatively small hydrocarbon, and graphene – a single graphite sheet – which represents an extended carbonaceous surface.

The main aims of this Thesis were to examine the validity of computationally modelled astrochemical reactions and to investigate the catalytic effect of dust grain surfaces on these reactions. Several formation reactions were examined, including water, methanol and carbonyl sulfide formation. The abundance of these molecules in dark molecular clouds cannot be explained by solely considering gas phase type reactions, and the influence that the carbonaceous surfaces have on these reactions was investigated in order to examine any catalytic effect that they may have.

Index

Chapter 1: The Chemical Universe 1

1.1. Molecules in space 2

1.1.1. Detection of molecules in space 2

1.1.2. Dust grains 5

1.1.3. Modelling the chemical evolution of the ISM 8

1.2. Chemistry in space 10

1.2.1. Reaction mechanisms 11

1.2.2. Adsorption 13

1.2.3. Formation of molecules 13

1.2.4. Hydrogen gas 15

1.3. References 18

Chapter 2: Computational Methods 21

2.1. Quantum Chemistry: WFT and DFT 23

2.1.1. WFT and DFT: ground states 23

2.1.2. Basis sets 31

2.1.3. Transition states 34

2.1.3.a. Transition state theory and reaction rates 34

Transition states and potential energy surfaces 34

Reaction rates 37

2.1.3.b. Algorithms to find transition states 39

Algorithms: chain algorithms 39

Algorithms: hill-walking algorithms 44

2.2. Computer codes 45

2.2.1. Gaussian03 and Molpro 46

2.2.2. Crystal06 47

2.2.3. Functionals 49

2.3. Summary 48

2.4. References 50

Chapter 3: Water 52

3.1. Astronomical importance of water 53

3.1.1. Introduction and importance of water 53

3.1.2. Potential formation reactions of water 56

3.2. Previous work 60

3.3. Validation and benchmarking 66

3.3.1. Methodology 66

3.3.2. Validation and benchmarking 66

3.4. Results and discussion 68

3.4.1. Adsorption on the surfaces 68

3.4.2. Water formation reactions 71

3.4.3. O + H → OH, OH + H → H_2O 74

3.4.4. OH + H_2 → H_2O + H 77

3.5. Astrochemical implications 79

3.6. Conclusions 83

3.7. References 85

Chapter 4: Methanol 87

4.1. Astronomical importance of methanol 88

4.1.1. Importance of methanol, formaldehyde and CO 88

4.1.2. Abundances and possible reactions 90

4.1.3. Previous work 91

4.2. Validation and benchmarking 94

4.3. Results and discussion 98

4.3.1. Potential formation reactions of methanol from CO 98

4.3.2. Reactions 100

CO + H → CHO 101

CH_2O + H → CH_3O 104

CH_2O + H → CH_2OH 105

Comparison with silica catalysis 109

4.4. Conclusions 110

4.5. References 113

Chapter 5: Carbonyl sulphide 114

5.1. Astronomical importance of OCS 115

5.1.1. Importance of OCS and astronomical abundances of its reactants 115

5.1.2. Potential formation reactions of OCS 118

5.2. Previous work 120

5.3. Validation and benchmarking 125

5.3.1. Methodology 125

5.3.2. Validation and benchmarking 125
5.4. Results and discussion 127
5.4.1. CO + S 130
5.4.2. CO + HS 132
5.4.3. CS + O 136
5.4.4. CS + OH 139
5.4.5. Comparison with CO_2 formation reactions 142
5.5. Astrochemical implications 145
5.6. Conclusions 148
5.7. References 150
Chapter 6: Conclusions and future work 152
6.1. Conclusions 153
6.2. Future Work 155
6.3 References 157

List of Figures

Chapter 1: The Chemical Universe

Figure 1.1: Molecular cloud B68, a dust cloud in the ISM (image courtesy of NASA). 6

Figure 1.2: Average extinction curve of the ISM. The curve can be deconvoluted into three different absorption peaks, related to the size of the absorbing particles. 6

Figure 1.3: A sample dust grain particle recovered by the StarDust mission. 7

Figure 1.4: Cartoon showing the dust grain composition. 7

Figure 1.5: The Eley Rideal mechanism. (a) One atom adsorbs onto a surface, (b) reacts with another atom passing by and forms a molecule, which then desorbs (c). 11

Figure 1.6: The Langmuir Hinshelwood mechanism. (a) Two atoms adsorb onto a surface, (b) diffuse across it and form a molecule which then desorbs (c). 12

Chapter 2: Computational Methods

Figure 2.1: 1D potential energy surfaces, e.g. when stretching a chemical bond. The left hand figure shows a Lennard-Jones type function; the red curve is the approximate parabola describing a harmonic approach. The frequency of this bond is related to the broadness of this parabola. On the right hand side is the potential energy surface of a transition state reaction coordinate. The absolute value of the imaginary frequency is also related to the broadness of the approximating parabola. 37

Figure 2.2: Energy vs. image number plot of a sample NEB calculation. The true and spring forces are shown for the highest energy image. Figure courtesy of Christine Bailey. 42

Figure 2.3: The molecule coronene, $C_{24}H_{12}$, which was used as a model for PAHs in this research. Carbon is black; hydrogen is white. 47

Figure 2.4: A 2D cell (the top left parallelogram) is changed into a 3x2 supercell (the top right combination of parallelograms). The cell is multiplied, after which the cells are joined together to

form a new, larger, cell (the bottom, larger parallelogram). The creation of this supercell will decrease the interaction of any atom with its next-cell image. 48

Figure 2.5: CO is added onto a graphene sheet – graphene carbon is depicted as the grey spheres, CO carbon is brown, oxygen is red. The left hand picture shows one CO molecule per unit cell of graphene. Clearly the CO molecules interact with each other. In the right hand picture, one CO molecule is added per 3x3 supercell of graphene, increasing the distance between the CO molecules and thus decreasing the interaction between adjacent CO molecules. 48

Chapter 3: Water

Figure 3.1: Importance of the H_3^+ ion (and ions in general) in the ISM. 56

Figure 3.2: Part of the chemical network for reactions possibly involved in water formation. Reactions can proceed in the gas phase or on a surface. 59

Figure 3.3: DFT energies vs. CCSD(T) energies for reactions involved in water formation, as shown in Figure 3.1 and Table 3.2. Axis values are in kJ mol^{-1}. 67

Figure 3.4: Adsorption geometries of water on the surfaces. Left: water on coronene, right: water on graphene. 71

Figure 3.5: Adsorption geometries of hydroxyl on the surfaces. Left: hydroxyl on coronene, right: hydroxyl on graphene. 71

Figure 3.6: Ozone formation from O_2 + O. Ozone is the lowest point on the singlet curve (left). The energy of O_2 + O is set to zero at infinite distance (right, quintuplet line). 74

Figure 3.7: Reaction energy profile for H + OH on a coronene surface. 76

Figure 3.8: Chemisorbed oxygen on coronene, forming an epoxide ring with two coronene carbon atoms. 76

Figure 3.9: Langmuir Hinshelwood transition state for the reaction of H_2 + OH on coronene. 79

Figure 3.10: Temperature dependency of the Langmuir Hinshelwood pre-exponential factor and reaction rate constant for the reaction $OH + H_2 \rightarrow H_2O + H$ on a coronene surface. 81

Figure 3.11: Temperature dependency of the Eley Rideal pre-exponential factor and reaction rate constant for the reaction $OH + H_2 \rightarrow H_2O + H$ on a coronene surface. 81

Figure 3.12: The ratio of reaction vs. desorption for LH (left hand axis) and ER (right hand axis) mechanisms, as a function of the temperature. 83

Chapter 4: Methanol

Figure 4.1: Possible hydrogenation pathways of CO to formaldehyde and methanol, both in the gas phase and on a surface. 90

Figure 4.2: PW1K vs. CCSD(T) reaction energies for the methanol formation reactions, showing agreement between both methods. 95

Figure 4.3. Reaction pathway to form methanol via formaldehyde from CO. (1a) to (1f) (top) shows the Eley Rideal mechanism. First CO adsorbs on the graphite surface, after which hydrogen in the gas phase reacts with CO. Once formaldehyde is formed, two possible reaction pathways are shown. (2a) to (2j) (bottom) shows the Langmuir Hinshelwood mechanism. CO adsorbs on the graphite surface. Physisorbed hydrogen (physisorption shown explicitly) then successively hydrogenates CO. Again, from formaldehyde on, two possible reaction pathways are shown. 97

Figure 4.4: Uncharged hydrogenation pathway of CO to formaldehyde and methanol, both in the gas phase and on a surface. 100

Figure 4.5: Reaction of $H + CO_{ads}$ to give CHO_{ads}. Top: Langmuir Hinshelwood mechanism; bottom: Eley Rideal mechanism. Shown from left to right are the initial state, the transition state, and the final state geometries. Graphene is grey, carbon is brown, oxygen is red and hydrogen is white. For clarity, the graphene surface is shown terminated; the calculations were performed on 2D periodic surfaces. 103

Figure 4.6: Surface reaction of $CH_2O + H \rightarrow CH_3O$. From left to right: the initial state geometry (formaldehyde plus a distant hydrogen atom), the transition state geometry, and the final state geometries (the methoxy radical adsorbed sideways on the graphene surface). The surface is

shown terminated for clarity; the calculations were performed on 2D periodic surfaces. Also for clarity, the graphene carbon atoms are grey, the formaldehyde / methoxy carbon atom is brown. Oxygen is red and hydrogen is white. 105

Figure 4.7: Relative energies (in kJ mol^{-1}) of formaldehyde reacting with a hydrogen atom to give the hydroxyl methyl radical. The full line shows the NEB reaction energies for the gas phase reaction; the dotted line is the surface catalysed NEB pathway. Figures 4.8 and 4.9 show the geometries corresponding to the initial, transition state and final energies. 106

Figure 4.8: Gas phase geometries of the reaction $CH_2O + H \rightarrow CH_2OH$. Shown from left to right: the initial geometry, the transition state geometry, and the final geometry. Carbon is grey, oxygen is red, hydrogen is white. 107

Figure 4.9: Surface catalysed formation of CH_2OH. The geometries shown are, from left to right: the initial geometry, the transition state geometry, and the final geometry. For clarity carbon is grey when it belongs to the graphene sheet, brown when it is part of the reactant. Oxygen is red, hydrogen is white. 107

Figure 4.10: π and π*-orbitals of formaldehyde (in the gas phase). 108

Chapter 5: Carbonyl Sulfide

Figure 5.1: The studied reaction pathways to OCS formation, starting from CO and H_2S photo-dissociation products (left hand side), and from CS and H_2O photo-dissociation products (right hand side). 120

Figure 5.2: Gas phase OCS formation from CO + S. The full line shows ^{3}OCS formation from ^{3}S and CO; the dotted line shows the calculated energy (in kJ mol^{-1}) of $^1S + CO \rightarrow {}^1OCS$. The energy of ^{3}S + CO at infinite distance is set to 0 kJ mol^{-1}. As the distance between C and S, shown on the horizontal axis, decreases (from right to left), the ground state (triplet) curve shows an activation barrier. It is only past this activation barrier (i.e. to its left) that the singlet state crosses the triplet state and becomes more favoured. 131

Figure 5.3: Three possible HSCO orientations are shown: from left to right *trans*-HSCO, *cis*-HSCO, *iso*-HSCO. Carbon is grey, oxygen is red, sulfur is yellow and hydrogen is white. 133

Figure 5.4: Reaction energy path for OCS formation from HS and CO. The energies shown on the graph are valid for the gas phase, ER and LH reactions. The effective values for the gas phase, LH and ER reactions are reported in Table 5.7. 134

Figure 5.5: Most stable orientations of *cis*-HSCO (left) and *trans*-HSCO (right) on a coronene surface.

Figure 5.6: Gas phase OCS formation from CS + O. The full line shows ^{3}OCS formation from ^{3}O and CS; the dotted line shows the calculated energy (in kJ mol^{-1}) of ^{1}O + CS → ^{1}OCS. The energy of ^{3}O + CS at infinite distance is set to 0 kJ mol^{-1}. As the distance between C and O, shown on the horizontal axis, decreases (from right to left), the ground state (triplet) curve shows a submerged activation barrier. It is only past this activation barrier (i.e. to its left) that the singlet state crosses the triplet state and becomes more favoured. The inset shows a zoom-in of the transition state area, to show the submerged barrier. 136

Figure 5.7: Gas phase reaction energy path for OCS formation from CS and OH. The energies shown on the graph are valid for the gas phase, ER and LH reactions. The effective values for the gas phase, LH and ER reactions are reported in Table 5.10. 141

Figure 5.8: Gas phase reaction energy path for CX + Y reactions. Energies are reported in kJ mol^{-1}.. 143

Figure 5.9: Gas phase reaction energy path for CX +HY reactions. Energies are reported in kJ mol^{-1}.144

Figure 5.10: Temperature dependency of the ratio of reaction vs. desorption for the reactions shown in Table 5.11 (LH). 147

Figure 5.11: Temperature dependency of the ratio of reaction vs. desorption for the reactions shown in Table 5.12 (ER). 148

List of Tables

Chapter 1: The Chemical Universe

Table 1.1: Molecules, ions and radicals detected and positively identified in the ISM to date. This table is adapted from the NASA website. 4

Chapter 2: Computational Methods

Table 2.1: Formal scaling of the time required to converge the energy with respect to the system size, for different DFT and WFT methods. *DFT scaling depends on the functional used, but is generally about the same or better than HF. Currently, linear scaling methods for DFT are available for (very) large systems. 27

Table 2.2: Jacob's Ladder for density functionals. The variables column shows that on every level of the ladder, more variables are included, improving the DFT method but becoming computationally slower. 29

Chapter 3: Water

Table 3.1: Chemical reactions, involved in water and OH formation, which are thought to happen in the ISM. 57

Table 3.2: Observed abundances for species in the water formation pathway, in dark molecular clouds. CO, CO_2 and CH_3OH have been included for comparison purposes, as they are the most abundant molecules in ISM ices. CD = Column Density, Ab = Abundance relative to H_2. 60

Table 3.3: Ab initio CCSD(T) energies and DFT energies for both functionals used (PW1K, MPWB1K) in kJ mol^{-1}. The reactions shown are part of the water formation pathway in the gas phase, as shown in Figure 3.2. Overall DFT values are around 12 kJ mol^{-1} lower than the corresponding CCSD(T) values. 68

Table 3.4: Experimental adsorption energies for water and other relevant species, on different surfaces. 70

Table 3.5: Theoretical adsorption energies for the water system adsorbed on coronene and on graphene, calculated with the MPWB1K and the PW1K functional respectively. Comparison is also made with previous studies, both experimental and theoretical. 70

Table 3.6: Total gas phase reaction energies and activation barriers of reactions involved in water formation, calculated with the MPWB1K and the PW1K functionals. Energies are in kJ mol^{-1}, activation barriers are in italics below the reaction energies. All molecules and radicals involved are assumed to be in the ground state (triplet state for O_2 and O, doublet state for other radicals, singlet state for other molecules). 73

Table 3.7: Calculated reaction energies and activation barriers of the reaction $OH + H_2 \rightarrow H_2O + H$. Calculations were performed with the MPWB1K (coronene) and the PW1K (graphene) functionals. Energies are in kJ mol^{-1}, activation barriers are in italics below the reaction energies. Both Langmuir Hinshelwood (LH) and Eley Rideal (ER) mechanisms were considered. ΔE denotes the reaction energy, and $\Delta E^{\neq}$ denotes the activation energy. 79

Table 3.8: Reaction rate constants and pre-exponential factors for both Eley Rideal and Langmuir Hinshelwood type $OH + H_2 \rightarrow H_2O + H$ reactions on a coronene surface. 82

Chapter 4: Methanol

Table 4.1: Observed abundances for species in the methanol formation pathway, in dark molecular clouds. CO_2 and H_2O have been included for comparison purposes. CD = Column Density, Ab = Abundance relative to H_2. 90

Table 4.2: Reaction energies for the methanol formation reactions in the gas phase. CCSD(T) and PW1K calculations are shown, and all values are in kJ mol^{-1}. 94

Table 4.3: Experimental adsorption energies for CO, methanol, and relevant species, on different surfaces. 96

Table 4.4: Adsorption energies for the methanol system adsorbed on graphene, calculated with the PW1K functional in this study and compared to previously reported results. 96

Table 4.5: Gas phase reaction enthalpies for reactions involved in methanol formation, involving H_2 / kJ mol^{-1}. 99

Table 4.6: Gas phase reaction energies for the methanol formation reactions. PW1K calculations performed in the current research are shown and compared with previous theoretical and experimental results where possible. PW1K and QCISD values are gas phase results. Hiraoka's results involve solid formaldehyde and methanol. All values are in kJ mol^{-1}. 101

Table 4.7: Comparison of calculated reaction energies and activation barriers (in italics) between gas phase and graphene. Energies are in kJ mol^{-1}. 104

Chapter 5: Carbonyl Sulphide

Table 5.1: Measured and calculated relative abundances (R.A.) of OCS and relevant reaction products in TMC-1. The abundance is relative to that of H_2, ~4 × 10^4 molecules cm^{-3}. 118

Table 5.2: Energies for gas phase OCS formation from CX + Y, as reported by previous studies. All energies are reported in kJ mol^{-1}. The excitation from ^{1}OCS to ^{3}OCS in this table was calculated using the reported ^{3}S + CO energy and the fact that it was reported to be very close to the ^{3}OCS energy. 121

Table 5.3: Experimental and theoretical energies for gas phase OCS formation from CX + HY, as reported by previous studies. All energies are reported in kJ mol^{-1}. 123

Table 5.4: Gas phase reaction energies, activation barriers, excitation energies and formation enthalpies for the OCS system. Values in italics refer to activation barriers and all values are in kJ mol^{-1}. Comparison with high-level ab initio values and literature values are also included.
s.a. denotes a submerged activation barrier. no ts. Indicates that no transition state was found for this reaction. The energies in the CCCBDB column are experimental enthalpies at 0 K and include formation and excitation enthalpies. 126

Table 5.5: Calculated adsorption energies using DFT, for relevant species physisorbed on coronene, except for ^{1}S and ^{1}O which are chemisorbed. Comparison with experimental results was made where possible, however experimental data is mostly unavailable. Experimental data includes adsorption on HOPG and amorphous carbon (denoted ^{HOPG} and ^{aC}). Theoretical results are adsorption energies on HOPG or coronene-like PAHs such as ovalene (^{HOPG} and ^{PAH}). 129

Table 5.6: Gas phase reaction energies and barrier heights for the CO + ^{3}S → ^{3}OCS reaction. The energies are expressed in kJ mol^{-1}. 132

Table 5.7: Calculated reaction energies and barrier heights for the CO + HS reaction, forming each of the three HSCO intermediates. The energies are expressed in kJ mol^{-1}. Barrier heights are in italics.

**The trans- isomer is formed via an LH type reaction. 134

Table 5.8: Calculated reaction energies and barrier heights for the CS + ^{3}O → ^{3}OCS reaction. The energies are expressed in kJ mol^{-1}.

*All activation barriers are submerged. The values given for the gas phase formation are the complexation energy and the submerged activation barrier with respect to the starting products at infinite distance. 138

Table 5.9: Properties of OCS and OCS transition states. Distances are in Å (1 Å = 10^{-10} m), energies are in kJ mol^{-1} and relative to ^{3}OCS. CO and CS are assumed to include a ^{3}S and a ^{3}O atom respectively. The geometries are gas phase geometries. 139

Table 5.10: Calculated reaction energies and barrier heights for the CS + OH reaction. The energies are expressed in kJ mol^{-1}. Barrier heights are in italics.

*The isomerisation of *trans*- to *cis*-HOCS is written as a LH reaction, as is the transition state for *cis*-HOCS dissociation. 141

Table 5.11: Reaction rates (r), pre-exponential factors (A) and activation barriers ($\Delta E^{\neq}$) for Langmuir Hinshelwood type reactions. The reaction rates are dependent on the surface coverage θ_X of chemical species. 146

Table 5.12: Reaction rates (r), pre-exponential factors (A) and activation barriers ($\Delta E^{\neq}$) for Eley Rideal type reactions. The reaction rates are dependent on the surface coverage θ_X and the gas phase concentration [Y] of chemical species. 146

The Chemical Universe

Chapter 1

1.1. Molecules in space

1.1.1. Detection of molecules in space

Since ancient times humanity has been observing the universe. Our historical archives show that the Ancient Greeks observed a static, everlasting universe where only a few stars, named *πλανητών* (*planiton*), wandered through the background of eternal stars. It was not until the Age of Enlightenment that it slowly occurred to scientists in Europe that not the earth, but the Sun, was a more likely candidate to be the centre of the universe. Scientists then came to realise that our Sun was just another star, which meant that stars were built up from the same material as the Sun. With the Age of Enlightenment came inventions including the microscope (1595) and the telescope (in 1608), both of which have increased our knowledge and understanding on a microscopic and macroscopic level. Since these discoveries, science has progressed to new heights, creating space telescopes covering a very wide range of wavelengths, and electron microscopes and scanning tunnelling microscopes able to show details on molecular and atomic levels. These progressions have led to more perfected and detailed theories about the physics of both very small and very large systems. Astronomical scientists obtain new data on a daily basis, attempting to fit theories of stellar evolution and planet formation to what is observed (1, 2).

Stars produce energy by fusing lighter nuclei together into heavier nuclei. The energy barrier to fusion is overcome by the star's own gravity, and the most abundant fusion process is the fusion of hydrogen into deuterium, tritium, helium-3 and helium-4. This process, called the proton-proton chain, happens in every star and is the primary source of its energy production (3, 4). Atoms like H and He have been discovered in stellar systems like the Sun – helium is named after the Greek (*Ήλιος*; *elios*) and the Roman (*Helios*) words for Sun (3). Fusing elements into heavier elements up to iron produces energy, however not all the fusion processes for different atoms are entirely understood.

Astrochemistry originally focussed on the detection of atoms. More recently it shifted towards molecular astronomy, which became possible after the introduction of radio and infrared telescopes, including satellitic telescopes which do not suffer from earthly noise. The object of interest consequently shifted from stars to the region between the stars: the interstellar medium (ISM). To date, over 150 molecules present in the ISM (shown in Table 1.1) have been detected and identified by infrared, visual and ultraviolet spectroscopy. Most of these molecules are relatively simple from a chemical viewpoint, the largest being only 13 atoms in size. Non-detection of larger molecules does not necessarily imply these molecules are absent. Many other techniques, available to laboratory chemists, cannot be applied to astronomy, which makes the assignment of detected spectral lines exclusively to one molecule either very hard or impossible.

For some of the detected molecules, gas phase chemical reactions under ISM conditions cannot account for the abundance, depending on the location in the ISM. Both pressure and temperature in the ISM vary strongly depending on the location and the proximity to stars, and the ISM is usually broken down into separate regions according to the pressure and temperature. The maximum pressure in the ISM is very low, around 10^{-9} bar (i.e. 10^{12} particles m^{-3}) in molecular clouds, and less than this value in other regions (down to $<10^{9}$ particles m^{-3} in diffuse clouds). The temperature extends over a wide range as well, from over 10,000 K in the warm neutral medium and over 10^{7} K in the coronal gas, down to as low as 10 – 20 K in dense molecular clouds. It is the dense molecular clouds on which this research is focussed.

A dense molecular cloud is the region in space where stars are formed, and the molecules present are very important for this process since they are capable of absorbing and re-emitting the energy that the proto-star produces upon formation. These clouds are of extremely low temperatures (10 to 20 K) and pressure (as low as 10^{-17} bar; 10^{4} particles cm^{-3}). As a molecular cloud collapses to form a proto-star, the collapsing gas releases gravitational potential energy as heat and radiation. The proto-star which is then formed will reach a temperature hot enough for the internal pressure to stop any further gravitational collapse. At this point, molecules present around the proto-star can absorb and radiate the energy via rotational and vibrational excitation, as well as via

Table 1.1: Molecules, ions and radicals detected and positively identified in the ISM to date. This table is adapted from the NASA website.[1]

H_2	N_2	H_3^+	C_3H_2	HC_5N
CO	CF^+	OCN^-	CH_2CN	C_6H
CSi	PO	HCP	H_2COH^+	C_6H^-
CP	H_2O	CCP	C_4Si	CH_3COOH
CS	H_2S	NH_3	C_5	$HCOOCH_3$
NO	HCN	H_2CO	HNC_3	CH_2OHCHO
NS	HNC	H_2CS	C_4H	CH_3C_3N
SO	CO_2	C_2H_2	C_4H^-	H_2C_6
HCl	SO_2	HNCO	HCOCN	HC_6H
NaCl	MgCN	HNCS	CH_3OH	CH_2CHCHO
KCl	MgNC	H_3O^+	CH_3SH	CH_2CCHCN
AlCl	NaCN	SiC_3	C_2H_4	C_7H
AlF	N_2O	C_3S	HC_4H	NH_2CH_2CN
PN	NH_2	H_2CN	CH_3CN	CH_3OCH_3
SiN	OCS	C_3H	CH_3NC	CH_3CH_2CN
SiO	CH_2	HCCN	$HCONH_2$	CH_3CH_2OH
SiS	HCO	CH_3	HC_2CHO	CH_3C_4H
NH	C_3	C_2CN	HC_3NH^+	HC_7N
OH	C_2H	C_3O	HC_4N	C_8H
C_2	C_2O	$HCNH^+$	C_5N	CH_3CONH_2
CN	C_2S	$HOCO^+$	C_5H	C_8H^-
HF	AlNC	C_3N^-	H_2C_4	CH_3CHCH_2
FeO	HNO	CH_4	H_2CCNH	CH_3COCH_3
LiH	SiCN	SiH_4	H_2C_3O	$HOCH_2CH_2OH$
CH	N_2H^+	CH_2NH	CH_2CHOH	CH_3CH_2CHO
CH^+	SiNC	NH_2CN	C_2H_4O	CH_3C_5N
CO^+	SiC_2	CH_2CO	$HCOCH_3$	HC_9N
SO^+	HCO^+	HCOOH	CH_3CCH	CH_3C_6H
SH	HOC^+	HC_3N	CH_3NH_2	C_6H_6
O_2	HCS^+	HCCNC	CH_2CHCN	$HC_{11}N$

electronic excitation. Without these molecules, low-mass stars including our Sun cannot be formed. Molecular clouds can thus be seen as stellar nurseries, where stars are born. Before starbirth, dense molecular clouds have a very low temperature and pressure as mentioned before, and it is because of this low temperature that the relative amounts of certain molecules cannot be explained by gas

---

[1] Table adapted from http://en.wikipedia.org/wiki/List_of_molecules_in_interstellar_space and http://www-691.gsfc.nasa.gov/cosmic.ice.lab/interstellar.htm (as of 1 October 2008)

phase reactions alone. It is now widely accepted that dust grains, present in dark molecular clouds, can act as the necessary catalysts for H_2 formation, and other key molecules in certain environments, such as hot cores. Since atoms and molecules can agglomerate on a dust particle, some reactions are more likely to take place on dust particles, compared to in the gas phase. The work presented here will use model dust grains to study the formation of relevant molecules.

1.1.2. Dust grains

Around 1784, on a trip around the Cape of Good Hope, William Herschel noticed something he described as a "hole in the sky", where almost no stars were visible (5). The origin of this hole was unclear, until spectroscopic evidence showed that some form of dust was blocking out part of the starlight. A well known dust cloud, Barnard-68, is shown in Figure 1.1. These dust grain particles play an essential role in interstellar chemistry (6-8) and, even though the exact composition of the grains remains unknown, there is strong evidence that they are composed of carbonaceous or siliceous material (5, 7, 9).

In comparing the spectra of these stars with the spectra of similar stars, an extinction curve can be obtained (shown in Figure 1.2), directly related to the size of particles blocking out the light. Though still subject to much debate, deconvolution of this curve led to three distinct absorption peaks (see Figure 1.2, taken and modified from (6)). The first peak was around 1-3 μm^{-1} (3300 – 10,000 Å), and was assigned to a silicate core consisting of organic refractory mantle particles, shown as a dash-dot line in the figure. The second peak had a maximum around 4.6 μm^{-1} (around 2200 Å), but this peak is subject to much debate. Finally PAH particles are responsible for the extinction over 7 μm^{-1} (dotted line). It is now generally accepted that dust grain particles have a siliceous core or a carbonaceous core (or a combination thereof), and depending on the region they

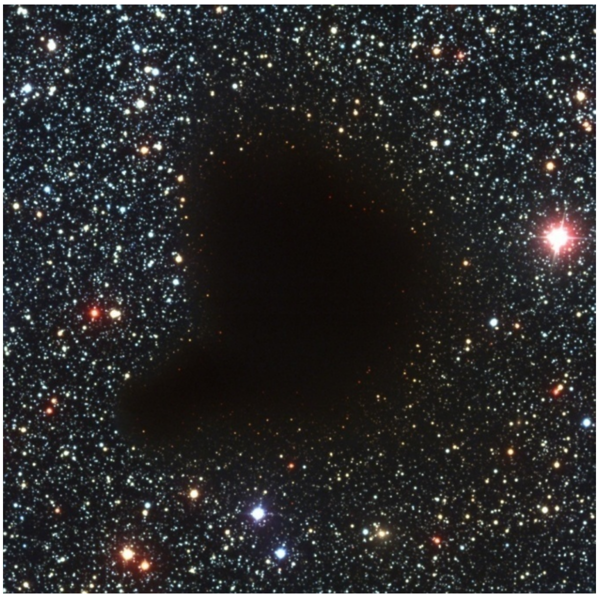

Figure 1.1: Molecular cloud B68, a dust cloud in the ISM (image courtesy of NASA, http://antwrp.gsfc.nasa.gov/apod/image/0803/barnard68_vlt_big.jpg)

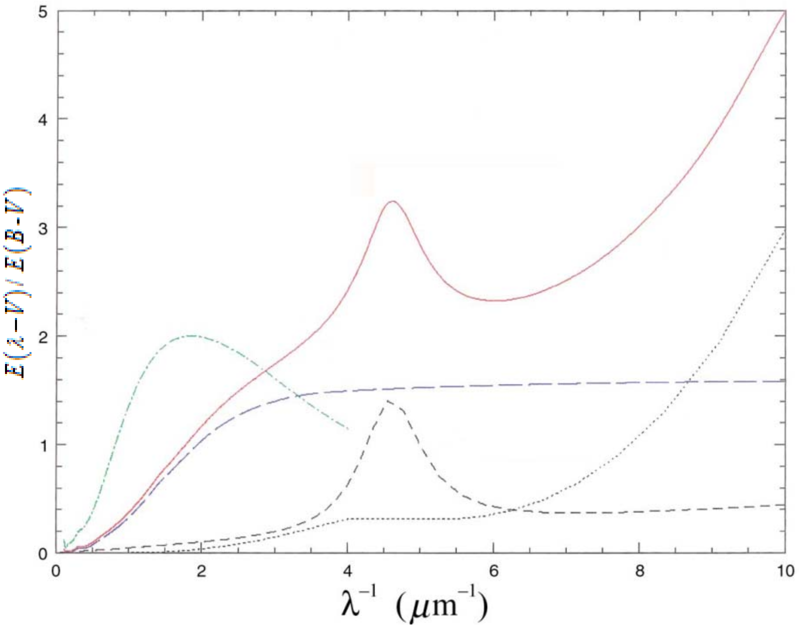

Figure 1.2: Average extinction curve of the ISM. The curve can be deconvoluted into three different absorption peaks (see text). The horizontal axis shows wavenumber (in μm^{-1}), the vertical axis shows the normalised extinction; i.e. the difference in extinction between the wavelength l and the V-band (1.8 μm^{-1}), with respect to the difference in extinction between the B-band (2.3 μm^{-1}) and the V-band.

may also be covered in an icy mantle consisting of H_2O, CO, CO_2 and CH_3OH molecules along with other trace species (5-7, 10).

Figure 1.3 shows a siliceous olivine (forsterite) dust grain particle which was recovered by NASA's StarDust mission (11), while Figure 1.4 shows a cartoon of the typical structure of an ISM dust grain particle as a core of siliceous and/or carbonaceous material, possibly covered in water ice.

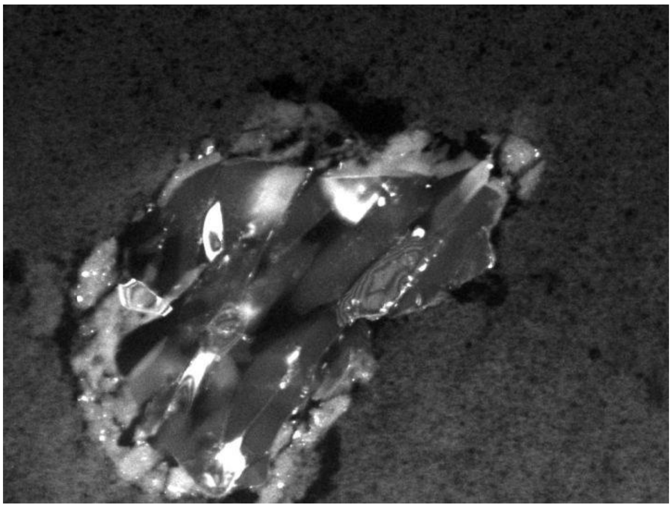

Figure 1.3: A sample dust grain particle recovered by the StarDust mission.

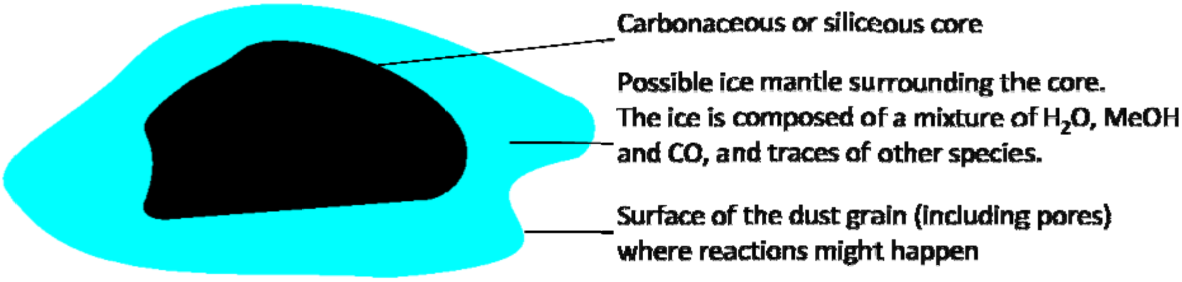

Figure 1.4: Cartoon showing the dust grain composition.

Many of the species found in the ISM, both in the gas phase and on dust grains, have too high an activation barrier for their formation to take place effectively in the gas phase. It is therefore believed that formation of these molecules may happen on the dust grain surface or in the icy mantle surrounding it.

Dust grains can be modelled as surfaces, and the importance of surface chemistry has already been shown for the H_2-formation problem (for example (12, 13) and references therein). H_2 is the most abundant molecule in the universe; however it cannot simply be formed by radiative recombination in the gas phase: as it is a homonuclear diatomic molecule, it has no dipole moment and as such it cannot radiate away any excess energy. The radiation which is present however, dissociates H_2 into hydrogen atoms. Since the amount of hydrogen molecules measured is significantly higher than predicted with gas phase models, and since it is relatively constant, hydrogen molecules must be formed via some other route.

Dust grain surfaces can interact with atoms and molecules in several ways to influence reactions, including the actual formation of molecules and the formation rate thereof. Four possible influences on any reaction can be distinguished. A dust grain may thermodynamically catalyse a chemical reaction, lowering the activation barrier and increasing the reaction rate. Species (atoms, molecules, ions) may accrete on the surface, which can increase the probability of an encounter. A dust grain can act as a third body absorbing excess energy produced upon reaction, hence reducing the possibility of newly formed molecules dissociating. And finally the surface can orient the adsorbates on the surface, increasing or decreasing the reaction rate. After H_2, which has been studied intensively, other molecules (14, 15) are also thought to be formed on the grain surface and experiments on models of these grains, and their impacts on astrochemistry under conditions relevant to the ISM, are currently being performed (for example (15-18)). It is the topic of this research to examine, theoretically, the influence of particular grain surfaces on the formation of certain molecules. Two models were used to represent carbonaceous dust grains: coronene and graphene. These models are described in Chapter 2.

1.1.3. Modelling the chemical evolution of the ISM

The research in this thesis examines grain surface reactions. The astrochemical models describing the evolution of the ISM and the dark clouds therein, are based on chemical networks. These networks involve calculating the concentrations of chemical species using reaction rates, occurring both in the gas phase and on a dust grain surface. This data used for astrochemistry is stored in large databases like the UMIST database for astrochemistry (UDFA) (19) and the NIST kinetics database (20). Reaction rates $k(T)$ are expressed as a function of the temperature *T* and are dependent on three parameters α, β, and γ, as shown in eq.(1.1). T_0 is dependent on the database used, e.g. UMIST uses 300 K, whereas NIST uses 298 K.

$$k(T) = \alpha \left(\frac{T}{T_0} \right)^{\beta} \exp\left(-\frac{\gamma}{k_B T} \right) \tag{1.1}$$

Equation (1.2) shows the reaction rate as it is usually written for chemical reactions.

$$k(T) = A \exp\left(-\frac{\Delta E^{\neq}}{RT} \right) \tag{1.2}$$

From these two equations, one can easily derive the straightforward connection between the astronomical rate parameters α, β and γ on the one hand, and the pre-exponential factor *A* and activation energy $\Delta E^{\neq}$ on the other (1.3). It is one of the main aims of this research to obtain the parameters *A* and $\Delta E^{\neq}$ for various reactions using quantum chemical calculations. N_A stands for Avogadro's constant.

$$\begin{aligned} A &= \alpha \left(\frac{T}{298} \right)^{\beta} \\ \Delta E^{\neq} &= \gamma N_A \end{aligned} \tag{1.3}$$

1.2. Chemistry in Space

The chemistry that occurs in the ISM region of space is different from earthly chemistry, most importantly because in the part of space relevant to this study there is almost no energy to help reactions overcome activation barriers. Reactions performed on earth are commonly performed at temperatures of 298 K (room temperature) or more, which is relatively high with respect to the temperature in dense molecular clouds, typically lower than 20 K. Moreover, the concentration in the ISM is close to losing its meaning, as typical number densities are of the order of 10^4 molecules cm^{-3} (or of the order of 10^{-17} mole dm^{-3}). Therefore any reactions happening in dense molecular clouds will have low, or absent, activation barriers, and some mechanism is required to accumulate species such that the density of molecules, and thus the reaction probability, increases.

As mentioned above, dust grains – more specifically dust grain surfaces – can adsorb molecules and atoms, such that the local density on the grain increases. The factors that play major roles in adsorbing these species are the structure of the grain and the adsorption energy. The surface structure is important since when a grain is more porous, it is possible that molecules reside in their pores, prolonging the time they spend on the grain. Representing a dust grain as a perfect surface is a good first approach. However, this model can be modified later on (21) to incorporate, for example, cavities. In this research, however, only perfect flat surfaces were used as a first approximation to dust grain surfaces. When compared to defective surfaces, the results obtained here are expected to give a lower boundary to the catalytic effect. In other words, the activation energy of the reactions happening on defective surfaces is expected to be lowered even further, and the adsorption energy is expected to be higher. This effect has already been observed in previous research (22, 23).

The adsorption energy of species on the grain surface should neither be too low, such that an adsorbed atom or molecule desorbs in a very short period of time, neither should it be too high, in order for the activation barrier required to react with another molecule or atom is low enough for the reaction to effectively occur. Moreover, a lower adsorption energy implies weaker bonding between the adsorbed species and the dust grain, which in turn implies it may be more difficult for this molecule, when it reacts, to transfer excess heat of formation to the dust grain surface.

1.2.1. Reaction Mechanisms

How exactly a reaction happens is a very difficult question to answer, and to get as wide a picture as possible, two different bimolecular reaction mechanisms, considered to be the extremes of a surface reaction, were studied. For a bimolecular reaction *A* + *B*, the Eley Rideal (ER) mechanism assumes *A* to be adsorbed on the surface, whereas *B* is in the gas phase. *B* reacts with *A* without *B* physisorbing during the reaction. The second mechanism is the Langmuir Hinshelwood (LH) mechanism, in which both *A* and *B* are physisorbed on, and are in thermal equilibrium with, the surface. Figures 1.5 and 1.6 [2] graphically show both ER and LH mechanisms for the formation of diatomic molecules.

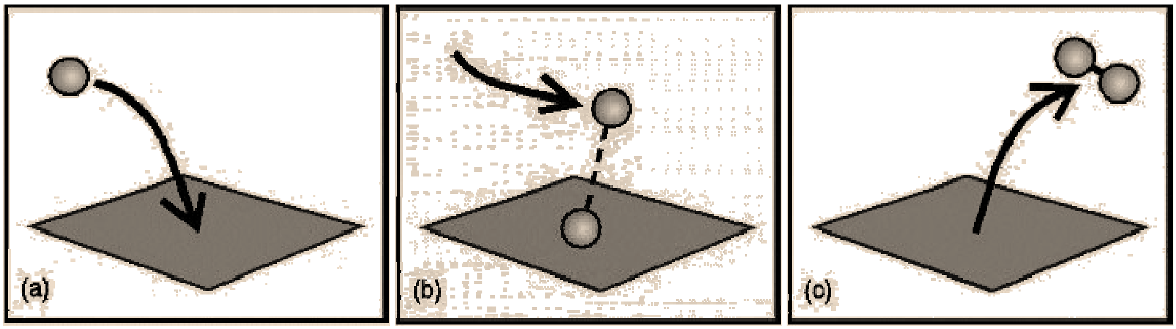

Figure 1.5: The Eley Rideal mechanism. (a) One atom adsorbs onto a surface, (b) reacts with another atom passing by and forms a molecule, which then desorbs (c).

---

[2] Figures showing ER and LH taken from the UCL Centre for Cosmic Chemistry and Physics website; courtesy of Dr Angela Wolff.

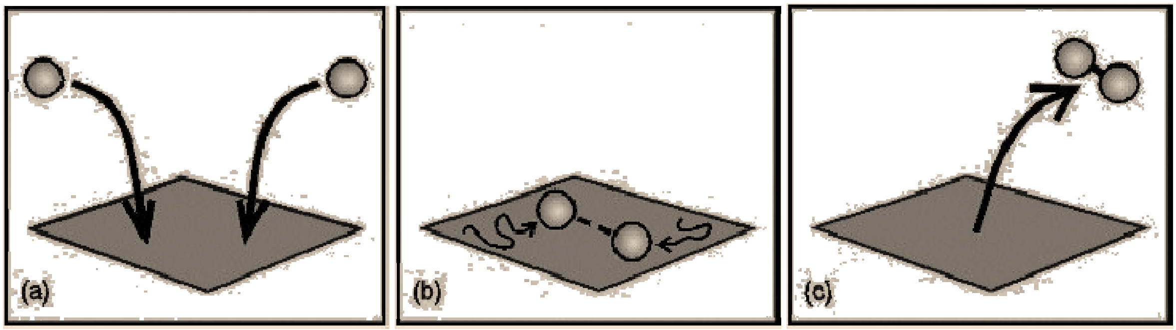

Figure 1.6: The Langmuir Hinshelwood mechanism. (a) Two atoms adsorb onto a surface, (b) diffuse across it and form a molecule which then desorbs (c).

Physisorption allows for *A* and/or *B* to be mobile on the surface, such that a reactive encounter can occur. The activation barriers and the reaction energies of ER and LH will probably differ, since the effect of the surface will be different. Other possible mechanisms include the hot atom (HA) mechanism, which may be considered to be in between LH and ER: *A* is physisorbed and *B* comes in from the gas phase; *B* will first physisorb on the surface, but before thermally equilibrating, reaction with *A* happens. Higher activation barriers can be overcome using this mechanism; however the activation barrier obtained via HA will be the same as the LH activation barrier. Moreover, the reaction frequency is lower in the ISM, hence the average lifetime of a species is very long. Therefore atoms, radicals and molecules are more likely to be in or close to the ground state when on a dust grain surface. From a kinetic point of view, the hot atom mechanism is interesting; however, kinetics are included in the astronomical model which will be used to study star-forming regions, using a statistical distribution for the possible reactions. Therefore the parameters obtained from studying LH can be used for both LH and the hot atom model.

In this study, a comparison of all reactions with the same reactions in the gas phase is made, for three different reasons. Firstly experimental research is widely available for gas phase reactions. Thus comparison (and hence benchmarking) with experimental results can be made through gas phase reactions. Similarly, most reported computational results are gas phase results, therefore it is imperative, for comparison with previous work to be possible, that gas phase reactions are also calculated. Finally, catalysis is defined in general through a comparison between two reactions, identical in beginning and ending products but different in reaction speed. Therefore the surface reactions studied here need to be compared to the uncatalysed, gas phase reaction.

1.2.2. Adsorption

There are two different types of adsorption, distinguished by the adsorption energy. Physisorption is the form of adsorption to a surface governed purely by van der Waals attraction. This is possible for any atom or molecule and can stabilise the species, while still allowing the adsorbate to retain at least some mobility on the surface. Typical physisorption enthalpies are of the order of a few kJ mol^{-1}, and can go up to 60 kJ mol^{-1} when dipole moments are present. Once above this value, adsorption will tend towards the formation of chemical bonds, which can be seen, for example, in a clear shift of vibrational frequencies of the adsorbate. Chemisorption, for which typical adsorption enthalpies are a few hundreds of kJ mol^{-1}, can be irreversible and the release of the adsorbate requires a certain activation barrier to be overcome, since a chemical bond must be broken. In dark molecular clouds, chemisorbed species cannot re-enter the gas phase without the help of an additional energy source (such as UV photons or cosmic rays). In addition, reactions involving chemisorbed species often require a large activation barrier to be overcome and, as such, chemisorption can slow down, or even entirely prevent, a given reaction from occurring on a surface. In this low-temperature regime, physisorption is the more important form of adsorption.

1.2.3. Formation of molecules

To date, a large amount of research of astronomical importance has been performed including investigations of the formation, adsorption and desorption of several different molecules, experimentally or theoretically, where ISM conditions were reproduced as closely as possible. All of the molecules appearing in Table 1.1 have been identified in the ISM but, as mentioned above, the abundances of some of these molecules cannot be explained using exclusively gas phase reaction mechanisms, indicating that surface reactions are likely to be of major importance, for example for CH_3OH and CO_2 formation. The formation of many small molecules has been investigated, both experimentally and theoretically, including CO_2, H_2O, H_2CO, CH_3OH, and C_2H_5OH. The formation of H_2 (and HD) has been studied particularly intensively.

Experimental chemists can derive desorption energies from temperature programmed desorption (TPD) studies, combined with a mass spectrometer. Infrared spectroscopy shows information on the identity of molecules, and, when applied to surface science, reflection absorption infrared spectroscopy (RAIRS, sometimes IRAS) can give information on the preferential site of adsorption on a surface (atop, bridged, or hollow), and the symmetry of adsorption. Many more surface science techniques exist in order to analyse and characterise the adsorbates. Despite the large number of experiments performed to investigate the formation of these molecules, the origin of many molecules in the ISM is still controversial, as is shown by, for example, the formation of methanol (24-30). The difficulties arise most likely from the fact that every experiment or simulation has its own conditions, i.e. the temperature, pressure, flux, etc. play a very important role in the exact mechanism of formation.

Previous investigations include studies of water (21, 31-38), ammonia (24, 32, 39, 40), carbon dioxide (41-44), formaldehyde (18, 25, 45, 46), methanol (18, 23-30, 32, 45, 47-50), and ethanol (51-53) formation and desorption. Different surfaces were used to study adsorption of astrochemical relevance including graphite (HOPG) (21, 32, 47, 54, 55), water ice (41, 56, 57), and silica (23, 33, 58); all being are logical choices given that evidence shows that carbon or silica are the most likely candidates to form the dust grain core, as shown in Figure 1.4. Several studies however, have already shown that defective surfaces are more reactive than non-defective surfaces and can lead to dissociative adsorption, as seen for water (21, 34) on defective graphite and on amorphous silica surfaces, for CO_2 (43) on the (1 0 1 0) surface of graphite ('zigzag'), and for methanol (23) on silica surfaces. These results will be discussed more in depth in Chapters 3, 4 and 5 where relevant.

1.2.4. Hydrogen gas

The hydrogen atom is the most abundant species present in the universe. About 90 % of the atoms in the universe are hydrogen, with the bulk of the remainder being helium (9%), oxygen, carbon and nitrogen (1, 3). Radiative recombination of two H atoms to form H_2 is not allowed as it makes use of a forbidden transition. Nonetheless, the most abundant molecule present in the universe is H_2, and astronomers and chemists have tried to explain this high abundance, including recombination of H and H^+, and H and H^- (59, 60). Although this explanation is valid for the early universe where ionic species are ubiquitous, ionic hydrogen atoms were rare in the later universe and this kind of recombination cannot explain the present abundance of hydrogen gas. The solution to this problem is the influence surfaces can have on reactions. In this case, the most important influence played by the surface is acting as a third body, such that recombination is no longer a forbidden process, and the formation energy is at least partially absorbed by the surface. The hydrogen gas formation reaction has been, and still is, intensively studied, and a large amount of data is available on the subject of hydrogen gas formation on different surfaces, including metallic (61-64) and graphitic surfaces (65-78), silicates (12, 79-81) and water ice (57, 82-85). The hydrogen problem is the first to be solved by including dust grains in the reaction mechanisms, and it is now widely accepted that other molecules may also be formed with the assistance of dust grains.

It was shown earlier, for example in Figure 1.4, that dust grains may be carbonaceous in origin. HOPG, highly orientated pyrolitic graphite, has been used as an astronomically relevant dust grain model. It is easily obtained experimentally and it can be modelled computationally using either a cluster approach (e.g. reference (86)) or a periodic approach . Theoretical results have shown that a hydrogen atom can both physisorb and chemisorb on an HOPG surface. The physisorption energy of hydrogen atoms on a graphite surface is very small, lower than 5 kJ mol^{-1} (87) whereas the chemisorption energy is around 65 kJ mol^{-1}. Chemisorption has an activation barrier around 20 kJ

mol^{-1}, and upon chemisorption, the carbon atom included in the chemical bond will pucker out of the surface by approximately 0.36 Å and tend more towards an sp^3 type carbon atom, thus breaking the aromaticity of graphite, which explains the rather low chemisorption energy. These results have been confirmed by many different studies (77, 87-92). Zecho *et al.* (91, 92) used an HOPG surface to show that incoming hydrogen atoms with an impact energy of 16 kJ mol^{-1} at relatively high temperatures (150 K and higher) can overcome the activation barrier and react with chemisorbed hydrogen to form H_2. It was shown by Sha et al. (77) that incoming atoms with an energy lower than 14.5 kJ mol^{-1} would scatter back without reacting. Furthermore, upon reaction, the surface lattice can reconstruct within 50 femtoseconds. Some part of the formation energy is absorbed by the surface, as shown by Baouche et al. (88). Chemisorbed hydrogen, however, is less relevant to the present study since, as previously mentioned, only small amounts of energy are available and therefore reactions with an appreciable reaction barrier are very unlikely to happen.

Various different studies, both experimental and theoretical, have investigated the rotational and vibrational distribution of H_2 formation from physisorbed H (65, 67, 73, 76) [65,66,73,93,94], showing that the highest populated states are around v = 3 – 5. It was suggested by Sidis et al. (66, 75), that the physisorption energy of H atoms on an HOPG surface may be too low for the surface to retain the atoms long enough, hence it is unlikely for reactions to happen. However, imperfections on surfaces, including charge defects and cavities, can resolve this problem. Vidali et al. (15) showed that the efficiency for recombination on different surfaces can be high, but only within a small temperature window. This observation can be understood as hydrogen is no longer mobile below a certain threshold temperature, whereas above a certain temperature it will desorb from the surface before reaction. Herbst et al. (93) showed that hopping barriers for hydrogen atoms physisorbed on olivine, amorphous carbon or mixed surfaces are very low, hence at very low temperatures (around 10 – 20 K) the H_2 recombination efficiency is still high. It can be concluded that hydrogen gas formation is a well understood process, showing that the effects of a surface include those of physisorption, increasing the reaction probability, and absorbing a portion of the formation energy.

The importance of the third body effect of the surface on a reaction has been shown for H_2 formation. For other formation reactions, it is possible that there is an activation barrier which can be influenced by the surface. Moreover, since the abundance of species other than H is at least 3 orders of magnitude lower in the ISM, adsorption on the surface will play an important role.

In the present research, the formation of three different molecules was studied: water (Chapter 3) and methanol (Chapter 4) are important biomolecular precursors and the most abundant molecules present in ISM ices, whereas OCS (Chapter 5) is thought to be very important for sulfur chemistry in the ISM. The effects which have been discussed in this chapter – adsorption, catalysis, and the third body effect – will be shown indeed to have an important influence on the formation of OCS, water and methanol.

1.3. References

1. *MS Encarta Online Encyclopedia*.
2. *Encyclopaedia Brittanica Online*.
3. Kaufmann, W. J. and Comins, N. F., *Discovering The Universe*, 1997.
4. May, B., Moore, P. and Lintott, C., *Bang! The Complete History Of The Universe*, 2006.
5. Williams, D. A., *Surf. Sci.*, 2002, **500**, 823.
6. Greenberg, J. M., *Surf. Sci.*, 2002, **500**, 793.
7. Williams, D. A., *Faraday Discuss*, 1998, 1.
8. Glover, S. C. O., *Astrophys. J.*, 2003, **584**, 331.
9. Williams, D. A. and Taylor, S. D., *Q J Roy Astron Soc*, 1996, **37**, 565.
10. Hu, A. M. and Duley, W. W., *Astrophys. J.*, 2007, **660**, L137.
11. *NASA StarDust mission*.
12. Pirronello, V., *Astrophys. J.*, 1997, **475**, L69.
13. Williams, D. A., Brown, W. A., Price, S. D., et al., *Astron Geophys*, 2007, **48**, 25.
14. Garrod, R., Park, I. H., Caselli, P., et al., *Faraday Discuss*, 2006, **133**, 51.
15. Vidali, G., Roser, J. E., Ling, L., et al., *Faraday Discuss*, 2006, **133**, 125.
16. Fraser, H. J., Bisschop, S. E., Pontoppidan, K. M., et al., *Mon. Not. R. Astron. Soc.*, 2005, **356**, 1283.
17. Vidali, G., Roser, J. E., Manico, G., et al., in *Space Life Sciences: Steps toward Origin(s) of Life*, Editon edn., 2004, vol. 33, pp. 6.
18. Watanabe, N., Nagaoka, A., Shiraki, T., et al., *Astrophys. J.*, 2004, **616**, 638.
19. Woodall, J., Agundez, M., Markwick-Kemper, A. J., et al., *Astron Astrophys*, 2007, **466**, 1197.
20. Manion, J. A., Huie, R. E., Levin, R. D., et al., *NIST Chemical Kinetics Database, NIST Standard Reference Database 17 (Web Version), Release 1.4.2, Data version 08.09*.
21. Cabrera-Sanfelix, P. and Darling, G. R., *J Phys Chem C*, 2007, **111**, 18258.
22. Goumans, T. P. M., Catlow, C. R. A. and Brown, W. A., *J Phys Chem C*, 2008, **112**, 15419.
23. Goumans, T. P. M., Wander, A., Catlow, C. R. A., et al., *Mon. Not. R. Astron. Soc.*, 2007, **382**, 1829.
24. Hiraoka, K., *AIP Conf. Proc.*, 2006, **855**, 86.
25. Hiraoka, K., Sato, T., Sato, S., et al., *Astrophys. J.*, 2002, **577**, 265.
26. Hiraoka, K., Wada, A., Kitagawa, H., et al., *Astrophys. J.*, 2005, **620**, 542.
27. Nagaoka, A., Watanabe, N. and Kouchi, A., in *Astrochemistry: from Laboratory Studies to Astronomical Observations*, eds. Kaiser, R. I., Bernath, P., Osamura, Y., et al., Amer Inst Physics, Melville, Editon edn., 2006, vol. 855, pp. 69.
28. Hidaka, H., *AIP Conf. Proc.*, 2006, **855**, 107.
29. Hidaka, H. and Hidaka, *Chem. Phys. Lett.*, 2008, **456**, 36.
30. Hidaka, H., Watanabe, N., Shiraki, T., et al., *Astrophys. J.*, 2004, **614**, 1124.
31. Birkett, G. R. and Do, D. D., *Mol. Phys.*, 2006, **104**, 623
32. Brown, W. A. and Bolina, A. S., *Mon. Not. R. Astron. Soc.*, 2007, **374**, 1006.
33. Collins, K. E., de Camargo, V. R., Dimiras, A. B., et al., *J Colloid Interf Sci*, 2005, **291**, 353.
34. Mahadevan, T. S. and Garofalini, S. H., *J Phys Chem C*, 2008, **112**, 1507.
35. Miyauchi, N., Hidaka, H., Chigai, T., et al., *Chem. Phys. Lett.*, 2008, **456**, 27.
36. Picaud, S., Collignon, B., Hoang, P. N. M., et al., *J Phys Chem B*, 2006, **110**, 8398.
37. Sanfelix, P. C., Holloway, S., Kolasinski, K. W., et al., *Surf. Sci.*, 2003, **532**, 166.
38. Suter, M. T., Andersson, P. U. and Pettersson, J. B. C., *Chem. Phys. Lett.*, 2007, **445**, 208.
39. Birkett, G. R. and Do, D. D., *Mol Simulat*, 2006, **32**, 523.
40. Lakhlifi, A. and Killingbeck, J. P., *J Phys Chem B*, 2005, **109**, 11322.
41. Talbi, D., Chandler, G. S. and Rohl, A. L., *J. Chem. Phys.*, 2006, **320**, 214.

42. Goumans, T. P. M., Uppal, M. A. and Brown, W. A., *Mon. Not. R. Astron. Soc.*, 2008, **384**, 1158.
43. Lilenfeld, H. V. and Richardson, R. J., *J. Chem. Phys.*, 1977, **67**, 3991.
44. Radovic, L. R., *Carbon*, 2005, **43**, 907.
45. Awad, Z., Chigai, T., Kimura, Y., et al., *Astrophys. J.*, 2005, **626**, 262.
46. Petraco, N. D. K., Allen, W. D. and Schaefer, H. F., *J. Chem. Phys.*, 2002, **116**, 10229.
47. Brown, W. A., Viti, S., Wolff, A. J., et al., *Faraday Discuss*, 2006, **133**, 113.
48. Geppert, W. D., Hamberg, M., Thomas, R. D., et al., *Faraday Discuss*, 2006, **133**, 177.
49. Houtman, C. and Barteau, M. A., *Surf. Sci.*, 1991, **248**, 57.
50. Das, A., Acharyya, K., Chakrabarti, S., et al., *Astron Astrophys*, 2008, **486**, 209.
51. Birkett, G. R. and Do, D. D., *Mol Simulat*, 2006, **32**, 887.
52. Burke, D. J., Wolff, A. J., Edridge, J. L., et al., *J. Chem. Phys.*, 2008, **128**.
53. Burke, D. J., Wolff, A. J., Edridge, J. L., et al., *Phys Chem Chem Phys*, 2008, **10**, 4956.
54. El-Barbary, A. A., Telling, R. H., Ewels, C. P., et al., *Phys Rev B*, 2003, **68**.
55. Li, L., Reich, S. and Robertson, J., *Phys Rev B*, 2005, **72**.
56. Papoular, R., *Mon Nor R Astron Soc*, 2005, **362**, 489.
57. Roser, J. E., Manico, G., Pirronello, V., et al., *Astrophys. J.*, 2002, **581**, 276.
58. Li, A. G., Greenberg, J. M. and Zhao, G., *Mon. Not. R. Astron. Soc.*, 2002, **334**, 840.
59. Hirata, C., *Mon. Not. R. Astron. Soc.*, 2006, **372**, 1175.
60. Lepp, S., Stancil, P. C. and Dalgarno, A., *J Phys B*, 2002, **35**, R57.
61. Gabriel, O., Schram, D. C. and Engeln, R., *Phys Rev E Stat Nonlin Soft Matter Phys*, 2008, **78**, 016407.
62. Greeley, J. and Mavrikakis, M., *J Phys Chem B*, 2005, **109**, 3460.
63. Sousa, C., Bertin, V. and Illas, F., *J Phys Chem B*, 2001, **105**, 1817.
64. Szabo, S. and Bakos, I., *Corros Rev*, 2004, **22**, 183.
65. Islam, F., Latimer, E. R. and Price, S. D., *J. Chem. Phys.*, 2007, **127**.
66. Jeloaica, L. and Sidis, V., *Chem. Phys. Lett.*, 1999, **300**, 157.
67. Latimer, E. R., Islam, F. and Price, S. D., *Chem. Phys. Lett.*, 2008, **455**, 174.
68. Martinazzo, R. and Tantardini, G. F., *J. Chem. Phys.*, 2006, **124**.
69. Martinazzo, R. and Tantardini, G. F., *J. Chem. Phys.*, 2006, **124**.
70. Mattera, L., Rosatelli, F., Salvo, C., et al., *Surface Sci*, 1980, **93**, 515.
71. Meijer, A., Farebrother, A. J. and Clary, D. C., *J Phys Chem A*, 2002, **106**, 8996.
72. Meijer, A., Farebrother, A. J., Clary, D. C., et al., *J Phys Chem A*, 2001, **105**, 2173.
73. Meijer, A. J. H. M., Fisher, A. J. and Clary, D. C., *J Phys Chem A*, 2003, **107**, 10862.
74. Morisset, S., Aguillon, F., Sizun, M., et al., *Phys Chem Chem Phys*, 2003, **5**, 506.
75. Morisset, S., Aguillon, F., Sizun, M., et al., *J. Chem. Phys.*, 2005, **122**.
76. Rutigliano, M., Cacciatore, M. and Billing, G. D., *Chem. Phys. Lett.*, 2001, **340**, 13.
77. Sha, X. W., Jackson, B. and Lemoine, D., *J. Chem. Phys.*, 2002, **116**, 7158.
78. Sha, X. W., Jackson, B., Lemoine, D., et al., *J. Chem. Phys.*, 2005, **122**.
79. Pirronello, V., Biham, O., Liu, C., et al., *Astrophys J Lett*, 1997, **483**, L131.
80. Ricchiardi, G., Vitillo, J. G., Cocina, D., et al., *Phys Chem Chem Phys*, 2007, **9**, 2753.
81. Vidali, G., Pirronello, V., Li, L., et al., *J Phys Chem A*, 2007, **111**, 12611.
82. Hornekaer, L., Baurichter, A., Petrunin, V. V., et al., *Science*, 2003, **302**, 1943.
83. Lemaire, J. L., Fillion, J. H., Dulieu, F., et al., *Actual Chimique*, 2008, III.
84. Pirronello, V., Liu, C., Roser, J. E., et al., *Astron Astrophys*, 1999, **344**, 681.
85. Roser, J. E., Swords, S., Vidali, G., et al., *Astrophys J Lett*, 2003, **596**, L55.
86. Allouche, A. and Ferro, Y., *Carbon*, 2006, **44**, 3320.
87. Sha, X. W. and Jackson, B., *Surf. Sci.*, 2002, **496**, 318.
88. Baouche, S., Gamborg, G., Petrunin, V. V., et al., *J. Chem. Phys.*, 2006, **125**.
89. Ferro, Y., Marinelli, F. and Allouche, A., *J. Chem. Phys.*, 2002, **116**, 8124.
90. Ferro, Y., Marinelli, F. and Allouche, A., *Chem. Phys. Lett.*, 2003, **368**, 609.

91. Zecho, T., Guttler, A., Sha, X. W., et al., *J. Chem. Phys.*, 2002, **117**, 8486.
92. Zecho, T., Guttler, A., Sha, X. W., et al., *Chem. Phys. Lett.*, 2002, **366**, 188.
93. Chang, Q., Cuppen, H. M. and Herbst, E., *Astron Astrophys*, 2005, **434**, 599.

Computational Methods

Chapter 2

Computational chemistry is one of the main means to study reaction kinetics and thermodynamics, to understand why certain reaction pathways are preferred over other ones, and to study the more complex behaviour of molecules and ions in detail. It is a wide field which includes wave function mechanics, density functional theory and molecular modelling, and can be applied to solid-state, gas-phase or solution systems. One of the major breakthroughs for computational chemistry, and more specifically for density functional theory (DFT), was the publication of two papers by the group of Hohenberg, Kohn and Sham (1, 2) in 1964 and 1965. These publications produced a practical form of DFT and this improvement, together with an increase of computer power and an exponential reduction in the price of computers, has led to computer clusters and high-performance superclusters now able to tackle more difficult problems at a higher accuracy within a sensible time span.

The aim of this chapter is to introduce the necessary background with the focus on the methods that were used in this work. A short review of Wave Function Theory (WFT) and DFT is given and coupled cluster theory (CCSD(T)) will be explained as this method was used for the benchmarking. Several different DFT methods were used for surface calculations. After this review, the importance of basis sets and the problems with smaller and larger sets are discussed. The Pople 6-311G** basis set was employed for most calculations – with the exception of the benchmarking where aug-cc-pVTZ was used. An extended discussion of transition states will follow, including the NEB algorithm which is one of two algorithms used to obtain the transition states. The chapter will finish with a discussion on the quantum chemical programs used, including Crystal06, Gaussian03 and Molpro, and a short overview of the functionals employed. It is, however, not possible to review all methods in quantum chemistry and further details can be found elsewhere (3-6).

2.1. Quantum Chemistry: WFT and DFT

Computational chemistry uses basic physical equations in order to solve chemical problems, implemented as a computational algorithm. Different approximations exist, e.g. electronic structure methods where the orbitals of electrons are the central objects or molecular mechanics where a molecule is treated as a combination of specific atoms. The size of a system – starting from an atom and going up to tens of thousands of atoms – is the main determining factor for which approximation is used. The scaling of the necessary computer time to solve a problem is not necessarily linear with the desired accuracy or with the number of electrons, and for very large problems a faster method is desired.

2.1.1. WFT and DFT: Ground States

There are two main branches of electronic structure methods: WFT (*ab initio* methods[1]) and DFT. Both methods are means to obtain the optimal, ground state energy of a system – for example a molecule – but differ in the approach used. WFT uses the ground state wave function as the central variable and, according to one of the WFT theorems, any physically observable property can be calculated using the correct operator acting on the ground state wave function, meaning that this wave function contains all possible information[2]. Every physically observable property can hence be computed from the ground state wave function, including energy, dipole, quadrupole and higher moments, excited energy levels, electron density, vibrational, rotational, NMR and EPR spectra,

---

[1] The meaning of "a*b initio* methods" depends on the author using the concept. Some authors prefer to use the term only when no empirical data is used, thus strictly speaking most DFT methods do not belong to the group of *ab initio* methods. However in the literature, *ab initio* is sometimes freely used where "electronic structure methods" should be used. Here *ab initio* will refer to methods which use no empirical data. Molecular modelling and methods derived from this (like QM/MM methods) will be ignored here as these methods are not used.

[2] This is the Copenhagen interpretation of Schrödinger's quantum mechanics. Other interpretations exist (e.g. Bohmian WFT; the many-world interpretation) but this is more of a philosophical difference. Here we will follow the Copenhagen interpretation.

hyperfine tensors, and so on. WFT is in theory exact but can unfortunately not be used on practical cases like real molecules due to the many-body problem and the exponentially rising number of variables with the increase of the number of electrons. A wave function is dependent on *4N* variables (three spatial coordinates and one spin coordinate per electron) and the time to solve the Schrödinger equation in the fastest way (Hartree-Fock) generally scales to the fourth power of the number of variables[3].

The ground state wave function of a system is defined by that wave function which yields the lowest total energy. Hence the energy is the most fundamental property of a system in WFT, and the operator which describes this is called the Hamiltonian, represented $\hat{H}$. The ground-state wave function is calculated using this operator, as shown in equations (2.1) and (2.2).

$$\hat{H}\Psi = E\Psi \tag{2.1}$$

$$\hat{H} = -\sum_{i=1}^{n}\frac{\nabla_i^2}{2} - \sum_{A=1}^{N}\frac{\nabla_A^2}{2M_A} - \sum_{i=1}^{n}\sum_{A=1}^{N}\frac{1}{r_{iA}} + \sum_{i=1}^{n-1}\sum_{j=i+1}^{n}\frac{1}{r_{ij}} + \sum_{A=1}^{N-1}\sum_{B=A+1}^{N}\frac{1}{r_{AB}} \tag{2.2}$$

Equation (2.1) is the Schrödinger equation, which describes the relation between the Hamiltonian, the wave function and the energy of a system. Equation (2.2) shows that the Hamiltonian is the sum of all of the contributions to the total energy including the kinetic energy of all electrons and nuclei (terms 1 and 2), the Coulomb attraction between all electrons and all nuclei (term 3), and the Coulomb repulsion between all unique pairs of electrons (term 4) and all unique pairs of nuclei (term 5). In this equation, *r* is the distance between two particles, lower case letters *i*, *j*, *n* count the electrons, capital letters *A*, *B*, *N* count nuclei, M_A is the mass of nucleus *A*, and all quantities (including mass and distance) and constants are in atomic units (see e.g. (3) for details on atomic units).

Solving the Schrödinger equation is difficult. The equation is not linear but also contains quadratic terms (the Coulomb repulsion between the electrons is one of the non-linear terms).

---

[3] Strictly speaking this is an upper bound to the time needed. Algorithms exist to speed up these calculations, e.g. by disregarding near-zero integrals or by using symmetry. However, in general the time needed for a Hartree-Fock calculation scales to the power of 3.5 – 4.

Because of the large ratio of the mass of a nucleus to the mass of an electron (for H this ratio is larger than 1800), it is possible to approximate this problem by considering the nuclei and the electrons as being independent from one other (the Born-Oppenheimer approximation). This is equivalent to the assumption that the nuclei have greatly more inertia than the electrons. Therefore, any change in geometry will invoke an instantaneous reaction from the electrons. In this approach, one can write the total wave function as a product of an electronic and a nuclear wave function, which are independent of each other. The electronic wave function can be obtained by solving the electronic Schrödinger equation shown in (2.3), which differs from (2.2) in that terms 1 and 3 are now grouped together into a one-electron operator, and terms 2 and 5 are now constant and can thus be omitted until the electronic Schrödinger equation is solved.

$$\hat{H}_{el} = -\sum_{i=1}^{n}\left(\frac{\nabla_i^2}{2} - \sum_{A=1}^{N}\frac{1}{r_{iA}}\right) + \sum_{i=1}^{n-1}\sum_{j=i+1}^{n}\frac{1}{r_{ij}} \tag{2.3}$$

The Hartree-Fock (HF) approximation, from which most wave function methods are derived, then rewrites the electronic wave function as a combination of one-electron wave functions and replaces the electron-electron repulsion with an effective one-electron potential, which creates a series of eigenvalue equations shown in eqs. (2.4) - (2.6).

$$f(i)\chi(i) = \varepsilon_i \chi(i) \tag{2.4}$$

$$f(i) = -\frac{\nabla_i^2}{2} - \sum_{A=1}^{N}\frac{Z_A}{r_{iA}} + v(i) \tag{2.5}$$

$$v(i) = \sum_{j=1}^{n}\left[J_{ij} - K_{ij}\right] \tag{2.6}$$

The $\chi(i)$ are the one-electron orbitals with energy ε_i. $f(i)$ is the Fock operator, containing the contributions which act on one electron i. Finally, the effective one-electron potential $v(i)$ is written as the average influence of all electrons, explicitly writing Coulomb (J_{ij}) and exchange (K_{ij}) contributions separately. HF is, however, a mean-field approximation and does not include any electron correlation. The correlation can partially be recovered by post-HF techniques, for example configuration interaction (CI) or coupled cluster (CC). Post-HF techniques, like CI and CC, are based on the orbitals created by HF. In addition to the orbitals which are occupied in HF theory, post-HF theories use the virtual orbitals created by HF.

HF theory uses so-called Slater determinants, an elegant way of combining one-electron orbitals in an anti-symmetric way such that Pauli's exclusion principle is followed by definition. However, in using one Slater determinant, only that combination of orbitals which yields the lowest energy is allowed. CI will correct HF by considering the possibility of electrons occupying excited states, hence multiple Slater determinants will be included. In solving the Schrödinger equation, HF theory will generate a set of occupied electron orbitals, and a set of unoccupied virtual orbitals which are higher in energy than the previous ones. CI will use these virtual orbitals to create a new wave function, which expands the Hartree-Fock wave function (2.7):

$$\Phi = a_0\Psi + \sum_S a_S\Psi_S + \sum_D a_D\Psi_D + \sum_T a_T\Psi_T + \ldots \tag{2.7}$$

In equation (2.7), the indices *S*, *D*, *T* refer to singly, doubly and triply excited states. For a singly excited state, this means that in the original ground state wave function obtained with HF, one of the occupied orbitals is replaced with one of the unoccupied orbitals. The CI method is computationally very demanding (Table 2.1 shows the formal scaling of several methods with the number of used orbitals) and therefore CI is usually truncated after double excitations (CID and CISD)[4]. Truncated CI however suffers from a problem known as size inconsistency. This problem is easily illustrated with an example. Imagine the CISD energy for two infinitely separated H_2 molecules, compared to twice the CISD energy of one H_2 molecule. In the latter case, single and double excitations are allowed twice (i.e. for two molecules separately), which will yield a lower energy than the one calculated in the first case, where both molecules are calculated at the same time and therefore two excitations for both molecules is the maximum allowed.

---

[4] Because of the orthonormality of the basis functions, CI with only single excitations, CIS, will not give any improvement over HF. CID is the 'least' possible truncation which improves on HF energies. CISD, only slightly more expensive in time, is therefore generally used.

In CC, the linearity of CI in equation (2.7) is replaced by a power series, shown below.

$$\Phi = e^{T}\Psi = \Psi + T\Psi + \frac{1}{2}T^{2}\Psi + \frac{1}{6}T^{3}\Psi + \dots \tag{2.8}$$

$$T = T_1 + T_2 + T_3 + \dots + T_N \tag{2.9}$$

In eq. (2.8) T is named the cluster operator, and it represents the possible excitations. Eq. (2.9) shows T explicitly as the sum of single, double, etc. excitations, up to N (all electrons are excited). When, for example, T represents single and double excitations, it can be seen that the second term in the CCSD equation (2.8) (which would be the equivalent of CISD in CI, cfr. eq. (2.7)) would include double (single*single), triple (single*double) and quadruple (double*double) excitations, whereas further terms include even higher excitations.

Table 2.1: Formal scaling of the time required to converge the energy with respect to the system size, for different DFT and WFT methods. *DFT scaling depends on the functional used, but is generally about the same or better than HF. Currently, linear scaling methods for DFT are available for (very) large systems.

Methods	**Power of the orbitals with which the method scales**
DFT*	**3**
Hartree-Fock, DFT*	**4**
MP2	**5**
MP3, CISD, CCSD	**6**
MP4, CCSD(T), CISD(T)	**7**
MP5, CISDT, CCSDT	**8**
MP6	**9**
MP7, CISDTQ, CCSDTQ	**10**

The current standard truncation of CC is at CCSD, with addition of an estimate of the triple excitations (denoted CCSD(T)). Using an estimate for the triplets, rather than the exact triplets correction, yields (as shown in Table 2.1) a gain of one order of magnitude in computational speed. Moreover, the computational effort rises rapidly and where HF theory formally scales with N^4 (7) (N being the number of basis functions used), more accurate post HF methods scale with higher powers (see Table 2.1). CISD and CCSD scale with N^6, and therefore it is only possible to use these very expensive and time-consuming methods for small molecules.

As the name suggests, DFT uses a functional of the density to obtain the energy of a system. Because it is unknown how to get the Universal Functional, which would give the exact density and energy of a system (see further, eq. (2.10)), we are forced to use approximations. Over time, improvements have been made on the basic “electron gas” functional – treating the density as a uniform gas – and more sophisticated functionals have been created. Perdew (8) suggested a classification dependent on which terms are used within functionals and named it Jacob’s Ladder. Table 2.2 shows this ladder and some examples of functionals for each rung. At the bottom of this ladder stand methods which only use the electron density. With increasing level more variables are included: the gradient of the density, the second derivative (and higher order derivatives) of the gradient incorporating kinetic energy, exact exchange, and the full information of the Kohn-Sham orbitals. Modern DFT, which uses the Kohn-Sham *ansatz*, uses a 4N-dependent (auxiliary) wave function similar to WFT. However, where the Hartree-Fock approximation fails to include electron correlation and post-HF methods are necessary to correct for this, correlation is already included in DFT functionals.

The density functional itself is, as shown in eq. (2.10), usually written as a sum of the kinetic energy functional (*T*), the Coulomb functional for electron-nucleus attraction (E_{ne}), the Coulomb functional for electron interaction (*J*), and a functional for non-classical contributions along with several corrections (E_{XC} or *XC*).

$$E_{DFT}\left[\rho\right]=T\left[\rho\right]+E_{ne}\left[\rho\right]+J\left[\rho\right]+E_{XC}\left[\rho\right] \qquad (2.10)$$

Here $T\left[\rho\right]$ represents the kinetic energy of the electrons, $E_{ne}\left[\rho\right]$ is the electron-nucleus attraction, $J\left[\rho\right]$ is the Coulomb repulsion, and $E_{XC}\left[\rho\right]$ is defined by setting eq. (2.10) equal to the exact energy, e.g. eq. (2.1). In the Kohn-Sham *ansatz* (2), a system of non-interacting electrons replaces the real system. The requirement of the non-interacting system is that its electron density equals the electron density of the real system. The real kinetic energy can now, to a good approximation, be calculated as the kinetic energy from the set of auxiliary orbitals with non-interacting electrons. With the introduction of the Kohn-Sham auxiliary orbitals, the first three terms in eq. (2.10) can be described exactly (eqs. (2.11) – (2.13)):

Table 2.2: Jacob's Ladder for density functionals. The variables column shows that on every level of the ladder, more variables are included, improving the DFT method but becoming computationally slower.

Level	Name	Variables	Additional variables	examples
5	Generalised RPA	$\rho, \nabla\rho,$ $\nabla^2\rho, XX$ $virtual\ \chi$	Unoccupied orbitals	OEP2
4	Hyper-GGA or hybrid GGA	$\rho, \nabla\rho,$ $(\nabla^2\rho), XX$	Exact (HF) exchange	B3LYP, MPWB1K, PW1K
3	Meta-GGA	$\rho, \nabla\rho,$ $\nabla^2\rho$	Second- and higher order derivatives of the density	B95, PKZB
2	GGA *Generalised gradient approximation*	$\rho, \nabla\rho$	Density gradient	BLYP, PW91, PBE
1	LDA *Local density approximation*	ρ	Electron density	VWN, LSDA

$$T_S[\rho] = -\frac{1}{2}\sum_i \langle \vartheta_i | \nabla^2 | \vartheta_i \rangle \tag{2.11}$$

$$E_{ne}[\rho] = \int \rho(\vec{r}) \sum_A \frac{Z_A}{|\vec{R}_A - \vec{r}|} d\vec{r} \tag{2.12}$$

$$J[\rho] = \frac{1}{2}\int\int \frac{\rho(\vec{r}_1)\rho(\vec{r}_2)}{|\vec{r}_1 - \vec{r}_2|} d\vec{r}_1 d\vec{r}_2 \tag{2.13}$$

The subscript S in the kinetic energy term denotes that this kinetic energy is calculated from a Slater determinant. The XC functional is then defined as the functional which yields the energy such that eq. (2.10) is true, i.e. the total energy has the correct value. As mentioned above, the kinetic energy (2.11) is calculated as the kinetic energy from the set of auxiliary orbitals with non-interacting electrons. The error that arises from this approximation, together with the non-classical contributions from the electron-electron interaction, forms the XC functional as shown in eq (2.14).

$$E_{XC}[\rho]=\left(T[\rho]-T_S[\rho]\right)+\left(E_{ee}[\rho]-J[\rho]\right) \tag{2.14}$$

The XC functional is commonly split into an exchange functional and a correlation functional. Both of these forms are the topic of continuous development and improvement. In the past, exchange and correlation functionals have been developed simultaneously, and the large errors created by both functionals partially cancel each other out. Therefore, separation of the XC functional into an X and a C functional may not be appropriate and a combination of two, separately developed X and C functionals, should always be verified.

The simplest form DFT can take is the local density approximation (LDA), where the electron density is that of a uniform electron gas. This method has proved to be very useful for systems with almost no external potential, like crystalline metals (5). However, the electron gas approximation is based upon a slowly varying electron density (as is the case in for example metals) and when abruptly changing densities are involved, for example in molecules, LDA performs badly. The gradient of the density was introduced in generalised gradient methods (GGA) as a correction to LDA, and because of a better description of a corrugated electron density these methods perform better than LDA for chemical systems. Meta-GGA functionals also take into account the second derivative of the density (and/or of the Kohn-Sham orbitals) and higher-order derivatives.

The fourth rung of Jacob’s Ladder includes exact exchange or HF exchange, applying the same formulae as HF theory (equations (2.4) – (2.6)) to calculate the exchange energy. The contribution of the exchange energy to the total energy is larger than the contribution of the correlation energy, therefore it seems feasible to try and improve the former first. However, since errors in both exchange and correlation functionals partially cancel each other out, replacing the entire exchange energy by exact exchange normally increases the error in the total density functional. Usually a mixing of 20% exact exchange and 80% from the exchange functional is taken, but a high percentage can prove advantageous for certain applications.

Physisorption, dispersion forces (London forces) and van der Waals interactions, barrier heights and transition states are known problems within DFT (6, 9, 10). In all of these cases, the forces involved arise from long-distance electron correlation, which is only poorly represented by DFT as the functionals used are local or semi-local. Mixing in a rather large amount of exact exchange (11) has been shown to provide a better description of the dispersion energy curve and has led to the development of kinetically optimised functionals, which are able accurately to reproduce barrier heights. Similarly, since HF overestimates reaction barriers and DFT underestimates them, accurate barriers can be calculated by using hybrid DFT methods. Even though hybrid functionals occupy the fourth rung, the second derivative of the density is not always necessarily included. When this is the case, the functional is referred to as meta-hybrid GGA.

2.1.2. Basis Sets

Within DFT and WFT, part of the numerical error in a solution is determined by the choice of basis set. The basis set is used to approximate the true orbitals with mathematical functions. A variety of basis sets are available, each of which has its own strengths and weaknesses.

Plane wave and augmented plane wave basis sets – almost always with, but sometimes without, pseudopotentials – are periodic functions which are excellent for describing infinite structures such as metallic solids and crystals. The basis functions are not concentrated around a certain area of space, preventing any bias as to where electrons are located. For metals it is known that the valence electrons are loosely bound and plane wave functions allow this diffuseness, even with a small number of functions, making a plane wave basis set the ideal choice. The general form of plane wave functions is shown in eqs. (2.15) and (2.16) (6), with *A*, *B* and *k* being parameters of the function:

$$\phi(x) = Ae^{ikx} + Be^{-ikx} \tag{2.15}$$

$$\phi(x) = A'\cos(kx) + B'\sin(kx) \tag{2.16}$$

$$E = \frac{1}{2}k^2 \tag{2.17}$$

The energy of a plane wave function can easily be derived and is shown in eq. (2.17). The fact that the energy of a plane wave is straightforwardly calculated is used to truncate the basis set. A cut-off energy is set and plane waves having energy below this energy are allowed, those with energy higher than the cut-off are not included in the basis set. Convergence of the basis set is reached when the total energy of a system does not change significantly when the cut-off energy is increased.

Localised orbitals have a maximum usually concentrated on a nucleus, and decay to zero at infinite distance, in contrast with plane wave orbitals. Two commonly used localised orbitals are Slater type orbitals (STO) and Gaussian type orbitals (GTO). Their mathematical forms are shown below in eq. (2.19) and eq. (2.18)); here ζ is a parameter which determines the height of the exponential function, N is a normalisation constant, Y is a spherical harmonic function, and r, θ, φ, x, y, z are the spherical and Cartesian coordinates.

$$\chi^{STO}(r,\theta,\varphi) = NY(\theta,\varphi)r^{n-1}e^{-\zeta r} \tag{2.18}$$

$$\chi^{GTO}(x,y,z) = Nx^{l_x}y^{l_y}z^{l_z}e^{-\zeta r^2} \tag{2.19}$$

Localised orbitals have the advantage that they have a straightforward pictorial representation and they can be easily understood in terms of chemical bonds. The fact that they are localised means they can be used to describe molecules and ions. The difference between STO and GTO is in the exponent. The STO is based on the exact solution for the hydrogen atom and, as such, describes the exponential decay of the orbitals with distance correctly. GTO give a less accurate description of this decay and do not have the correct shape of the cusp at the nuclear position. Linear combinations of GTO can be made to approximate this behaviour. Integrals of GTO, however, are computationally much more efficient (as the mathematical product of two GTO's yields another

GTO) and herein lies the strength of GTO. Following this philosophy, basis sets built up from contracted Gaussian functions were developed, in particular by the group of John Pople (6, 12). These GTO are then used as an approximation of STO and, even though about three times as many GTO are needed to reach a given level of accuracy, the decrease in computational effort needed compensates for this. The names that these basis sets were given refer to the size of the set, relative to the minimal number of functions the basis set requires (one per electron): double zeta (DZ), triple zeta (TZ), quadruple zeta (QZ) and so on. Unfortunately, as already discussed, the time needed to calculate increases rapidly with increasing size of the basis set.

The addition of orbitals which have a higher quantum number than the valence orbitals allows for polarisation of the atom. For H, for example, this means that a set of p-orbitals is added. For example when a hydrogen atom approaches a Na^+ ion, partial occupation of these orbitals by electrons will polarise the hydrogen atom, leading to a better description of the system. Finally, diffuse functions can be added to allow for correction for the long-range interactions. Diffuse functions, usually s- or p-type functions (6), differ from other basis functions in that they have a very small value of ζ in eq. (2.19), thus increasing the distance over which they decay. A more complete discussion of basis sets can be found elsewhere (6).

In this work, the contracted TZ Pople 6-311G(d,p) basis set was used[5]. For consistency and comparison reasons, only one basis set was chosen. Diffuse functions were not included for two reasons. Firstly, the Crystal06 code which was used during this research (see section 2.2.2) cannot utilise diffuse functions in a periodic system, since too large an overlap leads to numerical instability and causes a computationally linearly dependent basis set. Secondly, coronene was used as a dust grain model and for smaller basis sets it was found previously that coronene and similar polycyclic aromatic hydrocarbons are computationally unstable (13, 14). In particular, it was found that, depending on the basis set and Hamiltonian used, coronene can have an imaginary frequency (15). This imaginary frequency is associated with the antisymmetrical out-of-plane vibrations of the six

---

[5] For example see https://bse.pnl.gov/bse/portal

centre carbon atoms (b2g symmetry). It is most likely that this is an artefact and hence diffuse Gaussian functions in a small Pople basis set should be avoided. For graphene, the exclusion of diffuse functions only has a minor and negligible impact on the final result. The adsorption energies and the optimised distance between the adsorbate and the surface will however change, and again it is very likely that the calculated adsorption energy will be larger (i.e. stronger adsorption) when diffuse functions are included. Calculations on the helium dimer and the water dimer[6], both performed exclusively to estimate the influence of diffuse functions, showed that the energy increased (i.e. a diffuse basis set has a smaller physisorption energy than a basis set which lacks diffuse functions), but only for a value of 1.5 to 6.0 kJ mol^{-1}. Furthermore plane wave basis sets could not be used, as the available computational programs do not support plane waves and hybrid DFT simultaneously.

2.1.3. Transition States

Transition states and transition state theory form the basis for an understanding of kinetics, including chemical reactions and chemical reaction rates. The catalytic influence of surfaces on the rate of reactions is the central topic of this research; therefore transition states, algorithms for calculating them and their subsequent use in transition state theory will be discussed below.

2.1.3.a. Transition State Theory and Reaction Rates

Transition States and Potential Energy Surfaces

A transition state is defined as the geometry which has the maximum energy, on a minimum energy path (MEP) connecting a starting geometry and an ending geometry. This means that the

---

[6] Calculations were performed with Gaussian03, using the MPWB1K functional. The basis sets used were the Pople 6-311G** and 6-311++G** basis sets. The calculations were performed both with and without zero-point energy corrections; similar results were obtained.

transition state energy is, classically, the minimal energy required to reach a product state starting from reactants. This is equivalent to all but one coordinate being minimum, where the transition coordinate is at a maximum energy. For any system with N atoms, 3N-6 degrees of freedom are available (3N-5 if the system is linear) for vibrations and thus 3N-6(5) coordinates are needed to describe the system. Thus, in going from a certain geometry towards a different geometry, 3N-6(5) coordinates will span a 3N-5(4) dimensional potential energy surface. It is in this multidimensional space that one needs to search for a transition state, and as such obtain the activation energy for a particular reaction. Computational algorithms searching for the transition state are described in section 2.2.

Transition state theory, as followed here, was described by Eyring (16) in 1935. The location of a transition state is fully defined by the potential energy surface (PES), as the first and second derivatives of the energy with respect to any coordinate determine whether or not a particular configuration is a stationary point. The latter has the first derivative of the energy (*E*) with respect to any single variable (x_i) equal to zero. The distinction between a minimum and a transition state lies in the second derivatives. When one of the second derivative matrix (the Hessian matrix) eigenvalues is negative, this corresponds to a transition state or a first order saddle point, while higher order saddle points have a corresponding number of negative eigenvalues. A minimum is defined by eq. (2.20) whereas a transition state is defined by eq. (2.21).

$$\begin{aligned}&\frac{\partial E}{\partial x_i}=0 \quad \text{for all } i\\&\frac{\partial^2 E}{\partial x_i^2}>0 \quad \text{for all } i\end{aligned} \tag{2.20}$$

$$\begin{aligned}&\frac{\partial E}{\partial x_i}=0 \quad \text{for all } i\\&\frac{\partial^2 E}{\partial x_j^2}<0 \quad \text{for one } j\\&\frac{\partial^2 E}{\partial x_i^2}>0 \quad \text{for all } i\neq j\end{aligned} \tag{2.21}$$

The harmonic frequency of a molecular vibration is linked to the force constant matrix as explained in eqs. (2.22) – (2.24). The force acting on a harmonic spring depends on the mass *m* and the force constant *k*, and can be written as eq. (2.22):

$$\begin{aligned} \vec{F} &= m\frac{\partial^2 \vec{x}}{\partial t^2} \\ \vec{F} &= -k\vec{x} \end{aligned} \tag{2.22}$$

This differential equation has a periodic solution $x(\omega)$, with ω representing the frequency (2.23):

$$\omega = \sqrt{\frac{k}{m}} \tag{2.23}$$

The frequencies are related to the Hessian matrix *H*, and it is possible to calculate them from the eigenvalues f_{mwc}^{i} via equation(2.24), where *c* is the speed of light, v_i are the frequencies, $\tilde{v}_i$ are the wave numbers and f_{mwc}^{i} are the mass-weighted eigenvalues of the Hessian matrix.

$$\begin{aligned} v_i &= \frac{\sqrt{f_{mwc}^{i}}}{2\pi} \\ \tilde{v}_i &= \frac{\sqrt{f_{mwc}^{i}}}{2\pi c} \end{aligned} \tag{2.24}$$

At a minimum, all of the force constants are strictly positive. In a transition state however, one of the force constants is negative, yielding an imaginary frequency. Figure 2.1 shows the change in energy of two systems with respect to the change in a reaction coordinate. The left hand system is stable in this particular coordinate when the energy level is the lowest energy level. The frequency then depends on the curvature of the PES or its quadratic approximation (shown in red). On the right hand side, the reaction coordinate shown encounters a maximum. The imaginary frequency is related to the curvature of the PES.

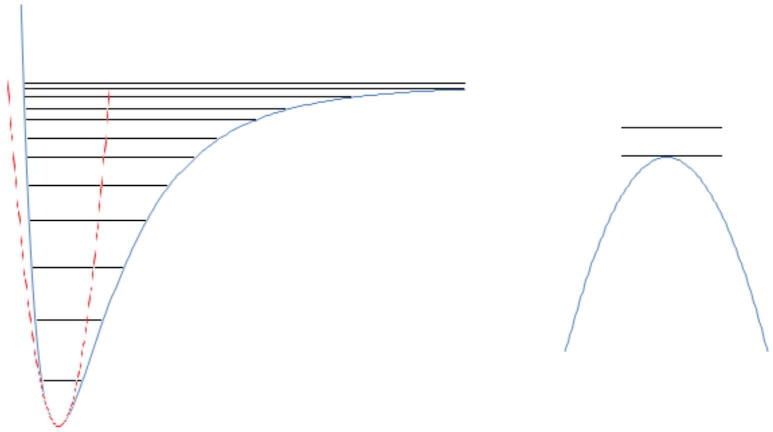

Figure 2.1: 1D potential energy surfaces, e.g. when stretching a chemical bond. The left hand figure shows a Lennard-Jones type function; the red curve is the approximate parabola describing a harmonic approach. The frequency of this bond is related to the broadness of this parabola. On the right hand side is the potential energy surface of a transition state reaction coordinate. The absolute value of the imaginary frequency is also related to the broadness of the approximating parabola.

Reaction Rates

A reaction rate equation for a reaction *A* + *B* ⟶ *C* is written as equation (2.25).

$$\frac{d[C]}{dt} = k(T)[A][B] \tag{2.25}$$

The Arrhenius rate constant *k* depends on the temperature *T* and can either be experimentally determined or it can be calculated as in eq. (2.26).

$$k = A\exp\left(-\frac{\Delta E^{\neq}}{RT}\right) \tag{2.26}$$

In this equation, R is the universal gas constant and $\Delta E^{\neq}$ is the difference in energy between the transition state and the reactant state i.e. the activation energy; it is the minimum energy which is needed for the reaction to proceed. Tunnelling is neglected here: generally the activation energy needed for reactions including tunnelling is lower than when tunnelling is not taken into account. However, tunnelling can be neglected for reactions that involve the movement of elements heavier than H and to a lesser extent D. A is the pre-exponential factor, accounting for reaction probability.

The pre-exponential factor can be calculated using transition state theory (17), as shown in equation (2.27), using the Boltzmann constant k_B and Planck's constant h:

$$k^{\neq}(T) = \frac{k_B T}{h} \frac{Q^{\neq}(T)}{Q^{R}(T)} \exp\left(-\frac{\Delta E^{\neq}}{kT}\right) \tag{2.27}$$

Combined with eq. (2.26), A can be calculated as follows:

$$A = \frac{k_B T}{h} \frac{Q^{\neq}(T)}{Q^{R}(T)} \tag{2.28}$$

In this equation, Q is the partition function (the $^{\neq}$ refers to the transition state, the ^{R} to the reactant state). In the following discussion, it has been assumed that the reaction is a Langmuir Hinshelwood type reaction. Equation (2.28) can then be further decomposed into eq. (2.29).

$$A = \frac{\dfrac{k_B T}{h}}{\dfrac{2\pi m k_B T}{h^2 N_A}} \frac{\exp\left(\sum_i \ln\left(1-\exp\dfrac{-v_i}{T}\right)^{-1}\right)^{\neq}}{\exp\left(\sum_i \ln\left(1-\exp\dfrac{-v_i}{T}\right)^{-1}\right)^{R}} \tag{2.29}$$

The v_i are as defined in eq. (2.24), m and T are the mass of the reactant and the temperature respectively. The exponentials in the numerator and denominator are the vibrational partition functions for the transition state and the reactant state respectively. The factor of $\frac{k_B T}{h}$ is the frequency factor accounting for the imaginary frequency of the transition state; $\frac{2\pi m k_B T}{h^2 N_A}$ is the relative[7] translational partition function per unit area. Rotational partition functions will make only a small contribution, since the masses of the surfaces considered are very large, and hence the change of moment of inertia will be negligible. The equations derived thus far, especially eq. (2.29), assume

---

[7] The translational partition function has a value of $\sqrt{\frac{2\pi m k_B T}{h^2 N_A}}$ per degree of translational freedom. Since it was assumed that an LH reaction takes place, because of physisorption, every species has two degrees of freedom leading to a power of $\frac{2}{2*2}$, thus $\frac{2\pi m k T}{h^2 N_A}$ appears in the denominator.

that we are dealing with a Langmuir Hinshelwood type of mechanism. In the case of an Eley Rideal reaction this equation will become

$$A = \frac{\frac{k_B T}{h}}{\left(\frac{2\pi m k_B T}{h^2 N_A}\right)^{\frac{3}{2}}} \frac{\exp\left(\sum_i \ln\left(1-\exp\frac{-v_i}{T}\right)^{-1}\right)^{\neq}}{\exp\left(\sum_i \ln\left(1-\exp\frac{-v_i}{T}\right)^{-1}\right)^{R}} \tag{2.30}$$

Thus, one vibrational degree of freedom in an LH reaction becomes a translational degree of freedom in ER. Moreover, since in ER there are gas phase species, this radical or molecule has rotational degrees of freedom (i.e. if it is not a single atom) which are no longer negligible. These rotational frequencies can be treated similar to the vibrational frequencies. Thus, via equations (2.26), (2.29) and (2.30), and the calculated activation energy, it is possible to predict reaction rates for reactions catalysed by surfaces from the energy and harmonic frequencies of reactants and transition states.

2.1.3.b. Algorithms to find Transition States

Conceptually, there are two different sets of algorithms to find a transition state, depending on whether one starts from a geometry close to a suspected transition state or from two different optimised geometries, between which one wants to find a transition state. The first group of methods are called chain algorithms, whereas the second group are called hill-walking algorithms.

Algorithms: Chain algorithms

Chain algorithms use two geometries, which are usually considered ‘frozen’ (i.e. the configuration or geometry is considered optimised; some algorithms allow optimisation of the end points as well), and will generate a number of images in between these beginning and ending points.

Depending on when and how these points are generated and optimised, a number of different algorithms have been proposed including nudged elastic band (NEB) and climbing image nudged elastic band (CI-NEB), conjugate peak refinement (CPR), the ridge method, and the string method. The NEB and CI-NEB methods have been implemented in the Crystal06 package (18) whereas the algorithm used within the Gaussian03 package is the Synchronous Transit-Guided Quasi-Newton (STQN) method, and a discussion of these will follow here. For a description of other algorithms, including the CPR, the ridge and the string method, the reader is referred to other available sources (19).

Nudged Elastic Band

In NEB a number of images are created in between the first and the last points, which are usually connected through a straight line. This means that the coordinates of any atom in a particular image are calculated straightforwardly from the initial geometry, the final geometry, and the total number of images – equation (2.31).

$$x_i^{\alpha} = \frac{N+1-\alpha}{N+1} x_i^{I} + \frac{\alpha}{N+1} x_i^{F} \qquad (2.31)$$

In this equation, α is the number of the image, *N* is the number of generated images, *x* is one coordinate, *i* is the coordinate counter (*i* =1, 2, 3 for x, y, z), and *I* and *F* stand for the initial and final structures respectively. From this formula, it can be seen that image 0 is the initial and image *N*+1 is the final geometry. When the images are created, the energy of every image, and accordingly the forces on the atoms, are calculated. The algorithm will now try to find a minimum energy path (MEP) from reactants to products. In order to ensure an equal spacing between the images and to ensure that the images still form a path from the reactants to the products, a virtual spring is attached in between every two consecutive images. The real forces for every image are then written as the sum of two vectors. One of these vectors is perpendicular to the springs attached to this image, the other lies in the plane formed by these springs. During the optimisation of the MEP only the perpendicular forces and the spring forces are used, while the parallel forces are neglected. In neglecting the parallel forces the images will be forced to form a continuous path uphill, whereas the spring forces keep an approximately equal spacing between the images. The total force acting on each image is described by equation (2.32).

$$\vec{F}_i = \left(\vec{F}_i^{spr}\right)_{\parallel} - \left(\nabla E\left(\vec{R}_i\right)\right)_{\perp} \tag{2.32}$$

In this equation, $\vec{F}_i^{spr}$ is the spring force acting on image *i*, as shown in equation (2.33) and $\nabla E\left(\vec{R}_i\right)$ is the gradient of the energy.

$$\vec{F}_i^{spr} = k\left\{\left|\vec{R}_{i+1} - \vec{R}_i\right| - \left|\vec{R}_i - \vec{R}_{i-1}\right|\right\}\vec{\tau}_i \tag{2.33}$$

When image *I* is not an extremum, $\vec{\tau}_i$ is defined as

$$\vec{\tau}_i = \begin{cases} \vec{R}_{i+1} - \vec{R}_i & E_{i-1} < E_i < E_{i+1} \\ \vec{R}_i - \vec{R}_{i-1} & E_{i-1} > E_i > E_{i+1} \end{cases} \tag{2.34}$$

At an extremum, $\vec{\tau}_i$ is defined as

$$\begin{aligned} \vec{\tau}_i &= \begin{cases} \left(\vec{R}_{i+1} - \vec{R}_i\right)\Delta E_i^{\max} + \left(\vec{R}_i - \vec{R}_{i-1}\right)\Delta E_i^{\min} & E_{i-1} < E_{i+1} \\ \left(\vec{R}_i - \vec{R}_{i-1}\right)\Delta E_i^{\max} + \left(\vec{R}_{i+1} - \vec{R}_i\right)\Delta E_i^{\min} & E_{i-1} > E_{i+1} \end{cases} \\ \Delta E_i^{\max} &= \max\left(\left|E_{i+1} - E_i\right|, \left|E_i - E_{i-1}\right|\right) \\ \Delta E_i^{\min} &= \min\left(\left|E_{i+1} - E_i\right|, \left|E_i - E_{i-1}\right|\right) \end{aligned} \tag{2.35}$$

Using this algorithm will ensure that the chain moves in the right direction, describing the minimum energy path (MEP). Figure 2.2 shows a pictorial representation of a sample NEB calculation where the energy of every image is plotted following the chemical reaction path. Upon convergence, the image with the highest energy is the closest to the transition state and it is this energy which will be used. It can be seen from Figure 2.2 that the maximum in the MEP does not necessarily coincide with the maximum energy image. A solution for this problem is to allow at least one image to move along the energy path.

There are two main versions of NEB, which differ in the way the spring constants are treated. In the variable spring constant approach, the spring constant for every spring depends on the relative energy of the images that it connects and on the energy of the highest image. Rather than having one spring constant, two constants k_1 and k_2 are used as shown in equation (2.36).

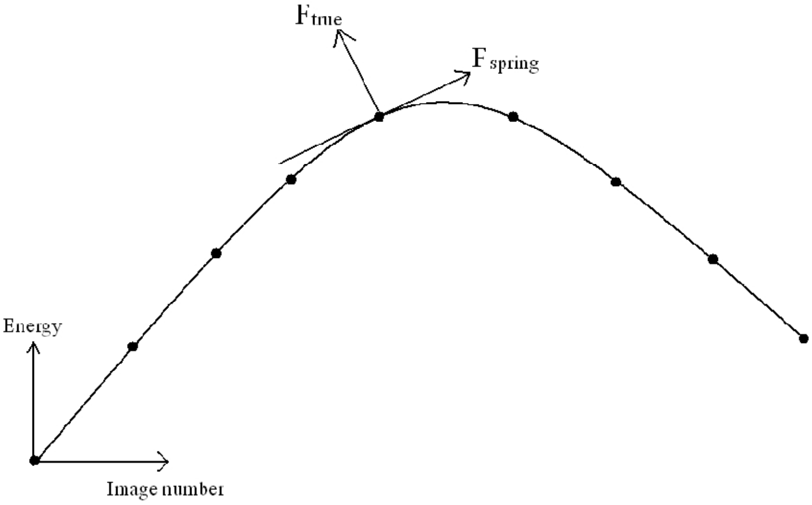

Figure 2.2: Energy vs. image number plot of a sample NEB calculation. The true and spring forces are shown for the highest energy image. Figure courtesy of Christine Bailey [(18)].

$$\begin{array}{ll} k_1 > 2k_2 & \\ k = k_1 - k_2 & E_i < \max\left(E_0, E_{N+1}\right) \\ k = k_1 - k_2\left(\dfrac{E_{\max} - \max\left(E_i, E_{i-1}\right)}{E_{\max} - \max\left(E_0, E_{N+1}\right)}\right) & E_i > \max\left(E_0, E_{N+1}\right) \end{array} \tag{2.36}$$

E_{max} denotes the highest energy of all images and E_i the energy of the *i*-th point. As mentioned before, E_0 and E_{N+1} are the energies of the initial and the final structures respectively. From this equation, we see that, close to the transition state, a stronger force will be applied, whereas images having energy lower than the energy of any one of the ending points will have the lowest spring force. This will allow the image density to increase around the transition state. It should be mentioned that, strictly speaking, k_1 does not have to be higher than $2k_2$, but it is strongly recommended, as very loose spring constants may make the distance between images very large.

The second solution is to allow only the highest image to move along the MEP, the correct way to do which is firstly to allow the NEB to have a loose convergence of the images (but nevertheless convergence) such that the highest image is in the neighbourhood of the transition state and the path is in the right area of the PES. At this point, the image with the highest energy is allowed to move along the MEP. If the first step is omitted, an image which may ‘accidentally’ have the highest energy could start climbing towards a wrong state. Instead of applying the force as defined in equation (2.32), the highest image has the force shown in eq. (2.37) acting on it.

$$\vec{F}_i = 2\left(\nabla E\left(\vec{R}_i\right)\right)_{\parallel} - \left(\nabla E\left(\vec{R}_i\right)\right) \tag{2.37}$$

The spring force on this image is neglected and the parallel part of the positive gradient of the energy is inverted. In the present research, both the variable force constant and climbing image methods were used and it was found that keeping the force constants fixed (but allowing climbing) leads to faster convergence, although in order to converge towards a transition state enough images should be produced in order to describe the MEP accurately. In particular, for the systems studied in this research, it was found that at least ten images were needed. Moreover, the force constant should be kept between 0.1 and 2 E_H/a_0^2 for the images not to diverge. The general performance of the NEB algorithm was evaluated using a small test system. Different combinations of force constants were used in searching for the transition state for the hydrogen exchange reaction $H_2 + H \rightarrow H + H_2$. The conclusion from this study was that, whereas general NEB theory assumes that the force constant can take any value, certain combinations of force constants made the sequence of images diverge, whereas other combinations gave accurate results. Further studies on the H_2O and CH_3OH systems showed that the choice of the optimal force constants is system dependent and that care should be taken when using this algorithm. As this was only a preliminary study, further investigation in this field will be needed in the future in order to alter and optimise this algorithm.

Synchronous Transit-Guided Quasi-Newton

The STQN algorithm, as implemented in Gaussian03, is a variation of the quadratic synchronous transit (QST) algorithm. STQN generates an estimate for the transition state and interpolates a second-order function between the initial state, the transition state and the final structures. The difference between the original QST and STQN is that in QST, the second-order function is a parabola, whereas in STQN the optimiser is constrained to use a circle arc to search for the transition state. Once the maximum energy is located, the optimiser will then switch to the standard Berny optimisation algorithm (20) to allow this structure to optimise towards the transition state. The Berny algorithm is an optimisation algorithm which uses the Hessian (which is the matrix containing the information about the forces) to generate a new geometry. Depending on the exact implementation of the algorithm, this geometry is created following either a linear or a polynomial interpolation of previous structures.

Algorithms: Hill-walking algorithms

The Drag method is a way of searching for a transition state where the assumption is made that, on going from a stable reactant (or a combination of reactants) towards the transition state, only one internal coordinate changes significantly. It is this one coordinate which will be changed stepwise, as at each step all other coordinates are allowed to relax. This leads to a one-dimensional PES from reactant(s) through transition state to the product(s). The highest point on this surface is usually a good estimate as a starting point for the optimiser, for example the Berny optimisation algorithm. For other algorithms the reader is referred to Henkelman's overview (19).

There are many algorithms for optimising structures, including those which require no derivatives (simplex), the first derivatives (steepest descent, conjugate gradient, dimer) and second derivatives (Newton-Rhapson); a description of the more common ones can be found in (6). Algorithms using the Hessian matrix (or an approximate second derivative matrix) for optimisation towards a ground state stable structure can be used to optimise towards a transition state once the structure is in the “region” of the transition state (e.g. the Berny algorithm which was mentioned above). Since the direction of the next optimisation step depends on the eigenvalues of the Hessian matrix, when one force eigenvalue is negative the system will optimise towards this local stationary point which is a transition state. At the end of an optimisation cycle, calculation of the forces (or similarly the frequencies) must be performed to verify whether the structure obtained is effectively a minimum or an n-th order saddle point.

Depending on the computer code, generally two algorithms were used. Gaussian03 uses the Berny algorithm (if necessary in combination with the STQN algorithm), since the second derivative matrix is available; Crystal06 uses NEB because the second derivative matrix can only be obtained numerically, which is a computationally very expensive procedure.

2.2. Computer Codes

Three different quantum chemistry codes have been selected and used in the calculations reported in this work. The selection procedure was based on the availability of algorithms within these codes and the speed at which the calculations can be performed. Ideally the program should have an optimisation algorithm for both minima and transition states and the implementation of hybrid functionals (preferentially meta-hybrid functionals) in order to obtain a reasonable representation of van der Waals interactions and barrier heights. To this end, reactions on coronene were studied with Gaussian03, which has meta-GGA functionals and can use high-level *ab initio* theory. Additionally, periodic boundary conditions need to be applied in order to study the infinite two-dimensional graphene surface. Crystal06, which allows the application of periodic boundary conditions but does not have meta-GGA functionals, was therefore used to study reactions on graphene. High-level *ab initio* benchmarking was performed with Molpro (21) since this program can handle larger basis sets in a more efficient way than does Gaussian03.

2.2.1. Gaussian03 and Molpro

Gaussian03 (22) is a connected system of different programs which can perform *ab initio* and DFT calculations. In particular, Gaussian03 is able to optimise stable structures, transition state structures, and calculate the corresponding energies and frequencies. The program is used worldwide and has become one of the standard quantum chemistry codes.

The capabilities of Molpro are comparable with Gaussian03, and it was used for high level *ab initio* benchmarking of gas phase calculations, since it treats large basis sets in a faster way than does Gaussian03. However because it is less user friendly it was only used for benchmarking purposes.

Gaussian03 was used for DFT gas phase calculations and for calculations on coronene (see Figure 2.3). Coronene, $C_{24}H_{12}$, is considered to be a good model for polycyclic aromatic hydrocarbons (PAHs) and has been used previously as the minimal model to model graphite, graphene, or PAHs (23-26). Coronene is large enough, such that adsorbed species do not interact with the hydrogen atoms (e.g. for the smaller benzene molecule the hydrogen atoms have a strong influence on the surface-adsorbate interaction), but not so big that it cannot be treated quantum chemically.

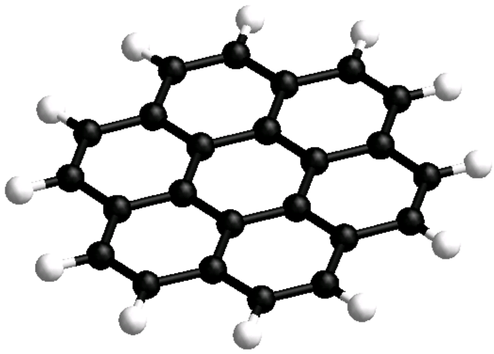

Figure 2.3: The molecule coronene, $C_{24}H_{12}$, which was used as a model for PAHs in this research. Carbon is black; hydrogen is white.

2.2.2. Crystal06

Crystal06 (27) is a periodic-system quantum chemistry program which can be used to perform *ab initio* and DFT calculations on 0D (molecules), 1D (polymers), 2D (slabs) and 3D (crystals) structures. These include optimisation, frequency calculation, generation of band diagrams and calculation of the density of states. A straightforward manipulation of the individual atoms within crystals makes it easy to calculate defects and their influence on physical properties. Crystal06 essentially differs from Gaussian03 in that it is designed for periodic systems, and is able to treat polymers, surfaces and crystals, whereas Gaussian03 is a molecular code. Wave functions within Crystal06 are expanded as Bloch functions of Gaussian orbitals. This approach ensures symmetry and the correct periodicity.

When studying defects or reactions on a surface, one needs to create supercells to avoid spurious interactions across images. A supercell is an integer expansion in all dimensions of a crystallographic cell (see Figure 2.4), thus increasing the number of atoms and the distances between the edges of the cell, but without loss of any symmetry, thus reducing interactions between adsorbates (or defects). The supercell must be large enough such that convergence with the supercell size has been reached and interactions between different adsorbates will be negligible. For example, consider a CO molecule adsorbed on graphene (Figure 2.5; graphene is a single layer of graphite and, as such, is a 2D crystal). When no supercell is used (left image), the CO molecules will interact with each other (as shown by the red lines connecting the oxygen atoms). A 3x3 supercell of

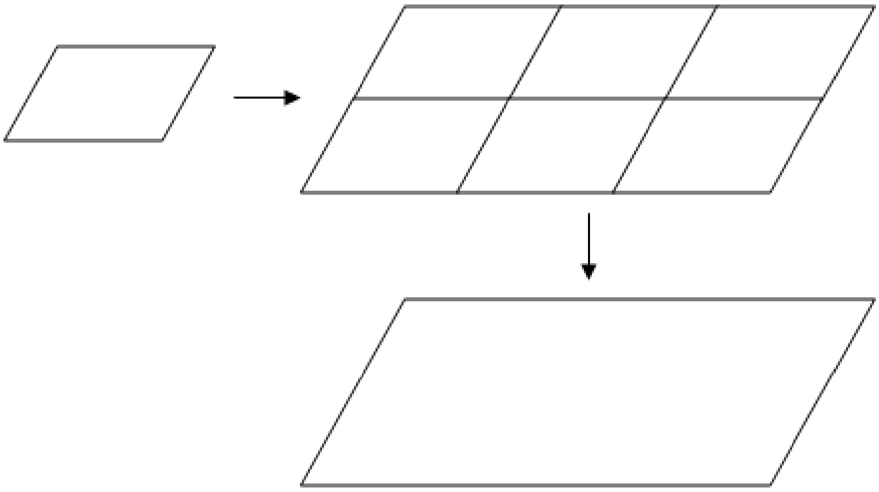

Figure 2.4: A 2D cell (the top left parallelogram) is changed into a 3×2 supercell (the top right combination of parallelograms). The cell is multiplied, after which the cells are joined together to form a new, larger, cell (the bottom, larger parallelogram). The creation of this supercell will decrease the interaction of any atom with its next-cell image.

the graphene primitive cell, however, is large enough to avoid such interactions. A CO molecule added into this supercell will have no significant interactions with the CO molecule in the next cell. Results on a graphene surface reported in this work were always performed on a 4x4 supercell.

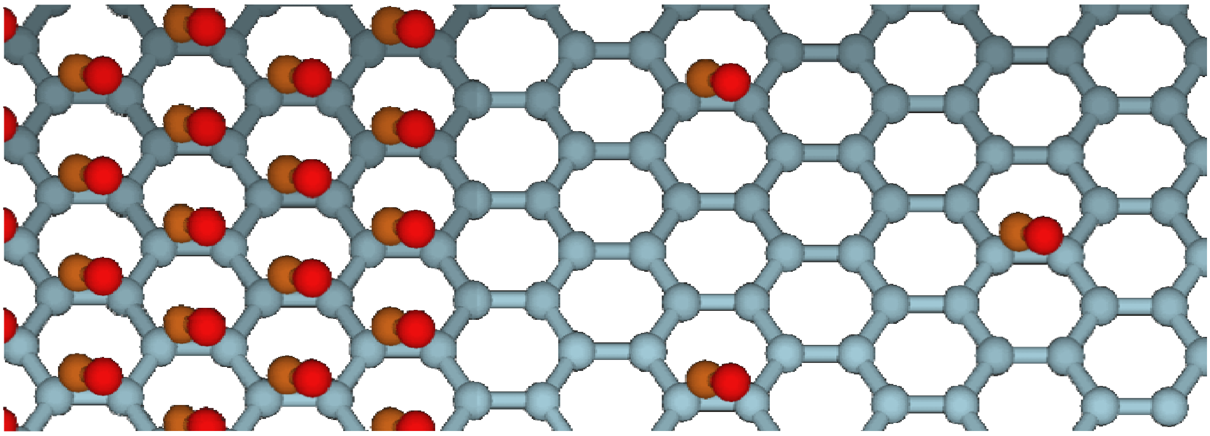

Figure 2.5: CO is added onto a graphene sheet – graphene carbon is depicted as the grey spheres, CO carbon is brown, oxygen is red. The left hand picture shows one CO molecule per unit cell of graphene. Clearly the CO molecules interact with each other. In the right hand picture, one CO molecule is added per 3x3 supercell of graphene, increasing the distance between the CO molecules and thus decreasing the interaction between adjacent CO molecules.

2.2.3. Functionals

The main interactions which were of importance in this research are chemical bonding and physisorption on a surface. Moreover, not only stable structures but also transition states were optimised, and both closed shell structures and radicals were used in the reactions. The functionals used in this work should be able to represent all of these interactions and structures correctly. Those include the PW1K and MPWB1K functionals. The MPWB1K functional was developed by Zhao and Truhlar (10) and is shown to be better at representing both barrier heights and dispersion forces than most other functionals. This functional is composed of Becke's B95 correlation, 56% MPW91 exchange and 44% exact exchange ((10) and references therein). This functional could unfortunately only be used within the Gaussian03 package (thus for reactions on a coronene surface), since it is not implemented in Crystal06. The second functional used, both within Crystal06 and Gaussian03, is a new functional based on the PW91 functional by Perdew and Wang (28). It constitutes of PW91 correlation, 57.2% PW91 exchange and 42.8% exact exchange. The parameter 42.8% was not reoptimised, but rather taken from the previously published MPW1K functional by Adamo and Barone (9) (which has the same correlation, but uses the MPW functional for exchange). Based on this similarity the functional was named PW1K. This functional had to be used, rather than MPW1K, since the Crystal06 computational package (27) does not contain the MPW functional. The new PW1K functional is a hybrid functional which can be easily recreated in a wide variety of software packages, and calculations with MPWB1K and PW1K have been compared within the Gaussian03 code. Since MPWB1K has previously been shown to reproduce physisorption energies, it can be used as a benchmark for our own calculations with the PW1K functional.

2.3. Summary

In this research, two different methods were used to optimise and evaluate both ground state and transition state structures: WFT and DFT. WFT was used for benchmarking DFT. The approach used was CCSD(T) on an aug-cc-pVTZ basis set. Within the DFT scheme, two different functionals were used: MPWB1K, a functional which was shown to represent physisorption energies, barrier heights, geometries and energies; and PW1K, a functional which was created for this work and is closely related to the previous functional.

Two programs were used: Gaussian03 for molecular structures, and Crystal06 for periodic structures. Standard optimisation techniques were applied to obtain local minima, and both STQN and NEB were used to obtain transition state geometries and energies.

2.4. References

1. Hohenberg, P., *Phys Rev B*, 1964, **136**, B864.
2. Kohn, W. and Sham, L. J., *Phys Rev*, 1965, **140**, 1133.
3. Szabo, A. and Ostlund, N. S., *Modern Quantum Chemistry*, Dover, 1989.
4. Koch, W. and Holthausen, M. C., *A Chemist's Guide to Density Functional Theory*, 2 edn., Wiley-VCH, 2002.
5. Martin, R. M., *Electronic Structure: Basic Theory and Practical Methods*, Cambridge University Press, 2005.
6. Jensen, F., *Introduction to Computational Chemistry*, 2 edn., Wiley, 2007.
7. Sousa, S. F., Fernandes, P. A. and Ramos, M. J., *J Phys Chem A*, 2007, **111**, 10439.
8. Perdew, J. P. and Schmidt, K., Density Functional Theory and its Application to Materials, Antwerp (Belgium), 2001.
9. Adamo, C. and Barone, V., *J. Chem. Phys.*, 1998, **108**, 664.
10. Zhao, Y. and Truhlar, D. G., *J Phys Chem A*, 2004, **108**, 6908.
11. Koch, W., 2002.
12. Hehre, W., *J. Chem. Phys.*, 1969, **51**, 2657.
13. Zhongxiang, Z., *J. Phys. Org. Chem.*, 1995, **8**, 103.
14. Cioslowski, J., O'Connor, P. B. and Fleischmann, E. D., *J. Am. Chem. Soc.*, 1991, **113**, 1086.
15. Goumans, T. P. M., Uppal, M. A. and Brown, W. A., *Mon. Not. R. Astron. Soc.*, 2008, **384**, 1158.
16. Eyring, H., *J. Chem. Phys.*, 1935, 107.
17. Truhlar, D., *Account Chem Res*, 1980, **13**, 440.
18. Bailey, C. L., Wander, A., Searle, B. G., et al.
19. Henkelman, G., Johannesson, G. and Jonsson, H., in *Theoretical Methods in Condensed Phase Chemistry*, Editon edn., 2000, vol. 5, pp. 269.
20. Schlegel, H. B., *J. Comput. Chem.*, 1982, **3**, 214.
21. Werner, H.-J., Knowles, P. J., Lindh, R., et al., *MOLPRO, version 2006.1, a package of ab initio programmes*.
22. Frisch, M. J., Trucks, G. W., Schlegel, H. B., et al., *Gaussian, Inc., Wallingford CT*, 2004.
23. Galano, A., *J Phys Chem A*, 2007, **111**, 1677.
24. Xu, S. C., Irle, S., Musaev, D. G., et al., *J Phys Chem B*, 2006, **110**, 21135.
25. Mendoza, C., Ruette, F., Martorell, G., et al., *Astrophys. J.*, 2004, **601**, L59.
26. Morisset, S., Aguillon, F., Sizun, M., et al., *Phys Chem Chem Phys*, 2003, **5**, 506.
27. Dovesi, R., Saunders, V. R., Roetti, C., et al., ed. Torino, U. o., Torino, Editon edn., 2006.
28. Perdew, J., *Phys Rev B*, 1996, **54**, 16533.

Water

Chapter 3

3.1. Astronomical importance of water

3.1.1. Introduction and importance of water

As mentioned in Chapter 1, hydrogen is the most abundant atom in the universe, and therefore hydrogenation is the most common chemical reaction. Free atoms (e.g. O, N and C) will most likely be hydrogenated until a stable molecule is formed (e.g. H_2O, NH_3, and CH_4). Astrochemical models have been developed that take into account many channels of formation and destruction for different molecules of which the presence in the ISM has been confirmed. Key factors for these channels are not limited to the activation barriers, but also include many external factors like temperature, radiation fields (including cosmic and electromagnetic radiation), and species (atoms, molecules, ions) densities. The first astrochemical models used only gas phase reactions. For many molecules, however, heir detected abundance in the interstellar medium (ISM) cannot be explained by solely considering gas phase reactions (1-8). These models predict abundances, depending on the molecule, one to several orders of magnitude lower than those that are sometimes observed (5-8). A possible assumption which may overcome this problem is that surface reactions, in addition to gas phase reactions, may be responsible for the formation of these overabundant molecules.

The chemical and physical nature of dust grains will play a crucial role in determining whether a certain surface reaction will effectively occur. Surfaces can accrete material, which is an important effect, since in the ISM the pressure is very low, around 10^{-14} mbar. At such low pressures, it is more meaningful to talk about number densities: 10,000 cm^{-3}. Surfaces accreting molecules and atoms will enhance the probability of collisions between two adsorbed particles, as long as the adsorption energy is high enough for the particles not to desorb, and low enough (i.e. it is in the physisorption region, between 0 and 60 kJ mol^{-1}) to allow for the particles to be mobile at very low temperatures. Surfaces can also absorb energy in the form of vibrational motion. More specifically the formation energy of newly formed molecules can be transferred to the surface, reducing the probability of them dissociating into their initial reactants. The efficiency with which the transfer of energy happens depends, amongst other things, on the strength of the surface – adsorbate bond. Finally the surface can chemically catalyse a reaction, lowering the activation barrier with respect to the reaction in the gas phase. Thus, it is important to examine the adsorption energies of the reactants on a surface, and the change in activation energies of reactions with respect to their gas phase counterparts.

In the ISM, ion chemistry is of major importance. Cosmic rays and electromagnetic radiation (most likely ultraviolet) can excite and ionise molecules and these ionic species can, as is the case for radicals, survive for very long periods in the low pressure environment. Many reactions are barrierless when charged species are involved and as such the relative contribution of ion-neutral reactions with respect to neutral-neutral reactions increases.

Water is one of the simplest molecules in the universe, and it is also one of the most abundant ones. Many of the ices occurring in the ISM contain water as the most important fraction, usually mixed with other molecules like CO or methanol, and often deposited on a dust grain surface. Water is in fact the most abundant solid material in space (1), and most ices in the ISM will therefore largely be composed of water (1). As it is very abundant, it is very likely that water is involved in the catalysis of other molecules, or forms a crucial part of their chemical network. In fact, Woon (6) has shown that water has a catalytic effect on methanol formation. The formation of water is however not entirely understood and there is much debate about how it is formed and how much every possible formation pathway contributes to the total water formation. In addition, water is also one of the molecules whose abundance cannot always be explained by exclusively considering gas phase reactions (both neutral-neutral and ion-neutral) (1-4). Since water is mostly concentrated in ices and on dust grains, it is very plausible to assume these may catalyse the formation of water, hence enhancing the production of water molecules in the ISM (1-4, 9-11). Dust grains, as explained in the first chapter, are thought to be composed of a siliceous core, surrounded by a carbonaceous mantle, and possibly covered in ices (including water and methanol ice). Charged reaction channels to water formation exist and are very important in the gas phase, but carbonaceous dust grains, as studied in this research, will neutralise ionic species (or delocalise their charge over the entire surface) and it is therefore not relevant to study these reactions here. However, it has been shown that charged surfaces – which is computationally equivalent to a charged species which hits a neutral surface – can catalyse some reactions (12, 13).

The main aim of this research is to study the influence of two carbonaceous model dust grain surfaces, graphene and coronene, on the reactants and products of water formation. Chemically speaking, both surfaces used are perfect, without any defects or charges. They are very similar to each other and therefore when these surfaces are used as models, similar results are expected. Computationally speaking however, there are major differences concerning the methods which can be used, the computational power available, and the experimental reproducibility and significance of the computational results. The surfaces differ in size: coronene is a molecule; graphene is a two dimensional periodic (and thus infinite) surface. Two different programs were used to calculate adsorption and reactions on these surfaces, with two different DFT functionals. The difference between the obtained results will briefly be discussed.

Here, both surfaces were used to examine one reaction. As is explained further, the most important reactions to water formation are barrierless, hence a surface cannot catalyse the reaction and reduce an absent activation barrier. The reaction $OH + H_2 \longrightarrow H_2O + H$ however is not barrierless, but it can also contribute to water formation (1, 2, 9, 10). This reaction is examined in detail. The gas phase activation barrier of this reaction is slightly too high for it to occur in the gas phase and any catalytic influence that a surface may have is thus very important.

3.1.2. Potential formation reactions of water

Water formation in the gas phase has been researched thoroughly, and as such the chemical network is very extended. Table 3.1 shows (a subset of) chemical reactions involving water and OH formation and destruction, which are thought to happen in the ISM (14). As a matter of fact, H_3^+ is believed to be a key molecular ion in the ISM gas phase reactions (15), which is also involved in one of the major reaction pathways for water formation in the gas phase (as shown below). Figure 3.1 shows the importance of the H_3^+ ion (figure taken from ref. (15)).

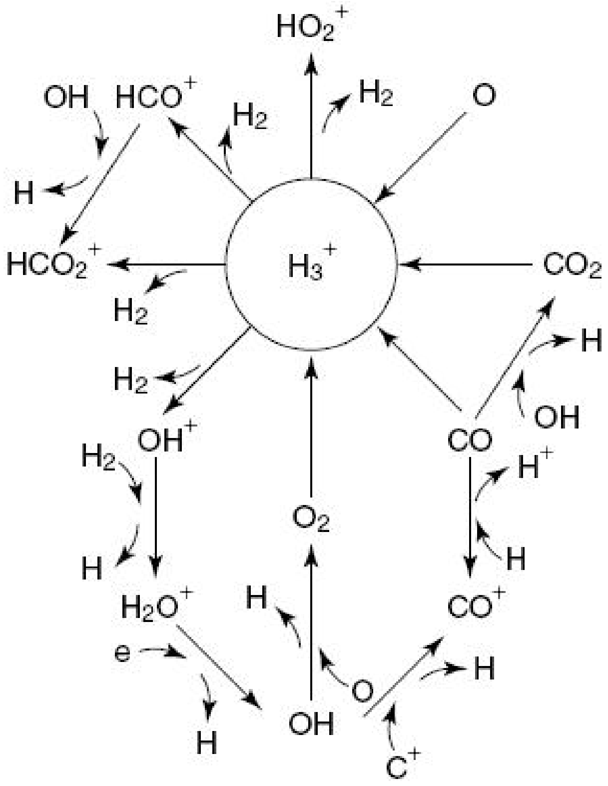

Figure 3.1: Importance of the H_3^+ ion (and ions in general) in the ISM.

A plausible ionic pathway for water formation in the ISM gas phase is shown below:

H_2 + cosmic rays $\longrightarrow H_2^+ + e^{-\,*}$

$H_2^+ + H_2 \longrightarrow H_3^+ + H$

$H_3^+ + O \longrightarrow OH^+ + H_2$

$OH^+ + H_2 \longrightarrow H_2O^+ + H$

$H_2O^+ + H_2 \longrightarrow H_3O^+ + H$

$H_3O^+ + X \longrightarrow H_2O + HX$

Table 3.1: Chemical reactions, involved in water and OH formation, which are thought to happen in the ISM.

Formation of OH	Formation of H_2O
Alcohol + photon $\rightarrow$ [...] + OH	$H_2O^+ + X \rightarrow H_2O + X^+$ (e.g. Si, ...)
Alcohol$^+$ + e$^-$ $\rightarrow$ [...] + OH	$H_3O^+ + X \rightarrow H_2O + HX^+$ (e.g. C_2, C_2H_3, C_2H_5OH, C_2O, C_2S, ...)
$CH + XO \rightarrow CX + OH$ (e.g. NO, O_2, O, HO_2, H_2O^+, ...)	$OH + H \rightarrow H_2O$
$CH_2 + XO \rightarrow CHX + OH$ (e.g. NO, O_2, O, H_2O^+, ...)	$OH + H_2 \rightarrow H_2O$
$H + XO \rightarrow OH + X$ (e.g. CO, CO_2, H_2O, H_2O_2, NO_2, NO_2^+, O^-, ...)	$H_2O_2 + H \rightarrow H_2O + OH$
$O + HX \rightarrow OH + X$ (e.g. H_2CO, H_2O, H_2O_2, H_2S, H_2S^+, HCO, HCN, HNO, ...)	Formation of H_2O^+
$H + O \rightarrow OH$	$H_2 + OH^+ \rightarrow H_2O^+ + H$
$H_2 + O \rightarrow OH + H$	$H_3^+ + OH \rightarrow H_2O^+ + H_2$
Formation of OH^+	$OH + HX^+ \rightarrow H_2O^+ + X$ (e.g. HO_2^+, HNO^+, HCO^+, HCN^+, ...)
$H_2 + O^+ \rightarrow OH^+ + H$	$OH^+ + HX \rightarrow H_2O^+ + X$ (e.g. HCO, OH, H_2O, ...)
$H_2^+ + O \rightarrow OH^+ + H$	Formation of H_3O^+
$H_3^+ + O \rightarrow OH^+ + H_2$	$H_2 + H_2O^+ \rightarrow H + H_3O^+$
	$HCO + H_2O^+ \rightarrow CO + H_3O^+$
	$H_2S + H_2O^+ \rightarrow HS + H_3O^+$

Figure 3.2 shows only neutral-neutral chemical reactions thought to contribute to water formation in the ISM (1, 2, 9-11, 16, 17), and the important atoms, radicals and molecules involved in this network. Only neutral-neutral reactions need to be investigated here, since surfaces and/or dust grains are involved, and charges will either be neutralised by, or delocalised on, the surface. Even though on surfaces any charges present will most likely be neutralised or delocalised and hence play a less important role than they do in the gas phase, the ion chemistry is an important possibility which should be researched in the future.

The factors determining whether a particular reaction will proceed are the abundances of the reactants involved, the activation barrier (if there is a barrier), and competing reactions (if any) which would reduce the abundance of the reactants. These factors have been investigated in this and in previous research (1, 9-11, 14-24). The astrochemical programs which have been mentioned in Chapter 1 use rate equations or more sophisticated methods like Monte Carlo random walk (11, 25-27) to calculate the abundance of every neutral or charged molecule and atom available in the program, as a function of time. At the end of this chapter, an example of these rate equations will be shown and explained in detail.

The most straightforward neutral-neutral reaction pathway to form water in the ISM is to successively hydrogenate an oxygen atom with hydrogen atoms, to yield water in two steps (1-4, 9-11, 19, 20). In dark molecular clouds, hydrogen is however mostly present as hydrogen gas, H_2. Thus another, more likely, possibility is to use H_2 as a source of hydrogen to create water from an oxygen atom (1-4, 9, 19, 20). A third possible reaction pathway goes via the formation of oxygen gas (O_2) and hydrogen peroxide (H_2O_2), and was proposed by Tielens et al. (17) Finally oxygen gas can form ozone, which in turn can be hydrogenated to form oxygen gas and a hydroxyl radical (1, 3, 4, 9, 19, 20). These reactions are numbered (1) to (8) and shown below Figure 3.2. Multiple formation pathways exist to form OH, including $CH + O_2$, $CH_2 + O$, $CH_2 + O_2$, $H + CO_2$, $H + N_2O$, and the dissociation of alcohols (28, 29).

$$O + H \rightarrow OH \tag{1a}$$

$$O + H_2 \rightarrow OH + H \tag{1b}$$

$$OH + H \rightarrow H_2O \tag{2a}$$

$$OH + H_2 \rightarrow H_2O + H \tag{2b}$$

$$O + O \rightarrow O_2 \tag{3}$$

$$O_2 + H \rightarrow HO_2 \tag{4}$$

$$HO_2 + H \rightarrow H_2O_2 \tag{5}$$

$$H_2O_2 + H \rightarrow H_2O + OH \tag{6}$$

$$O_2 + O \rightarrow O_3 \tag{7}$$

$$O_3 + H \rightarrow O_2 + OH \tag{8}$$

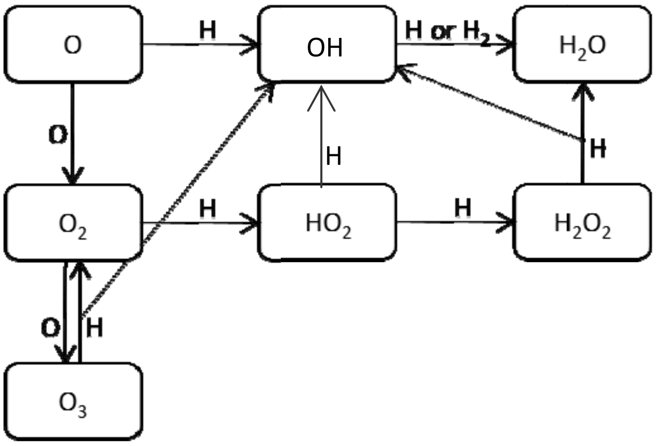

Figure 3.2: Part of the chemical network for reactions possibly involved in water formation. Reactions can proceed in the gas phase or on a surface.

Abundances

Water is one of the most abundant species in the ISM. Table 3.2 shows the abundances of several molecules, including the four most abundant species in ices (water, methanol, CO and CO_2) (18). The hydroxyl radical is present in dark clouds (30) in relatively high abundances, about two orders of magnitude higher than methanol. This suggests that either OH is formed in the gas phase or that OH forms on a dust grain and then evaporates from this grain. No OH detection in ices was reported in a review by van Dishoeck *et al.* (18), supporting the assumption that OH, upon formation, is so energetic that it immediately desorbs from the grain surface. It can then re-adsorb on a surface to react, forming other molecules (e.g. water), or it can undergo reactions in the gas phase, possibly via an ion-neutral channel.

Table 3.2: Observed abundances for species in the water formation pathway, in dark molecular clouds (TMC-1 and W33A). CO, CO_2 and CH_3OH have been included for comparison purposes, as they are the most abundant molecules in ISM ices. CD = Column Density, Ab = Abundance relative to H_2.

Molecule	**CD in W33A** (31), $/10^{-17}$ cm^2	**Average CD** (31), $/10^{-17}$ cm^2	**Ab in TMC-1** (30)	**Ab in ices** (18)
H_2O	110	12.5 – 120	---	5×10^{-5}
OH	---	---	3.0×10^{-7}	---
HDO	0.3	---	---	---
CO	8.9	1.00 – 18.0	8.0×10^{-5}	$1 \times 10^{-6} – 10 \times 10^{-6}$
CO_2	14.5	0.38 – 6.60	---	8×10^{-6}
CH_3OH	19.5	0.50 – 36.0	2-3 $\times 10^{-9}$	4×10^{-6}

3.2. Previous work

Water formation via the various routes shown in Figure 3.2 has been researched both theoretically and experimentally. The routes mentioned in this figure were first suggested by Klein and Scheer in 1959 (19). Unfortunately no verification of the intermediate products (including H_2O_2) was performed, leaving the question open as to whether all of these reaction pathways are actually valid, or whether the contribution of some of the pathways is insignificant. Later simulations by Cuppen and Herbst (1, 20) led to the suggestion that that reactions (1a) and (2a), involving hydrogenation of oxygen atoms and the hydroxyl radical by hydrogen atoms, would be the dominant route to water formation in diffuse clouds, whereas the other pathways would be the primary ones in dense molecular clouds. Since the former clouds allow both cosmic radiation and ultraviolet light to penetrate, many molecules are dissociated and plenty of atoms are formed. The latter clouds are too dense for UV radiation to penetrate the cloud and dissociate H_2, however cosmic rays can penetrate this far and UV radiation can be formed *in situ*, inside the cloud.

The reactions shown in Figure 3.2 under gas phase conditions have been investigated computationally and the results will be shown in the next section. The only difference between reactions with H_2 rather than with H is, thermodynamically speaking, the dissociation of the former into two hydrogen atoms, thus the difference in reaction energy equals the strength of the hydrogen bond. For this reason, reactions with H_2 as one of the reactants are approximately 400 kJ mol^{-1} less exothermic than the corresponding reactions with H.

Reaction of H_2 with an oxygen atom ($O + H_2 \rightarrow OH + H$, reaction 1b) is an endothermic reaction and will thus not occur in the ISM. Since hydrogen predominantly occurs in molecular form in dense clouds (15), this allows for molecules like O_2 to be formed. Once formed, O_2 can then react with atomic hydrogen to form H_2O_2 and eventually H_2O (1-4, 9, 19, 20), even though hydrogen is mostly trapped as H_2. The possibility also exists that water may be formed from H_3O^+ (15); in diffuse clouds H_3^+ is believed to be a key molecular ion (15). However, since the fraction of molecules and atoms which are ionised in these dense molecular clouds is very low (between 10^{-4} and 10^{-8}), the pathways using ionised species are very unlikely to contribute significantly (21).

O_2 and H_2 will not react with each other to form water in the ISM (1). Direct formation of water needs to be catalysed (as is commonly shown in the 'squeaky pop test'). Formation of two OH species from $O_2 + H_2$ would require an activation barrier of more than 180 kJ mol^{-1} to be overcome (14, 24). Bearing in mind that dark molecular clouds in the ISM have temperatures of 20 K or lower, reaction of O_2 with H_2 can be excluded from any further research (15). It has also been shown (15) that water formation at temperatures below 300 K is less effective via $O + H_2$ and $OH + H_2$, but more effective via $O + H$ and $OH + H$.

Previous theoretical studies are composed mainly of gas phase reactions as these are easier to study. Data on surface reactions is however very scarce (1). A study by Das et al. (10) used a Monte Carlo simulation for water and methanol formation, both in the gas phase and on an olivine surface. Only hydrogen (H), oxygen (O) and CO were used as starting species, and only surface reactions were allowed (i.e. no gas phase reactions). Ten reactions were included, allowing for the creation of the molecules H_2, O_2, H_2O, CO_2, H_2CO and methanol. Their study showed that, starting with number densities for H, O and CO ranging from 0.075 to 7.5 particles cm^{-3} (which were obtained via calculations, where the H_2 number density was varied from 10^3 to 10^5 cm^{-3}), the equilibrium abundance of water was between 10^{-10} and 10^{-9} with respect to the gas phase H_2 abundance. The water abundance reached 10^{-4} with respect to total hydrogen column density, and clearly showed that it was the most abundant molecule on the grains (3 to 20 times more abundant than methanol, in agreement with astronomical observations). The reaction activation barriers for H_2O and CH_3OH formation used in these calculations are however approximate only (10, 11, 22), stressing the importance of the present research.

A computational study on water formation performed by Jelea et al. (23), showed that diffusion barriers of at least 14 kJ mol^{-1} need to be overcome in the cases where O, H or OH are chemisorbed on a graphite surface. The barriers computed here will very likely be higher than the ones shown in Jelea's publication because of the method which was used (the PBE functional was employed here). The barriers are already relatively high under ISM conditions, which makes chemical sense as bonds need to be broken in order for the species to move over the surface and come close enough to each other in order to react. For this reason, for studies concerning reactions in the ISM, chemisorption is much less important than physisorption, where only a few kJ mol^{-1} are needed for desorbing an atom or a molecule. Another important observation made in Jelea's publication (23) is that graphite, as a surface, is an electron reservoir. The unique properties of graphite (and also graphene) of acting as a (semi-)metal ensure that electrically charged species will immediately lose their charge, once they bond to the graphite surface. Therefore, when a graphite or a graphite-like surface is considered as a dust grain, it is not necessary to study ionic reactions on the surface. Finally, (23) used quantum molecular dynamics, and in their simulations of OH formation, the OH radical desorbs from the surface, despite it being chemisorbed. Re-adsorption of the OH radical would then be the next step necessary for water formation, considerably slowing down the process. It was however suggested that, if OH happens to be hindered (e.g. it is stuck between two graphene sheets), it may not desorb. Defective graphene sheets may also help prevent immediate desorption.

Stantcheva *et al.* (11) studied the formation of CO_2, methanol and water computationally and showed that the use of rate equations as an astronomical model breaks down when the coverage of dust grains become very low, of the order of one or less molecules per dust grain. Instead, they show that the use of a Monte Carlo approach or a master rate equation approach is more accurate. They report that unfortunately, the use of these methods is very limited since the time needed to solve the equations scales exponentially with the number of species included.

Reactions (1a) and (2a), O + H and OH + H, are both barrierless (1) and extremely exothermic (9), both in the gas phase and on a surface. However, most hydrogen in dark clouds is trapped as H_2 (H is about 4 orders of magnitude less abundant than H_2 (10)). Radiative association is extremely inefficient (15), which also prevents reactions (1a) and (2a) from proceeding, unless a third body is present. These reactions are hence insufficiently effective to provide the amount of H_2O which has been observed.

Experiments have also been performed to test these reactions, however it was unclear whether the water and OH were formed during irradiation or upon heating of the sample (1, 9). Hiraoka *et al.* (9) studied water formation via reactions (1a) and (2a), and reported that the hydrogenation of oxygen atoms on dust grains seems likely to be very efficient. They also state that the reaction of OH with H_2, reaction (2b), may be important, since the predicted rate constant of 2 x 10^{-15} cm^3 $molecule^{-1}$ s^{-1} is large. However, this rate constant is for a temperature of 250 K, and includes tunnelling.

Recently, Dulieu *et al.* (3, 4) studied the same reactions using amorphous solid water as the surface. Using two atomic beams, one of deuterium atoms and one of oxygen atoms, they irradiated the surface at a temperature of 10 K under ultra-high vacuum conditions, and concluded that water formed under those conditions. At temperatures higher than 20 K, they noted that D atoms would desorb from the ice, hence preventing water being formed during the warm-up necessary for their detection method (temperature programmed desorption). They also tried to form water via D_2 + O and D_2 + O_2 and showed that, at this temperature, these reactions do not proceed.

Reaction (1b) is endothermic and has a gas phase activation barrier of around 26 kJ mol^{-1} (the reported values are 26.33 kJ mol^{-1} (24) and 26.25 kJ mol^{-1} (14)) and is therefore unlikely to happen in dark clouds. Once OH is formed however, it can react with H_2 to form H_2O. The activation barrier in the gas phase is also relatively high (reported to be 13.83 kJ mol^{-1} (24), 14.47 kJ mol^{-1} (14) and 21.59 kJ mol^{-1} (1)), such that a reduction of this barrier by a dust grain would be necessary for this reaction to proceed. The reaction is exothermic, with a reaction energy of -62.76 kJ mol^{-1} (9). OH itself needs to be formed via a route other than (1b). The 4-step mechanism, via H_2O_2, leads to both OH and H_2O production. Addition of two oxygen atoms (reaction (3)) is barrierless for the same reason as reactions (1a) and (2a): the addition of two radicals is usually barrierless, especially in the case of two atoms.

Miyauchi *et al.* (1) performed experiments on the formation of water via O_2 and hydrogen peroxide, as suggested in reactions (4), (5) and (6). Reaction (4), the addition of H to O_2, is an example of an exception to the radical-radical addition, since the bond formed between the hydrogen atom and the O_2 (diradical) molecule will be via the O_2 antibonding π^*-orbital, reducing the stability of the oxygen-oxygen bond. The barrier was shown to be very low (1), estimated to be between 0.42 and 1.67 kJ mol^{-1} (1, 32). O_2 + H will not break the oxygen-oxygen bond however, since this reaction is endothermic (+71 kJ mol^{-1} (32)). The hydrogen peroxide forming reaction (5) is, again, barrierless (1), and hence hydrogen peroxide formation via reactions (4) + (5) is very efficient.

Hydrogen peroxide can react with a hydrogen atom to form water + OH as in reaction (6), with an activation barrier between 15 and 18 kJ mol^{-1} (1, 14). The barrier is relatively high and, because experiments have shown this reaction to be fast, it is suggested to go via quantum tunnelling of the hydrogen atom (1). However, the experiments also showed a constant concentration of H_2O_2, suggesting that the barrier for reaction (6) is high enough for a large amount of hydrogen peroxide to be formed. Experiments which replace hydrogen with deuterium atoms (1) show that indeed the rate of reaction (4) barely changes, implying there is a very small barrier for this reaction, and that the rate of reaction (5) is reduced by a factor of 8, implying a barrier of the order of 13 kJ mol^{-1} (33). These ultrahigh vacuum experiments have confirmed that, below 70 K, firstly hydrogen peroxide is formed rapidly and efficiently, shortly after which water is formed. Reaction rates were compared with the first step in methanol formation (see chapter 4), and were estimated to be two orders of magnitude larger than CO + H (1). No observation of the intermediate radical HO_2 was made, showing that the reaction of this radical with H is much faster than the formation of this radical from H and O_2 (1).

Ioppolo *et al.* (2) have studied water formation via hydrogenation of O_2 ice. They show, in agreement with Miyauchi *et al.* (1), that hydrogen peroxide is easily formed. The rate of reaction to H_2O_2 formation was reported to be temperature independent, suggesting a small activation barrier for reactions (4) and (5), $O_2 + 2\ H \rightarrow H_2O_2$. The authors reported that the activation barrier was lower than 10 kJ mol^{-1}, which was a previously assumed barrier (17). Again, however, the H_2O_2 (and D_2O_2) column density increased to a constant value, around 5 times larger than the water column density. The column density of the peroxide remaining constant suggests that a larger activation barrier needs to be overcome, in order to proceed to water formation (if the activation barrier to water formation would be small or negligible, the peroxide column density would not reach such a high value compared to water). The authors suggested a model taking into account the penetration depth of H into O_2 ice, which accurately reproduced the temperature dependence of the observed reaction rate. Assuming that this depth is different for H_2O_2 ice, the experimental temperature dependence of the water formation reaction rates also agreed with the model. They stated that, since in dense gas no H_2O_2 or water is observed, and since most oxygen atoms have recombined to form O_2, most of the O_2 does not react to form hydrogen peroxide or water. However the difference in their model is that interstellar ices are not exclusively built up from O_2 and therefore the penetration depth of the hydrogen atoms is different from the depth measured in the laboratory. Their model also showed that the formation of water via ozone, reactions (7) and (8), is approximately 5 orders of magnitude lower than its formation via hydrogen peroxide, and formation via O + H.

Reactions (7) and (8), which add another possible route to OH formation via O_3, were suggested by Tielens and Hagen (17) and Hiraoka et al. (9). However, no data was found in the literature on this possible reaction pathway. Possibly the activation barrier of ozone formation, reaction (7), is too high for ozone to efficiently form. The UMIST database for astrochemistry (14) does not contain any data on ozone, suggesting that there is no experimental data available.

3.3. Validation and benchmarking

3.3.1. Methodology

The relative DFT energies of all gas-phase molecules were benchmarked against high-level CCSD(T)/aug-cc-pVTZ calculations, using the Molpro program (34). Two different surfaces were used to study the hydrogenation of OH with H_2: graphene and coronene. Graphene is a periodic (infinite) surface, and calculations were performed using the Crystal06 code (35), with the PW1K/6-311G** level of theory. As mentioned in Chapter 2, the experimental NEB code of Crystal06 was used to obtain the structures and geometries of transition states. Reactions on coronene were studied using Gaussian03 (36), with the MPWB1K/6-311G** level of theory, where a standard algorithm was used for transition state calculations. Details of the programs, DFT functionals and basis sets were described in Chapter 2.

3.3.2. Validation and benchmarking

Firstly, DFT gas phase values were validated against high-level *ab initio* theory. The excellent agreement between CCSD(T) calculations on the one hand, and DFT calculations and experimental results on the other hand, can be seen in Figure 3.3 and Table 3.3. Both the figure and the table show the gas phase reaction energies for CCSD(T), PW1K and MPWB1K calculations, for reactions involved in the water formation pathway, as shown in Figure 3.2. Fitting a straight line by means of the least squares method shows that, with a goodness of fit value $R^2_{MPWB1K} = 0.9989$ and $R^2_{PW1K} = 0.9993$, on average, DFT results are between 2.5 and 9.3 kJ mol^{-1} lower in energy with respect to the

CCSD(T) results. The experimental values for these reactions are based on the online CCCDBD (28) formation enthalpies, extrapolated to 0 K, and are shown in the right hand column. An excellent agreement between experimental values on the one hand, and CCSD(T) and DFT results on the other hand can be seen; R^2 values range from 0.9958 (for CCSD(T) results) to 0.9984, with DFT values on average 3.5 kJ mol^{-1} more or less than the experimental values. Based on these results, both PW1K and MPWB1K are acceptable functionals for the present study. The minor disagreement between the DFT and the CCSD(T) values shows that, compared to experimental values, DFT overestimates and CCSD(T) underestimates the reaction energies. However DFT values are very close to the experimental values, hence the major error is probably situated in the CCSD(T) results.

Figure 3.3: DFT energies vs. CCSD(T) energies for reactions involved in water formation, as shown in Figure 3.2 and Table 3.3. Axis values are in kJ mol^{-1}.

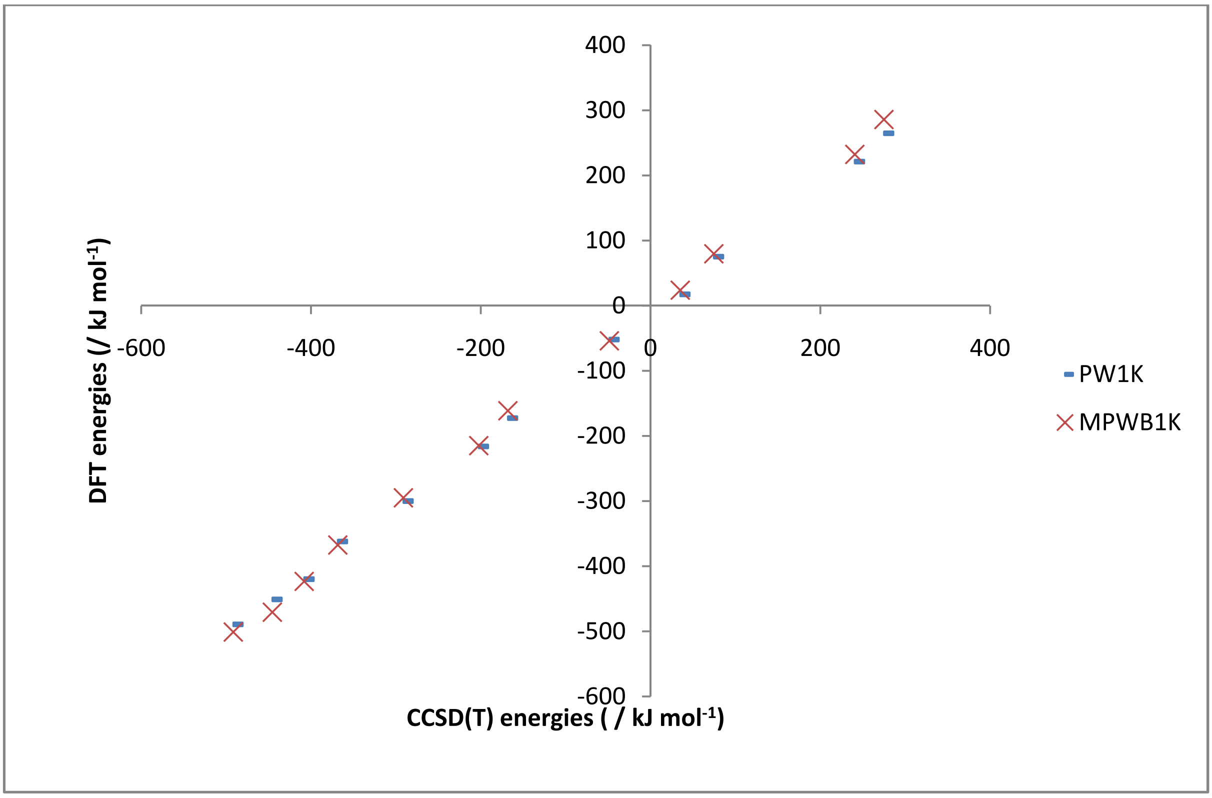

	CCSD(T) **[This work]**	**PW1K** **[This work]**	**MPWB1K** **[This work]**	**Experimental** **CCCBDB**[28]
$O + H \rightarrow OH$	-407.94	-419.81	-423.18	-425.83
$O + H_2 \rightarrow OH + H$	35.03	17.43	23.91	6.25
$OH + H \rightarrow H_2O$	-491.49	-489.17	-501.00	-491.96
$OH + H_2 \rightarrow H_2O + H$	-48.51	-51.93	-53.91	-59.88
$O + O \rightarrow O_2$	-445.52	-450.94	-470.55	-493.58
$O_2 + H \rightarrow HO_2$	-202.37	-216.05	-214.68	-203.44
$O_2 + H_2 \rightarrow HO_2 + H$	240.61	221.19	232.41	228.64
$HO_2 + H \rightarrow OH + OH$	-168.00	-172.63	-161.13	-154.64
$HO_2 + H_2 \rightarrow 2\ OH + H$	274.98	264.62	285.96	277.44
$HO_2 + H \rightarrow H_2O_2$	-368.39	-361.89	-367.30	-358.53
$HO_2 + H_2 \rightarrow H_2O_2 + H$	74.59	75.35	79.79	73.55
$H_2O_2 + H \rightarrow H_2O + OH$	-291.10	-299.91	-294.84	-288.07

Table 3.3: Ab initio CCSD(T) energies and DFT energies for both functionals used (PW1K, MPWB1K) in kJ mol^{-1}. The reactions shown are part of the water formation pathway in the gas phase, as shown in Figure 3.2. Overall DFT values are around 12 kJ mol^{-1} lower than the corresponding CCSD(T) values.

3.4. Results and Discussion

3.4.1. Adsorption on the surfaces

Adsorption energies are an important way of validating the functionals used here and can be compared with experimental values. It is important to validate the functionals used, as they were chosen to represent long-range interactions, including physisorption energies and transition state barriers. Table 3.4 shows experimental physisorption energies of H_2, water, CO and methanol on different surfaces. Table 3.5 compares the adsorption energies obtained in this research with the previously reported ones. Physisorption energies are typically lower than 60 kJ mol^{-1}, whereas chemisorption energies, where adsorption involves the creation of a chemical bond, are typically higher than 80 kJ mol^{-1}. Table 3.5 shows reasonable agreement between the two functionals used in this research: MPWB1K, used for the coronene calculations, and PW1K, used for the graphene calculations. This is a very important result, as it clearly suggests that the results obtained with both functionals are comparable. PW1K reproduces adsorption energies better than MPWB1K, which is surprising since the MPW exchange includes a different factor for the gradient part of the density compared to the PW functional, and MPW was optimised for this purpose. Moreover this also shows that coronene and graphene have a similar influence on the adsorbates, the investigation of which was one of the main aims of this research. Results also show that they catalyse the reactions in a similar way, as discussed later.

Table 3.5 shows some disagreement between the experimentally measured values of the adsorption energy and theoretically obtained values. DFT predicts smaller values for long-range interactions, i.e. a lower binding energy is obtained. There are several reasons for the observed disagreements. Firstly, experimentally measured values include adsorbate – adsorbate interactions, which will give a different number compared to theoretically calculated values, where only one molecule is adsorbed. For strongly polarised molecules, which may also have hydrogen bonding, the binding energy will be higher than the theoretical one. Secondly, experimental surfaces have defects (adatoms, vacancies, etc.) whereas the computed surface is perfect and shows no defects. Finally, the first DFT functionals (LDA, GGA, see Chapter 2) were unable to reproduce van der Waals interactions and were, as Zhao and Truhlar pointed out (37), focused on reproducing chemical bonds. Newer DFT methods, including the hybrid functionals used in this work, aim to better represent other forms of bonding (including dispersion interactions). However, DFT is still not capable of exactly reproducing energies, and a difference in adsorption energy of about 10 kJ mol^{-1} is to be expected (37). Therefore the major underestimation of the adsorption energy seen here is most likely due to problems with DFT and occurs because of the presence of strong hydrogen bonds between the adsorbed species. Nevertheless, there is a clear physisorption potential for all molecules and atoms, which proves very important since the dust grain surface is able to adsorb and retain species, thus improving the probability of reaction.

Table 3.4: Experimental adsorption energies for water and other relevant species, on different surfaces.

Species	**Adsorption energy / kJ mol^{-1}**	**reference**
H on H_2O	-3.74	(38)
H_2 on H_2 ice	-0.83	(38)
H_2 on H_2O/CH_3OH	-4.62	(38)
H_2O on HOPG	-39.90 – -46	(39, 40)
CO on HOPG	-11.25	(41)
CO on HOPG *(calculation)*	-12.18 – -12.82	(42)
CH_3OH on HOPG	-41.00 – -48.00	(43)

Table 3.5: Theoretical adsorption energies for the water system adsorbed on coronene and on graphene, calculated with the MPWB1K and the PW1K functional respectively. Comparison is also made with previous studies, both experimental and theoretical.

	PW1K (graphene) [this study]	**MPWB1K (coronene) [this study]**	**Other studies**
H	-0.86	3.14	-3.05 – -4.23 $^{\mathrm{HOPG}}$ (44)
^1O	-397.08	-388.89	-166.89 – -183.79 $^{\mathrm{HOPG}}$ (45)
^3O	-7.82	-5.91	---
H_2	-3.25	2.57	< -7 (46, 47); -5.31 $^{\mathrm{PAH}}$ (48); -3.78 – -5.02 $^{\mathrm{HOPG}}$ (44)
OH	-12.42	-8.46	---
H_2O	-14.06	-9.36	-12.06 – -17.85 $^{\mathrm{HOPG}}$ (44) *calculated* -39.90 – -46 $^{\mathrm{HOPG}}$ (39, 40) *experimental*

Figure 3.4 shows the adsorption geometries for water on the two surfaces; both geometries are clearly very comparable. Both hydrogen atoms point towards the surface, creating order on the surface. Figure 3.5 shows the geometries for OH on both surfaces. Again, no major differences can be seen. Water adsorbs between 2.945 Å (graphene) and 3.112 Å (coronene) from the surface. The distance to the surface from hydroxyl is between 2.830 Å (graphene) and 2.963 Å (coronene). The distances are measured from the oxygen atom, and a systematic difference can be observed showing that PW1K binds the molecules on average 0.15 Å closer to the surface. This is the main origin of the difference in adsorption energies between PW1K and MPWB1K.

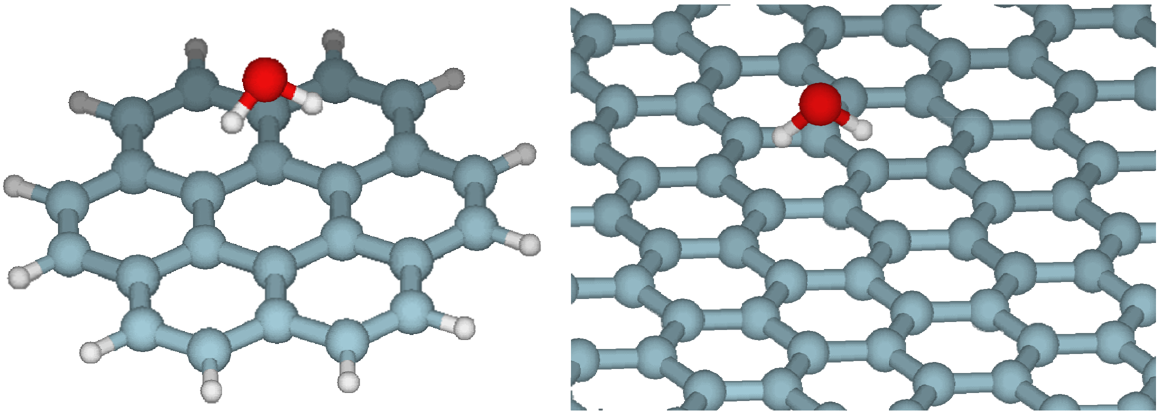

Figure 3.4: Adsorption geometries of water on the surfaces. Left: water on coronene, right: water on graphene.

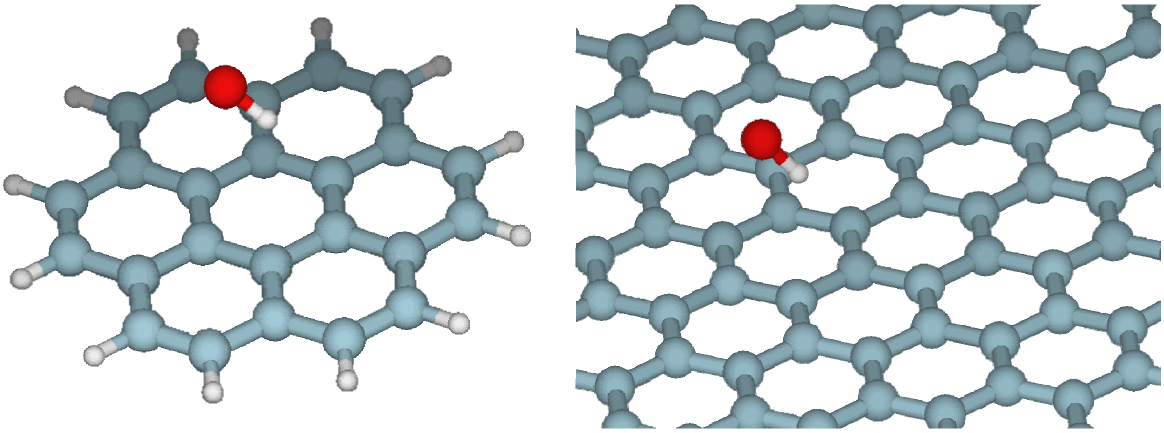

Figure 3.5: Adsorption geometries of hydroxyl on the surfaces. Left: hydroxyl on coronene, right: hydroxyl on graphene.

3.4.2. Water formation reactions

Before any reactions on a surface were investigated, activation barriers and reaction energies were determined in the gas phase. Using the gas phase values, it is then possible to discriminate against reactions with high activation barriers and also against endothermic reactions, since the catalytic effect of a purely physisorbing surface is assumed to be minimal[1]. 8 reactions important to

---

[1] The reactions which are exothermic and have a relatively low activation barrier were calculated on a surface, which gave an estimate for the reduction in activation barrier with respect to the gas phase. This was then used reversely, to decide whether it was worth calculating reactions with a relatively high gas phase activation barrier. This technique is valid as long as the used atoms and molecules are the same or similar (i.e. in this case

water formation are shown in Figure 3.2, each of which uses either H or H_2 as a hydrogen source. The results for these reactions in gas phase are shown in Table 3.6. Saddle point geometries and their energies (which, after conversion, give the barrier heights) were optimised from initial structures obtained by constrained potential energy surface scans along the reaction coordinate, or via quadratic synchronous transfer (in which case an initial guess for the transition state structure is obtained by interpolating the geometry between the starting and ending geometries). Both algorithms are subject to the researcher's 'chemical intuition', and are usually able to find the correct geometry if the starting geometry is sufficiently close to the transition structure geometry. The nature of all reactants, products and transition states was therefore assured by checking the number of imaginary frequencies (0 for stable products; 1 for transition states).

The ozone pathway (9, 17, 20) to water formation has a very large activation barrier to ozone formation, in itself an endothermic reaction. Even though the destruction of ozone by a hydrogen atom only has a negligible activation barrier, this reaction was not investigated on a surface because there is no feasible way of forming the molecule. Cuppen and Herbst (20) reported a zero activation barrier for reaction (7), in disagreement with the present study. However no explanation as to how this number was obtained was given. Ozone has not been detected in the ISM at present (see Chapter 1 and the NASA website), which is a strong indication that, since ozone is relatively stable, there is no barrierless pathway to its formation, and hence its contribution to water formation via ozone (reactions 7 and 8) is negligible. Figure 3.6 shows the singlet, triplet and quintuplet reaction energies for $^1O_3$ (on the left hand side) and $^3O_2$ + ^3O (right hand side), and indicates a minimal activation barrier of around 100 kJ mol^{-1}. Ozone is commonly produced by dissociating oxygen gas (e.g. (49, 50)), and as such the oxygen atoms are probably in an electronically excited state, which helps to overcome the barrier.

H, OH, H_2O, etc.), and as long as the used method (functional, basis set) stays the same throughout all calculations.

Table 3.6: Total gas phase reaction energies and activation barriers of reactions involved in water formation, calculated with the MPWB1K and the PW1K functionals. Energies are in kJ mol^{-1}, activation barriers are in italics below the reaction energies. All molecules and radicals involved are assumed to be in the ground state (triplet state for O_2 and O, doublet state for other radicals, singlet state for other molecules).

(*) This reaction is assumed to go via an intermediate, excited H_2O_2 molecule in which case the activation barrier equals the reaction energy, since the formation of H_2O_2 in itself is barrierless.

		MPWB1K	**PW1K**
O + H → OH	1a	-423.18	-419.81
		---	---
OH + H → H_2O	2a	-501.00	-489.17
		---	---
O_2 + H → HO_2	4a	-214.68	-216.05
		8.36	*not calculated*
HO_2 + H → H_2O_2	5a	-367.30	-361.89
		---	*not calculated*
H_2O_2 + H → H_2O + OH	6a	-294.84	-299.91
		33.40	*not calculated*
HO_2 + H → 2 OH (*)	9a	-161.13	-172.63
		-161.13(*)	*not calculated*
O + H_2 → OH + H	1b	23.91	17.43
		56.35	*not calculated*
OH + H_2 → H_2O + H	2b	-53.91	-51.93
		20.48	*22.13*
O_2 + H_2 → HO_2 + H	4b	232.41	221.19
		236.82	*not calculated*
HO_2 + H_2 → H_2O_2 + H	5b	79.79	75.35
		109.47	*not calculated*
H_2O_2 + H_2 → H_2O + OH + H	6b	152.26	137.33
		not calculated	*not calculated*
HO_2 + H_2 → 2 OH + H	9b	285.96	264.62
		not calculated	*not calculated*
O + O → O_2	3	-470.55	-450.94
		---	---
O + O_2 → O_3	7	11.19	30.42
		93.24	*not calculated*
O_3 + H → O_2 + OH	8a	-434.37	-450.23
		>340	*not calculated*
O_3 + H_2 → O_2 + OH + H	8b	12.72	-12.98
		not calculated	*not calculated*

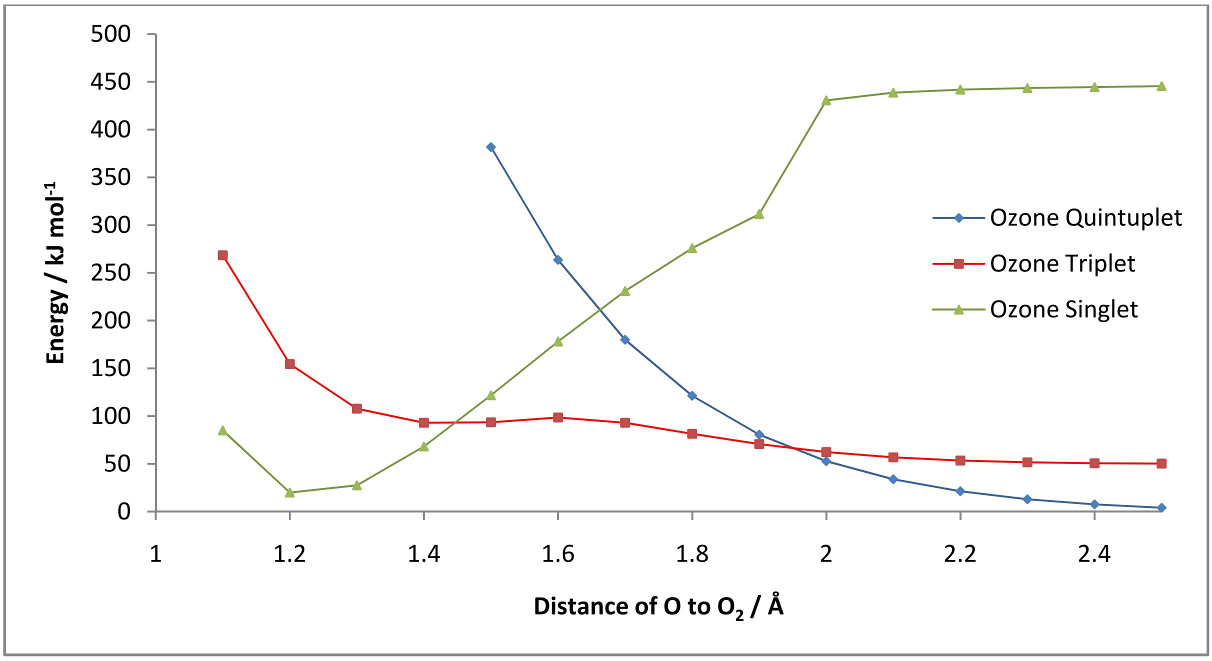

Figure 3.6: Ozone formation from O_2 + O. Ozone is the lowest point on the singlet curve (left). The energy of O_2 + O is set to zero at infinite distance (right, quintuplet line).

With only one exception, table 3.6 shows that reactions involving H_2 are endothermic. This is not surprising since a very strong H–H bond needs to be broken (437.24 kJ mol^{-1} according to PW1K, 447.09 kJ mol^{-1} according to MPWB1K) in order for these reactions to proceed. Only the formation of the H–O bond in water is exothermic enough to make the overall reaction 2b exothermic. The two DFT methods disagree on the endo- or exothermicity of reaction 8b, but since the formation of ozone is inhibited by a large activation barrier this, in essence thermoneutral, reaction will not contribute significantly and was therefore not researched on a surface.

The decision to study reactions (1a) O + H, (2a) OH + H, and (2b) OH + H_2 was based on the observed endothermicity of reactions involving H_2 bond cleavage, and the large activation barriers which will be encountered in the other reaction pathways.

3.4.3. O + H → OH, OH + H → H_2O

As was mentioned earlier, Cuppen and Herbst (1, 20) suggested that surface reactions (1a) and (2a) are the dominant route to water formation in diffuse clouds, where hydrogen mainly occurs as hydrogen atoms. Only taking into account neutral-neutral surface reactions, reactions (3), (4), (5) and (6) would be the primary ones in dense molecular clouds, since hydrogen is mainly present as H_2 in these clouds. Calculations performed here confirm that the addition of H to the radicals O or OH is barrierless. Figure 3.7 shows the reaction energy for a hydrogen atom reacting with physisorbed OH on coronene. As such, the surface's main influence on these reactions is to retain these reactants and increase the surface coverage, such that the possibility of two reactants encountering each other and reacting increases.

For this to be true, i.e. for two reactants to encounter each other on a surface and react, both of the reactants must adsorb on the surface. However the adsorption energy must not be so large that the reactants become immobilised. Therefore the ideal adsorption energy lies between 0 and 60 kJ mol^{-1}, which is called the physisorption region. The calculated adsorption energies were shown in Table 3.6, and show that oxygen is more stable in the singlet state. In this case, a triatomic ring system is formed (an epoxide) with two carbon atoms from graphene or coronene, as shown in Figure 3.8. Oxygen has thus formed two chemical bonds and is chemisorbed, and therefore immobilised on the surface. There is an activation barrier to chemisorption and an activation barrier to desorb oxygen from the surface. For this reason, chemisorbed oxygen can be considered to be removed from the water chemical network and it was subsequently excluded from further investigation.

All species in the (gas phase) ground state physisorb on the surface. Two sets of calculations were performed; one on coronene and one on graphene. The PW1K functional, which was used for graphene calculations, gives systematically lower adsorption energies than MPWB1K: species adsorb 2 to 6 kJ mol^{-1} less effectively than according to MPWB1K. From comparison with experimental results, MPWB1K is believed to be closer to the true value. PW1K is the best available functional in the Crystal06 program, but fortunately the difference from MPWB1K is relatively small and as such both graphene and coronene results can be used.

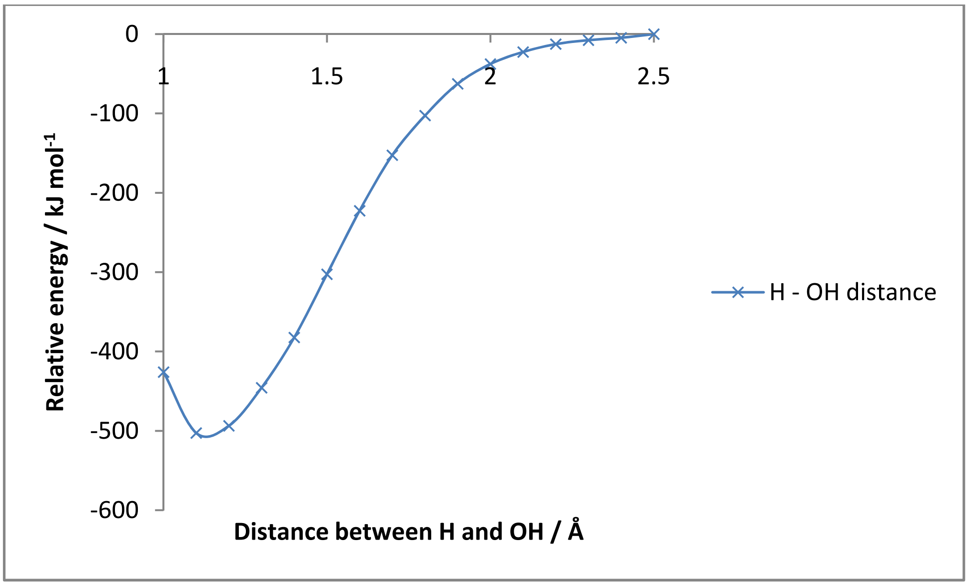

Figure 3.7: Reaction energy profile for H + OH on a coronene surface.

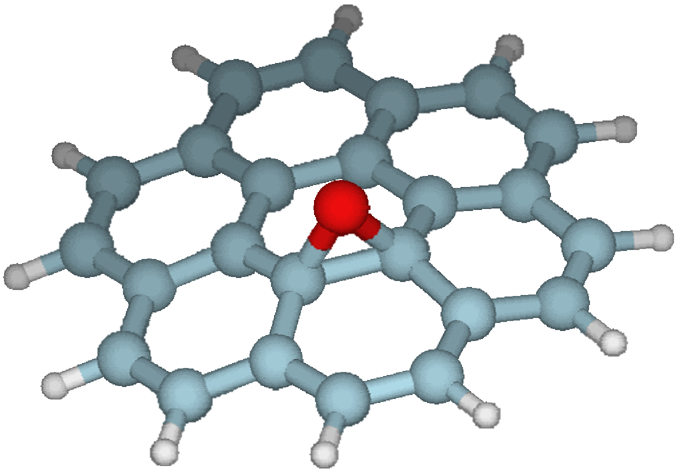

Figure 3.8: Chemisorbed oxygen on coronene, forming an epoxide ring with two coronene carbon atoms.

Adsorption energies were calculated as:

$$E_{ads} = E_{X+surf} - E_X - E_{surf}$$

Where E_{surf} is the energy of the (clean, perfect) surface, E_X is the energy of the gas phase component *X*, and E_{X+surf} is the energy of *X* adsorbed on a surface; all energies represent energies of optimised structures. The calculated adsorption energies for ^3O, OH and H_2O range from -7.82 to -

14.06 kJ mol^{-1} (MPWB1K), which was already shown to be an underestimation. Most likely the actual adsorption energies are a factor of 2 – 3 times larger. Upon formation of OH and water via reactions (1a) and (2a), a massive amount of energy is released (between 400 and 500 kJ mol^{-1}) which will at least partially be absorbed by the surface. Previous research on the formation of H_2 on a graphite surface (27, 51-59) has shown that a surface does indeed absorb a significant amount of the formation energy into phonon modes. However, even if the surface absorbs 90% of the reaction energy, this still leaves enough energy for the newly formed product to desorb. Contrary to their charged counterparts, neutral-neutral gas phase reactions under ISM conditions are very inefficient, since new molecules are formed in highly excited states and must lose some energy, otherwise they will dissociate into smaller parts. When a product is formed on the surface and desorbs, it will have to re-adsorb on a surface before reacting any further, because of the inefficiency of gas phase reactions.

Since neither hydrogenation reaction O + H nor OH + H has an activation barrier, this reaction pathway is the main water formation pathway. The other possible pathways, shown in Figure 3.2, have barriers to water formation and will inevitably contribute much less to water formation. Eley Rideal addition of hydrogen to physisorbed oxygen or hydroxyl is barrierless. The Langmuir Hinshelwood addition encounters a minor barrier: the hopping barrier for hydrogen on the surface. Calculations have shown this barrier to be less than 0.5 kJ mol^{-1}, thus comparable to RT even at temperatures around the universe's background noise of around 3 K; this barrier will therefore not hinder the reactions.

3.4.4. $OH + H_2 \rightarrow H_2O + H$

Reactions (1b) and (2b) are alternative reactions to water formation, where hydrogen is now provided by hydrogen gas. Reaction (1b) is endothermic and has a substantial activation barrier. The electron cloud of ^3O is very small, hence a purely physisorbing surface will not reduce this activation barrier enough for the reaction to proceed on the surface. However once OH is formed, which is possible via other routes (e.g. the dissociation of alcohols, and many reactions between oxygen-bearing molecules and H or H_2 (28, 29)), reaction (2b) can proceed and contribute to water formation. Table 3.7 shows the results of these calculations, for both graphene and coronene compared to the gas phase results. Two mechanisms, Langmuir Hinshelwood (LH; H_2 is physisorbed on the surface before reacting) and Eley Rideal (ER; H_2 comes from the gas phase before reacting) were investigated. In both cases OH is physisorbed on the surface.

The ER mechanism on coronene weakly catalyses H_2O formation. The activation barrier is reduced to 18.38 kJ mol^{-1}, a 10% reduction with respect to the gas phase (20.48 kJ mol^{-1}). The LH reaction on coronene increases the barrier to 23.60 kJ mol^{-1}, because in this case the H_2 – OH gas phase transition state is hindered sterically, thus a less efficient orientation on the surface occurs, leading to a small increase in activation energy. Very similar results were obtained for a graphene surface. The activation barrier for the ER reaction is slightly lower than the gas phase activation barrier, where a slightly increased barrier is found for the LH mechanism. This result is very important since, despite the different surface (though they are similar, i.e. both reactions happen near aromatic carbon six-membered rings), and despite the different functionals that were used, a very similar result is obtained. This implies that research performed on either surface – as long as there are no edge effects as described in Chapter 2 – is equally valid. Figure 3.9 shows the transition state of OH + H_2 on a coronene surface. In this transition state, the H_2 bond is already stretched from 0.7499 Å to 0.8303 Å, and the OH bond distance has decreased slightly from 0.9642 to 0.9622 Å.

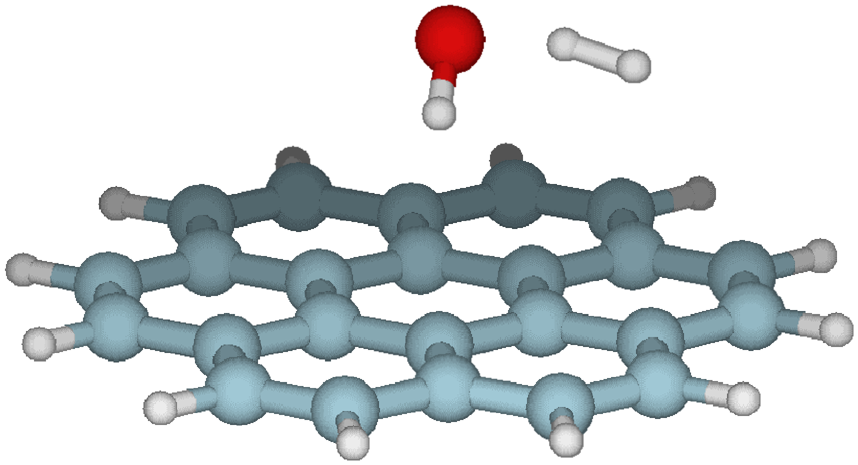

Figure 3.9: Langmuir Hinshelwood transition state for the reaction of H_2 + OH on coronene.

Table 3.7: Calculated reaction energies and activation barriers of the reaction $OH + H_2 \rightarrow H_2O + H$. Calculations were performed with the MPWB1K (coronene) and the PW1K (graphene) functionals. Energies are in kJ mol^{-1}, activation barriers are in italics below the reaction energies. Both Langmuir Hinshelwood (LH) and Eley Rideal (ER) mechanisms were considered. ΔE denotes the reaction energy, and $\Delta E^{\neq}$ denotes the activation energy.

		MPWB1K – coronene			PW1K – graphene		
		Gas phase	ER	LH	Gas phase	ER	LH
$OH + H_2 \rightarrow H_2O + H$	ΔE	-53.91	-55.56	-53.17	-51.93	-52.83	-52.26
	$\Delta E^{\neq}$	*20.48*	*18.38*	*23.60*	*25.13*	*22.43*	*27.19*

3.5. Astrochemical implications

From accurate frequency calculations of both the transition state and the reactant state on the coronene surface, the rate constant and the pre-exponential factor for a reaction can be determined, as discussed in Chapter 2. The reaction rate constant and pre-exponential factor can then be incorporated into chemical models of astrophysical environments, which models the chemical evolution of the universe. Since the optimised structures need to be converged extremely well (they must be exactly in the local minimum of the PES), results obtained using Crystal06 would take a very long time, particularly since Crystal06 calculates the first and second order derivatives numerically rather than analytically. Therefore only the coronene results are discussed.

The rate constant and the pre-exponential factor of the reaction OH + H_2 → H_2O + H were calculated as a function of the temperature. In Chapter 2, it was explained that pre-exponential factors can be calculated based on vibrational frequencies (equation 2.28).

$$A = \frac{hN_A}{2\pi m} \frac{\exp\left(\sum_i \ln\left(1 - \exp\frac{-v_i}{T}\right)^{-1}\right)^{\neq}}{\exp\left(\sum_i \ln\left(1 - \exp\frac{-v_i}{T}\right)^{-1}\right)^{R}} \tag{3.1}$$

In this equation, m is the mass of the reactant, T is the temperature, h is Planck's constant, and N_A is Avogadro's constant. The v_i are the vibrational and rotational frequencies, obtained from the frequency calculation. Equation (3.1) shows that the (Langmuir Hinshelwood) pre-exponential factor A is dependent on the temperature T. This dependency is shown in Table 3.8 and Figure 3.10, Figure 3.11 shows the dependency for the ER mechanism. The (Arrhenius) rate constant of a reaction is now simply given by equation (3.2):

$$k = A\exp\left(-\frac{\Delta E^{\neq}}{RT}\right) \tag{3.2}$$

The rate constant k is hence also dependent on the temperature, this dependency is also shown in Table 3.8 and Figures 3.10 and 3.11. From equations (3.1) and (3.2), one can see that the temperature dependence of the rate constant is not a simple expression. However, for very low temperatures, the rate constant drops to zero asymptotically (since the exponential part of equation (3.2) becomes infinitely small). For high temperatures, it may be assumed that the pre-exponential factor will equal the rate constant, since the exponential factor will equal 1.

Figure 3.10: Temperature dependency of the Langmuir Hinshelwood pre-exponential factor (A) and reaction rate constant (k) for the reaction OH + H_2 ⟶ H_2O + H on a coronene surface.

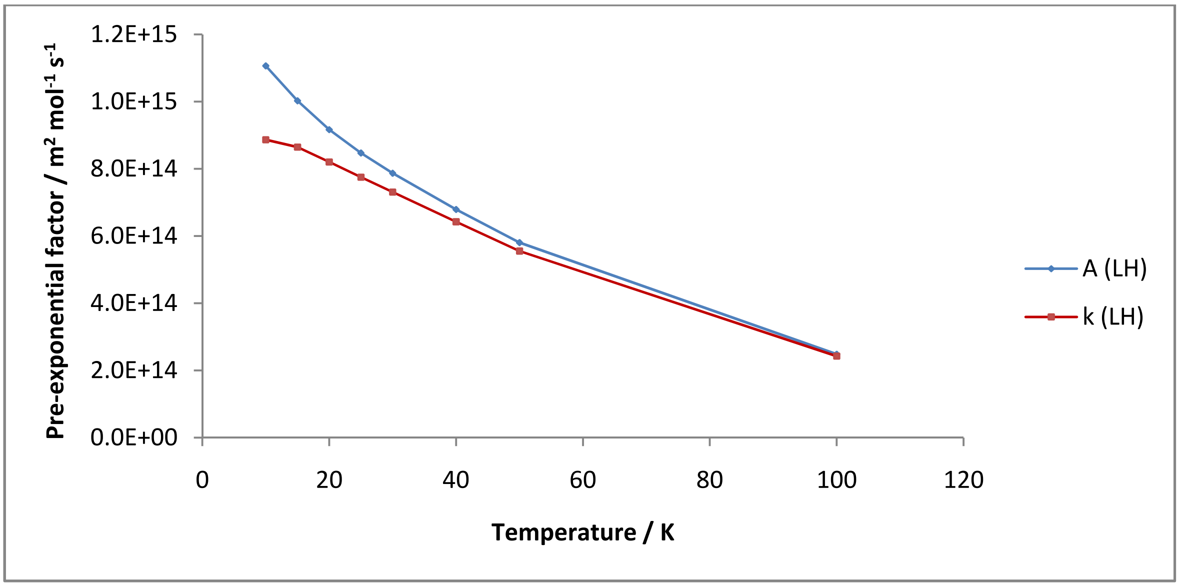

Figure 3.11: Temperature dependency of the Eley Rideal pre-exponential factor (A) and reaction rate constant (k) for the reaction OH + H_2 ⟶ H_2O + H on a coronene surface.

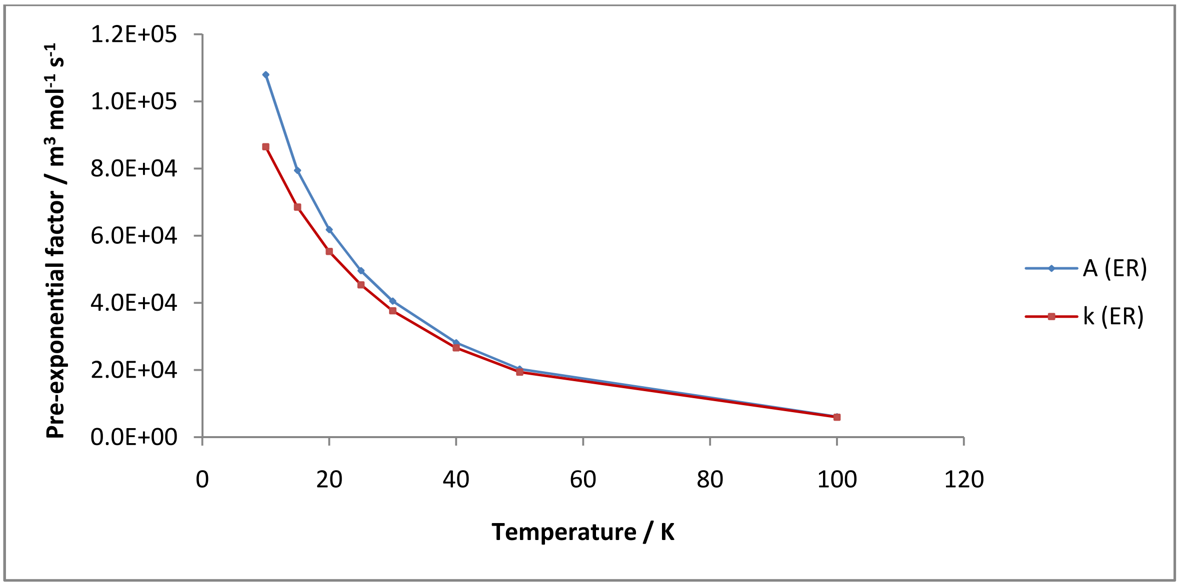

Table 3.8: Reaction rate constants and pre-exponential factors for both Eley Rideal and Langmuir Hinshelwood type OH + $H_2 \rightarrow H_2O + H$ reactions on a coronene surface.

Temperature / K	**A (LH) / m^2 mol^{-1} s^{-1}**	**k (LH) / m^2 mol^{-1} s^{-1}**	**A (ER) / m^3 mol^{-1} s^{-1}**	**k (ER) / m^3 mol^{-1} s^{-1}**
10	1.107×10^{15}	8.866×10^{14}	1.080×10^{5}	1.066×10^{4}
15	1.002×10^{15}	8.648×10^{14}	7.944×10^{4}	7.880×10^{4}
20	9.166×10^{14}	8.205×10^{14}	6.181×10^{4}	6.143×10^{4}
25	8.471×10^{14}	7.753×10^{14}	4.959×10^{4}	1.965×10^{4}
30	7.869×10^{14}	7.309×10^{14}	4.054×10^{4}	4.037×10^{4}
40	6.791×10^{14}	6.425×10^{14}	2.812×10^{4}	2.803×10^{4}
50	5.805×10^{14}	5.553×10^{14}	2.028×10^{4}	1.277×10^{4}
100	2.481×10^{14}	2.426×10^{14}	6.098×10^{3}	1.528×10^{4}

At every temperature, there is a certain rate of reaction, dependent on the coverage and (in the case of ER) the H_2 gas pressure. The reaction rate competes with the rate of desorption, which, since the coverage is nearly zero, is assumed to be a first-order process for every adsorbed species. Therefore, it is possible to calculate the ratio as a function of the temperature, of molecules which will react to form water before desorption occurs.

$$\frac{r_{rxn}}{r_{des}} = \frac{A_{rxn}}{A_{des}} \exp\left(\frac{\Delta E_{des} - \Delta E_{rxn}^{\neq}}{RT}\right)\left\{H_2\right\} \tag{3.3}$$

In equation (3.3), r_{rxn} and r_{des} are the rate of reaction and the rate of desorption respectively. A_{rxn} and A_{des} are the respective pre-exponential factors, ΔE_{des} is the desorption energy and $\Delta E_{rxn}^{\neq}$ is the activation barrier. T is the temperature, and finally $\left\{H_2\right\}$ is the H_2 coverage in the case of LH reactions, and the partial H_2 pressure in the case of ER reactions. Using an H_2 partial pressure of 1.38 x 10^{-17} (for 10 K) to 1.38 x 10^{-16} bar (for 100 K) and an experimental A_{des} of 2 x 10^{14} s^{-1} (60), the ratio of the rates shown in eq. (3.3) does not exceed 10^{-24} for an ER reaction. However, the ratio for the LH type reaction goes up to 10^{-3} at extremely low temperatures, showing that this reaction can indeed proceed and is favoured over the ER type reaction. This is a significant result: even though the activation barrier is barely reduced, still a small amount of OH reacts to water via this mechanism. Figure 3.12 shows ratio (3.3) as a function of the temperature for the LH reaction (plotted on the left axis) and the ER reaction (plotted on the right axis). This graph suggests that, for temperatures between 10 and 20 K, around 1 OHO molecule in 10,000 will react with H_2 to form water, whereas desorption occurs for the other molecules. This number is dimensionless, i.e. it is a comparison between reaction and desorption, however depending on the OH density and the OH flux (OH is still produced via other mechanisms), the contribution via this reaction pathway is significant.

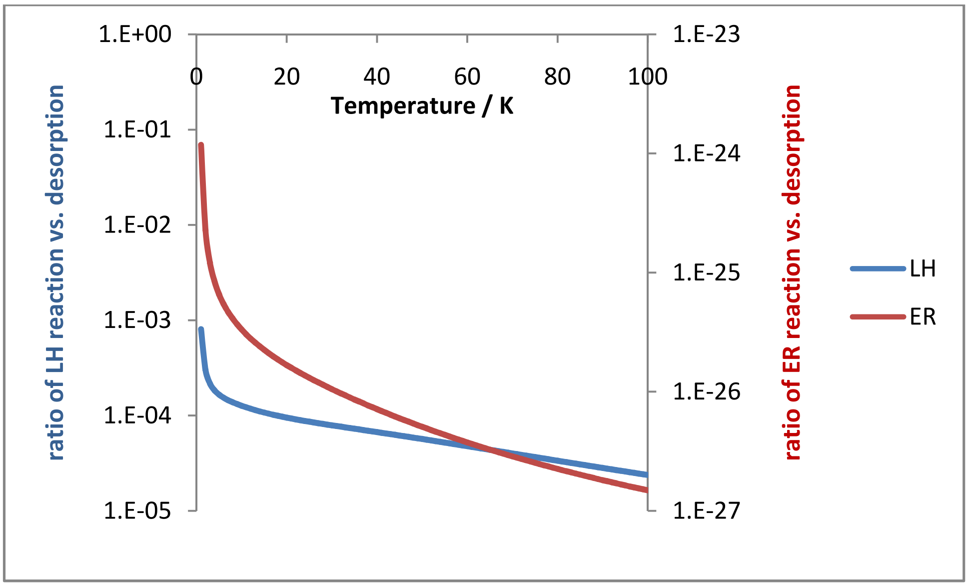

Figure 3.12: the ratio of reaction vs. desorption for LH (left hand axis) and ER (right hand axis) mechanisms, as a function of the temperature.

3.6. Conclusions

In this research, it has been shown that the reactions O + H ⟶ OH and OH + H ⟶ H_2O are both barrierless, in the gas phase as well as on a surface. The molecules water and OH, and the atoms O and H adsorb on the surface therefore the surface will increase the probability of an encounter and the success of these encounters. This route is thought to be the major formation route for water formation, since at 10 – 20 K H atoms are mobile on the surface and experience no hopping barrier, thus allowing for fast movement over the surface.

It has also been shown that a graphene and a coronene surface can both catalyse the water formation reaction OH + H_2 → H_2O + H, albeit very weakly. No strong catalytic effect is expected since both surfaces only physisorb the reactants, and neither have a dipole moment. Even though only pure van der Waals forces are responsible for the observed physisorption, a (small) reduction of the gas phase activation barrier is observed, and it is believed, based on previous results from our group (12), that polar or charged surfaces may have a stronger catalytic influence on these reactions. The influence of a defective surface will be different, given that adatoms or vacancies may chemisorb species and immobilise them. However, once the chemically active defects are removed and only physisorption is possible, the effect will be similar to the polar surfaces and larger than a clean, perfect surface.

The reaction on a surface can proceed via two different mechanisms: Eley Rideal and Langmuir Hinshelwood. The ER mechanism is catalysed, whereas the LH mechanism is not, since the transition state of the latter experiences steric hindrance from the surface. The catalytic effect of the surface reduces the former activation barrier by approximately 10%. The LH mechanism is favoured over the ER mechanism despite the slightly larger barrier, because the probability of an encounter on the surface is many orders of magnitude larger than in the gas phase.

The calculations performed here have also shown that the differences between calculations performed on coronene and graphene are only minor. The adsorption energies are very similar, although the MPWB1K functional performs better than the PW1K functional. PW1K however is the 'best' functional available in Crystal06. The activation barriers are comparable in height, i.e. again the influence of coronene and graphene are similar. A major drawback to use graphene however is the time needed for a successful calculation to complete. This is almost entirely due to the nature of the NEB algorithm and the need to calculate a large amount of geometries. Coronene however can only be used if the molecules which are studied are small enough, such that the hydrogen atoms of coronene do not influence the reaction (unless, of c0ourse, such an influence is desired). This means that calculations in the following chapters, making use of both graphene (for methanol) and coronene (for OCS) are equally valid.

3.7. References

1. Miyauchi, N., Hidaka, H., Chigai, T., et al., *Chem. Phys. Lett.*, 2008, **456**, 27.
2. Ioppolo, S., Cuppen, H. M., Romanzin, C., et al., *Astrophys. J.*, 2008, **686**, 1474.
3. Dulieu, F., Amiaud, L., Congiu, E., et al., *arXiv:0903.3120*, 2008.
4. Dulieu, F., Amiaud, L., Fillion, J. H., et al., *Molecules in Space and Laboratory*, 2007.
5. Woon, D., *J. Chem. Phys.*, 1996, **105**, 9921.
6. Woon, D. E., *Astrophys. J.*, 2002, **569**, 541.
7. Dhendecourt, L. B., Allamandola, L. J., Baas, F., et al., *Astron Astrophys*, 1982, **109**, L12.
8. Garrod, R., Park, I. H., Caselli, P., et al., *Faraday Discuss*, 2006, **133**, 51.
9. Hiraoka, K., Miyagoshi, T., Takayama, T., et al., *Astrophys. J.*, 1998, **498**, 710.
10. Das, A., Acharyya, K., Chakrabarti, S., et al., *Astron Astrophys*, 2008, **486**, 209.
11. Stantcheva, T., Shematovich, V. I. and Herbst, E., *Astron Astrophys*, 2002, **391**, 1069.
12. Goumans, T. P. M., Catlow, C. R. A. and Brown, W. A., *J Phys Chem C*, 2008, **112**, 15419.
13. Goumans, T. P. M., Wander, A., Catlow, C. R. A., et al., *Mon. Not. R. Astron. Soc.*, 2007, **382**, 1829.
14. Woodall, J., Agundez, M., Markwick-Kemper, A. J., et al., *Astron Astrophys*, 2007, **466**, 1197.
15. Tennyson, J., *Handbook of Molecular Physics and Quantum Chemistry - Chapter 3: Molecules in Space*, 2003.
16. Tielens, A., *J. Phys. Chem.*, 1983, **87**, 4220.
17. Tielens, A., *Astron Astrophys*, 1982, **114**, 245.
18. van Dishoeck, E., *Annu Rev Astron Astr*, 1998, **36**, 317.
19. Klein, R. and Scheer, M. D., *J. Chem. Phys.*, 1959, **31**, 278.
20. Cuppen, H. M. and Herbst, E., *Astrophys. J.*, 2007, **668**, 294.
21. Mckee, C. F. and Draine, B. T., *Science*, 1991, **252**, 397.
22. Caselli, P., Stantcheva, T., Shalabiea, O., et al., *Planet Space Sci*, 2002, **50**, 1257.
23. Jelea, A., Marinelli, F., Ferro, Y., et al., *Carbon*, 2004, **42**, 3189.
24. Bergin, Edwin A., Melnick, Gary J. and Neufeld, David A., *Astrophys. J.*, 1998, **499**, 777.
25. Woon, D. E. and Herbst, E., *Astrophys. J.*, 1997, **477**, 204.
26. Cuppen, H. M., Morata, O. and Herbst, E., *Mon. Not. R. Astron. Soc.*, 2006, **367**, 1757.
27. Chang, Q., Cuppen, H. M. and Herbst, E., *Astron Astrophys*, 2005, **434**, 599.
28. Johnson, R. D., Editon edn., Sept 2006.
29. Manion, J. A., Huie, R. E., Levin, R. D., et al., *NIST Chemical Kinetics Database, NIST Standard Reference Database 17 (Web Version), Release 1.4.2, Data version 08.09*.
30. Ohishi, M., Irvine, W. M. and Kaifu, N., *Iau Symposia*, 1992, 171.
31. Gibb, E. L., Whittet, D. C. B., Schutte, W. A., et al., *Astrophys. J.*, 2000, **536**, 347.
32. Ralph, K. and Milton, D. S., *J. Chem. Phys.*, 1959, **31**, 278.
33. Goumans, T. P. M., Editon edn.
34. Werner, H.-J., Knowles, P. J., Lindh, R., et al., *MOLPRO, version 2006.1, a package of ab initio programmes*.
35. Dovesi, R., Saunders, V. R., Roetti, C., et al., ed. Torino, U. o., Torino, Editon edn., 2006.
36. Frisch, M. J., Trucks, G. W., Schlegel, H. B., et al., *Gaussian, Inc., Wallingford CT*, 2004.
37. Zhao, Y. and Truhlar, D. G., *J Phys Chem A*, 2004, **108**, 6908.
38. Sandford, S. A. and Allamandola, L. J., *Astrophys. J.*, 1993, **417**, 815.
39. Brown, W. A., Viti, S., Wolff, A. J., et al., *Faraday Discuss*, 2006, **133**, 113.

40. Ulbricht, H., Zacharia, R., Cindir, N., et al., *Carbon*, 2006, **44**, 2931.
41. Piper, J., Morrison, J. A. and Peters, C., *Mol. Phys.*, 1984, **53**, 1463.
42. Hansen, F. Y., Bruch, L. W. and Roosevelt, S. E., *Phys Rev B*, 1992, **45**, 11238.
43. Brown, W. A. and Bolina, A. S., *Mon. Not. R. Astron. Soc.*, 2007, **374**, 1006.
44. Vidali, G., *Surf Sci Rep*, 1991, **12**, 133.
45. Ferro, Y., Allouche, A., Marinelli, F., et al., *Surf. Sci.*, 2004, **559**, 158.
46. Dericbourg, J., *Surf. Sci.*, 1976, **59**, 565.
47. Matsumoto, T., *Phys Rev E*, 2008, **77**, 031611.
48. Tran, F., Weber, J., Wesolowski, T. A., et al., *J Phys Chem B*, 2002, **106**, 8689.
49. Freeman, D. E., Yoshino, K. and Parkinson, W. H., *Science*, 1990, **250**, 1432.
50. Slanger, T. G. and Gadd, G. E., *Science*, 1990, **250**, 1433.
51. Chang, Q., *Astron Astrophys*, 2006, **458**, 497.
52. Greenberg, J. M., *Surf. Sci.*, 2002, **500**, 793.
53. Islam, F., Latimer, E. R. and Price, S. D., *J. Chem. Phys.*, 2007, **127**.
54. Meijer, A., Farebrother, A. J. and Clary, D. C., *J Phys Chem A*, 2002, **106**, 8996.
55. Meijer, A., Farebrother, A. J., Clary, D. C., et al., *J Phys Chem A*, 2001, **105**, 2173.
56. Meijer, A. J. H. M., Fisher, A. J. and Clary, D. C., *J Phys Chem A*, 2003, **107**, 10862.
57. Morisset, S., Aguillon, F., Sizun, M., et al., *Phys Chem Chem Phys*, 2003, **5**, 506.
58. Morisset, S., Aguillon, F., Sizun, M., et al., *J. Chem. Phys.*, 2005, **122**.
59. Rutigliano, M., Cacciatore, M. and Billing, G. D., *Chem. Phys. Lett.*, 2001, **340**, 13.
60. Goumans, T. P. M., Uppal, M. A. and Brown, W. A., *Mon. Not. R. Astron. Soc.*, 2008, **384**, 1158.

Methanol

Chapter 4

4.1. Astronomical importance of methanol

4.1.1. Importance of methanol, formaldehyde and CO

Methanol (CH_3OH), formaldehyde (CH_2O) and CO have been detected in high abundances in the interstellar medium (ISM), both in the gas phase and in ices (1). Even though some molecules, including CO, can be formed in the gas phase (2), the abundance of certain other molecules, including methanol and formaldehyde, cannot always be explained considering only formation reactions which happen in the gas phase (2-5). The ISM environment of dark clouds, described in Chapter 1, is very cold (the temperature is lower than 20 K) and therefore any reaction should have a very low or absent activation barrier in order for it to proceed under these conditions. Since the gas phase activation barriers of methanol and formaldehyde formation are large (as will be shown numerically below), the detected abundances are sometimes too high for them to be formed exclusively in the gas phase (5-7) and astrochemical models, predicting radical and molecule formation, must be adapted in order to predict the correct amount of these molecules. Dust grains, also described in Chapter 1, can catalyse the formation of molecules by lowering the gas phase activation barriers. The necessity of including dust grains in these models arises from the fact that even the best gas phase models predict an amount of methanol which is three orders of magnitude lower than the observed value (5).

It has been suggested that, in addition to understanding the formation of species on dust grains, one also needs to investigate the adsorption and desorption processes on the grains, because, according to some models, all molecules (including methanol, formaldehyde and CO) should have accreted on dust grains after a relatively short period of time (2). This understanding of adsorption and desorption processes would include understanding the sticking probability, a number which is commonly set to 1, i.e. when an atom or molecule hits a grain, the probability for it to stick to the grain is unity. This approximation is valid only when the surface coverage is very low (i.e. for a molecule hitting a grain, there will be an adsorption site available), and when there is no activation barrier to adsorption (i.e. a molecule will not 'bounce off' the surface).

The research described here focuses on carbonaceous surfaces, more specifically a graphene surface, as dust grain models, to catalyse the formation reactions of CO to methanol. There are many other possible surfaces, including siliceous or icy surfaces, all of which are derived from what is known of the structure of dust grains, described in Chapter 1.

Since methanol is the simplest alcohol, and formaldehyde the simplest carbonyl compound, it is very important to understand the formation of both of these molecules, in the gas phase as well as in solution or on a surface. Once the formation pathways of these smaller molecules are understood, the formation of similar larger molecules is likely to occur via analogous pathways and hence can be understood more easily. Moreover, both methanol and formaldehyde may play important roles themselves in forming more complex molecules; for example they can be one of the reactants in forming a larger molecule[a] or they can be involved in catalysing the formation of larger molecules.

Since hydrogen is the most abundant atom and hydrogen gas (H_2) is the most abundant molecule present in the universe, hydrogenation reactions are the most important reactions observed in the ISM. Therefore, the currently accepted formation pathway of formaldehyde in the ISM, both in the gas phase and on a surface, includes hydrogenation of CO in two steps. Methanol in turn is formed from formaldehyde, requiring another two steps to hydrogenate it (8-11). CO, the starting molecule, is readily available both as a gas phase molecule, or as an ice component (2).

Here, both the gas phase and surface catalysed formation of methanol were studied computationally, starting from CO and using graphene as a model dust grain surface. CO was sequentially hydrogenated with hydrogen atoms, following two likely routes, to methanol.

---

[a] In fact, the formation of methanol from CO – as is explained further in this chapter – proceeds via formaldehyde. This is an example of the above statement where, once formaldehyde can be formed, methanol can be formed from it.

4.1.2. Abundances and possible reactions

Methanol can be formed from CO reacting with hydrogen (this can be hydrogen atoms, H_2, or some other form of hydrogen). The proposed sequence of reactions for methanol formation from CO is shown in Figure 4.1, where every arrow signifies the addition of hydrogen. The abundances and column densities of relevant species in dark molecular clouds are shown in Table 4.1, including CO, CH_2O and CH_3OH. The abundances of these species are relatively high, in comparison with other very abundant species like water and CO_2, which suggests that there is at least one pathway which can easily lead to the formation of CH_2O and CH_3OH.

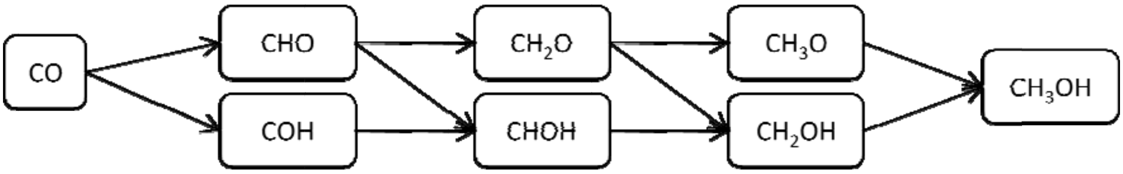

Figure 4.1: Possible hydrogenation pathways of CO to formaldehyde and methanol, both in the gas phase and on a surface.

Table 4.1: Observed abundances for species in the methanol formation pathway, in dark molecular clouds. CO_2 and H_2O have been included for comparison purposes. CD = Column Density, Ab = Abundance relative to H_2.

Molecule	**CD in W33A** (7), $/10^{-17}$ cm^2	**Average CD** (7), $/10^{-17}$ cm^2	**Ab in TMC-1** (6)	**Ab in ices** (12)	**CD in Mon R2** (13), $/10^{-10}$ cm^2
H_2O	110	12.5 – 120	---	5×10^{-5}	---
CO	8.9	1.00 – 18.0	8×10^{-5}	$1 \times 10^{-6} – 10 \times 10^{-6}$	---
CHO	---	---	---	---	1.2 – 3.9
CH_2O	7.1	1.75 – 25.2	2×10^{-8}	2×10^{-6}	---
CH_3OH	19.5	0.50 – 36.0	$2\text{-}3 \times 10^{-9}$	4×10^{-6}	---
CO_2	14.5	0.38 – 6.60	---	8×10^{-6}	---

Certain cations, including CO^+, CHO^+ and COH^+, have also been detected in the ISM (12-14) and in fact, CHO^+ is quite often the dominant ion in dark clouds. This suggests the further possibility of a formation pathway for formaldehyde and methanol using charged intermediates. As a matter of fact, almost all reactions involving the CO^+, HCO^+ and COH^+ ions in the UMIST database are marked as barrierless, and therefore their contribution to the formation of methanol in the gas phase is likely to be significant. The column density, and the abundance, of these charged species in dark molecular clouds is much lower than the density of neutral molecules. More importantly however, as was pointed out in Chapter 3, though ion-neutral chemistry usually dominates in the gas phase, , the focus of this research is on carbonaceous, polycyclic carbon surfaces. On these surfaces, any charge present is smeared out or neutralised, such that ion-neutral reactions effectively become neutral-neutral reactions.

4.1.3. Previous work

Under the ISM conditions of low pressure and temperature, the generally accepted neutral-neutral gas phase and surface formation pathway of methanol from CO is shown in Figure 4.1 and is shown in detail in reactions (1) to (4). Reaction pathways involving ionic species, though very important in the gas phase, are only of minor importance on conducting surfaces and are hence excluded from this study.

$CO + H (H_2) \rightarrow$ $CHO (+H)$ (1a)

$COH (+H)$ (1b)

$CHO + H (H_2) \rightarrow$ $CH_2O (+H)$ (2a)

$CHOH (+H)$ (2b)

$COH + H (H_2) \rightarrow$ $CHOH (+H)$ (2c)

$CH_2O + H (H_2) \rightarrow$ $CH_3O (+H)$ (3a)

$CH_2OH (+H)$ (3b)

$CHOH + H (H_2) \rightarrow$ $CH_2OH (+H)$ (3c)

$CH_3O + H (H_2) \rightarrow$ $CH_3OH (+H)$ (4a)

$CH_2OH + H (H_2) \rightarrow$ $CH_3OH (+H)$ (4b)

There is much experimental literature available on the formation of methanol, both in the gas phase and on surfaces. Experimental investigations of the formation of methanol on model dust grain surfaces, as suggested in reactions (1) to (4), have been the subject of controversy, most importantly because two different research groups have obtained significantly different results. In both experiments, CO was deposited on a cold surface, and was fired upon with hydrogen atoms. Results showed that the formation of methanol from formaldehyde does not happen under all circumstances. However, it is probably a consequence of the different experimental conditions which have led to Hiraoka *et al.* reporting that methanol is not formed at 10 K (15), whereas Watanabe *et al.* (16) report that methanol is clearly formed at that temperature. There are two main differences distinguishing the experimental setup of the two experiments. Watanabe's group uses a hydrogen flux of two orders of magnitude larger than Hiraoka's group and blames the non-detection of methanol on this low flux. Hiraoka *et al.* however (17), assume that their way of generating the hydrogen atoms (via DC discharge) produces a purer beam of atoms, whereas the microwaves used by Watanabe *et al.* are said to produce other species, including free electrons and protons. Moreover, Hiraoka *et al.* report that, in Watanabe's research, a 4:1 ratio of H_2O:CO is used; water is said to have possible catalytic effects on formaldehyde and methanol formation.

The reverse process of the dissociation of methanol upon reaction with a hydrogen atom (i.e. $CH_3OH + H \rightarrow CH_2O + \ldots$) has a much lower rate and is therefore of minor importance. Hiraoka *et al.* (17) showed that the abstraction of the hydroxyl hydrogen atom from methanol by another hydrogen atom, $CH_3OH + H \rightarrow CH_3O + H_2$, does not happen. Hence methanol can be seen as a terminal product of the hydrogenation of CO, which is in agreement with Garrod *et al.*'s chemical network for methanol (18), giving cosmic rays as one of the only ways of destroying methanol; neutral-neutral reactions do not destroy it. Both Watanabe and Hiraoka clearly agree on the fact that the formation of CH_2O is faster than the formation of CH_3OH, which is also in agreement with preliminary results of experiments in our research group.

In the same publication, Hiraoka *et al.* (17) also showed that the addition of D to CHO is preferred over the abstraction of the hydrogen atom, thus leading to formaldehyde formation, rather than CO + H_2 formation. Contrarily, for D + H_2CO, the abstraction of a hydrogen atom is favoured over addition, meaning that the formation of the CHO radical is preferred over formation of CH_3O.

Catalysis of CO hydrogenation by water ice has also been shown by Watanabe *et al.* (19). Not only was CO hydrogenation improved, but formaldehyde formation was also shown to be autocatalytic. Finally, they reported that hydrogenation comes to an almost standstill outside of the interval between 12 and 20 K. Below this temperature, hydrogenation is suppressed on CO ice, and above 20 K the hydrogenation is very slow on water ice and halted on CO ice. It is interesting to consider, at this point, that CO is mobile below 20 K, as shown by Öberg *et al*. (20), allowing for both the Langmuir-Hinshelwood and Eley-Rideal mechanisms to happen.

Watanabe's group (16) also showed that methanol formation from formaldehyde is independent of the hydrogen atom beam temperature. Methanol formation from formaldehyde was shown to be twice as slow as formaldehyde formation from CO, both at 15 K. Again, it was shown that irradiation of CH_3OH with H atoms did not produce H_2CO.

Woon (4) has previously shown theoretically that the radical-radical additions (2) and (4) are barrierless in the gas phase, therefore a surface cannot catalyse these. However, reactions (2b) and (2c), CHOH formation, were shown to have an activation barrier over 40 kJ mol^{-1} (4), which is too high to be overcome in the ISM; therefore these reactions were excluded from further research in this study. The addition of hydrogen to formaldehyde can happen in two ways, as shown in (3a) and (3b): either addition to the carbon atom forming the methoxy radical, or addition to the oxygen forming the hydroxyl methyl radical. Since both additions are exothermic (4, 17) (by approximately 100 kJ mol^{-1} in the gas phase) and both reactions have a comparable activation barrier (4), both reaction pathways were investigated. Therefore, of reactions (1) to (4), only the addition of hydrogen to the molecules CO and formaldehyde will be investigated (i.e. reactions (1a), (3a) and (3b)).

4.2. Validation and benchmarking

As mentioned before, density functional theory (DFT) is an *a posteriori* theory which needs validation, therefore the relative DFT energies of all gas-phase molecules and radicals discussed in this chapter were validated against high-level CCSD(T)/aug-cc-pVTZ calculations, using the Molpro program (21). Where a surface was involved, graphene was used as the grain model, and all DFT results were obtained using the Crystal06 code (22), with the PW1K/6-311G** level of theory. The PW1K functional, which was employed here, was a newly created functional, as already explained in Chapter 2. The good correlation between DFT and CCSD(T) results can be seen in Figure 4.2 and Table 4.2.

Table 4.2: Reaction energies for the methanol formation reactions in the gas phase. CCSD(T) and PW1K calculations are shown, and all values are in kJ mol^{-1}.

Reaction	**CCSD(T) aug-cc-pVTZ [This work]**	**PW1K 6-311G** [This work]**
$CO + H \rightarrow CHO$	-59.96	-98.89
$CO + H \rightarrow COH$	112.01	69.32
$CHO + H \rightarrow CH_2O$	-380.94	-388.25
$CHO + H \rightarrow CHOH$	-55.50	-88.21
$COH + H \rightarrow CHOH$	-227.48	-256.43
$CH_2O + H \rightarrow CH_3O$	-100.25	-141.37
$CH_2O + H \rightarrow CH_2OH$	-129.77	-164.53
$CHOH + H \rightarrow CH_2OH$	-455.21	-464.39
$CH_3O + H \rightarrow CH_3OH$	-447.31	-439.58
$CH_2OH + H \rightarrow CH_3OH$	-417.61	-416.60

Both the figure and the table show the gas phase reaction energies calculated with both CCSD(T) and PW1K calculations, for all reactions involved in methanol formation in the gas phase *via* addition of a hydrogen atom in each step. Fitting a straight line by means of the least squares method shows that, with a goodness of fit value of $R^2 = 0.9985$, on average, DFT results are 42 kJ mol^{-1} lower in energy than the CCSD(T) results. It is very likely that these lower reaction energies, though they may seem slightly problematic, will be similar when gas phase values are compared to surface catalysed values. Moreover CCSD(T), even though very high level calculations, still does not give the exact values and a comparison with experimental energies is more appropriate. A more in depth discussion of these results and comparison to previously reported experimental and theoretical results will follow later.

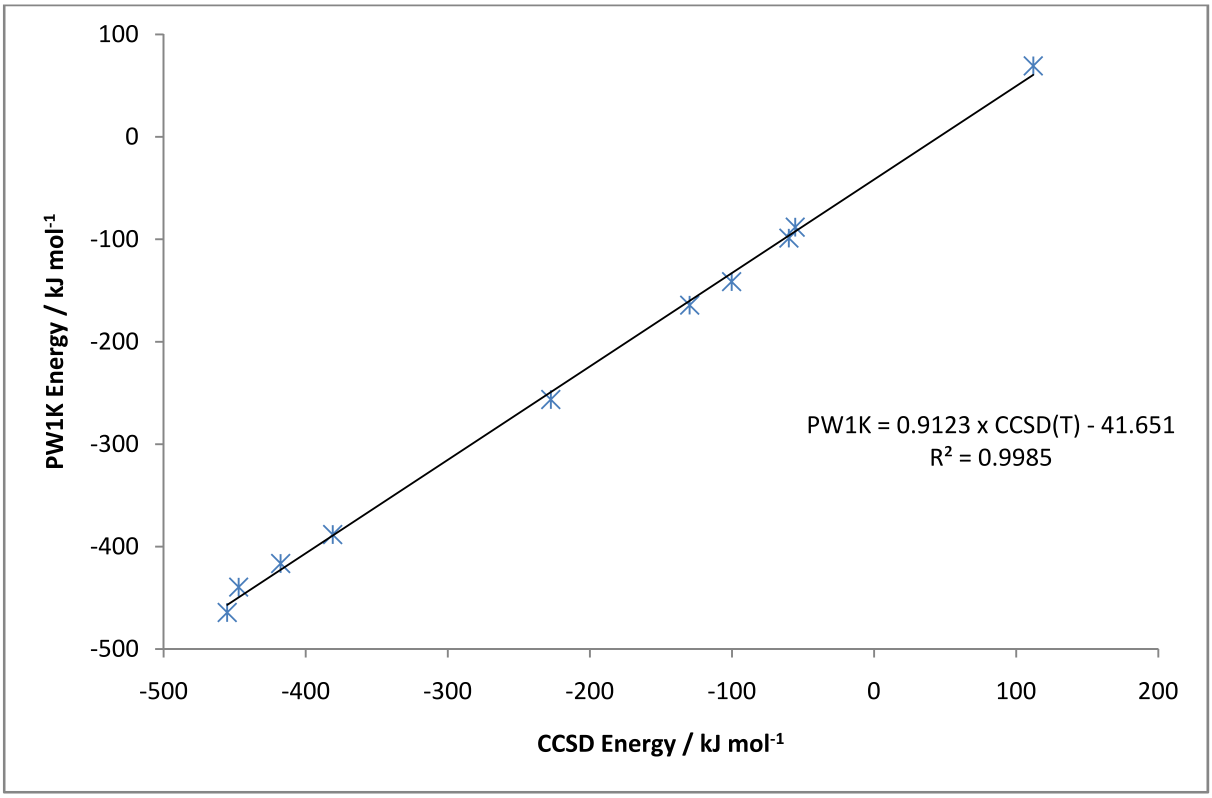

Figure 4.2: PW1K vs. CCSD(T) reaction energies for the methanol formation reactions, showing agreement between both methods.

Adsorption energies

The proposed sequence of reactions is the hydrogenation of CO via formaldehyde to methanol on a graphite surface. In the first step, CO adsorbs on the surface. At every consecutive step, either a hydrogen atom adsorbs on the graphite surface, or the species already adsorbed on the surface reacts with a hydrogen atom. Here, distinction is made between the Eley Rideal mechanism (hydrogen reacts from the gas phase) and the Langmuir Hinshelwood mechanism (hydrogen first adsorbs on the surface, after which it reacts whilst remaining physisorbed). These processes are shown in Figure 4.3. Before investigating activation barriers and catalysis by the surface, the adsorption energies of the relevant species are analysed computationally, and compared to literature values where available, in Tables 4.3 and 4.4.

Table 4.3: Experimental adsorption energies for CO, methanol, and relevant species, on different surfaces.

Species	**Adsorption energy / kJ mol^{-1}**	**reference**
H on H_2O	-3.74	(23)
H_2 on H_2	-0.83	(23)
H_2 on H_2O/CH_3OH	-4.62	(23)
H_2O on HOPG	-39.90	(24)
CO on H_2O	-14.47	(23)
CO on H_2O	-9.80	(25)
CO on CO	-7.11	(26)
CO on CO	-7.98	(23)
CO on meteorite	-13.50	(25)
CO on HOPG	-11.25	(27)
CO on HOPG *(calculation)*	-12.18 – -12.82	(28)
CH_3OH on CH_3OH	-35.21	(23)
CH_3OH on HOPG *(monolayer)*	-48.00	(29)
CH_3OH on HOPG *(multilayer)*	-41.00	(29)

Table 4.4: Adsorption energies for the methanol system adsorbed on graphene, calculated with the PW1K functional in this study and compared to previously reported results.

	PW1K / kJ mol^{-1} [this study]	**Other studies / kJ mol^{-1}**
CO	-18.54	-11.3 – -20.4 (27, 28, 30, 31)
CHO	-37.55	
CH_2O	-38.72	
CH_3O	-42.14	
CH_2OH	-60.66	
CH_3OH	-52.35	-41.0 – -48.00 (29, 30)

Figure 4.3. Reaction pathway to form methanol via formaldehyde from CO. (1a) to (1f) (top) shows the Eley Rideal mechanism. First CO adsorbs on the graphite surface, after which hydrogen in the gas phase reacts with CO. Once formaldehyde is formed, two possible reaction pathways are shown. (2a) to (2j) (bottom) shows the Langmuir Hinshelwood mechanism. CO adsorbs on the graphite surface. Physisorbed hydrogen (physisorption shown explicitly) then successively hydrogenates CO. Again, from formaldehyde on, two possible reaction pathways are shown.

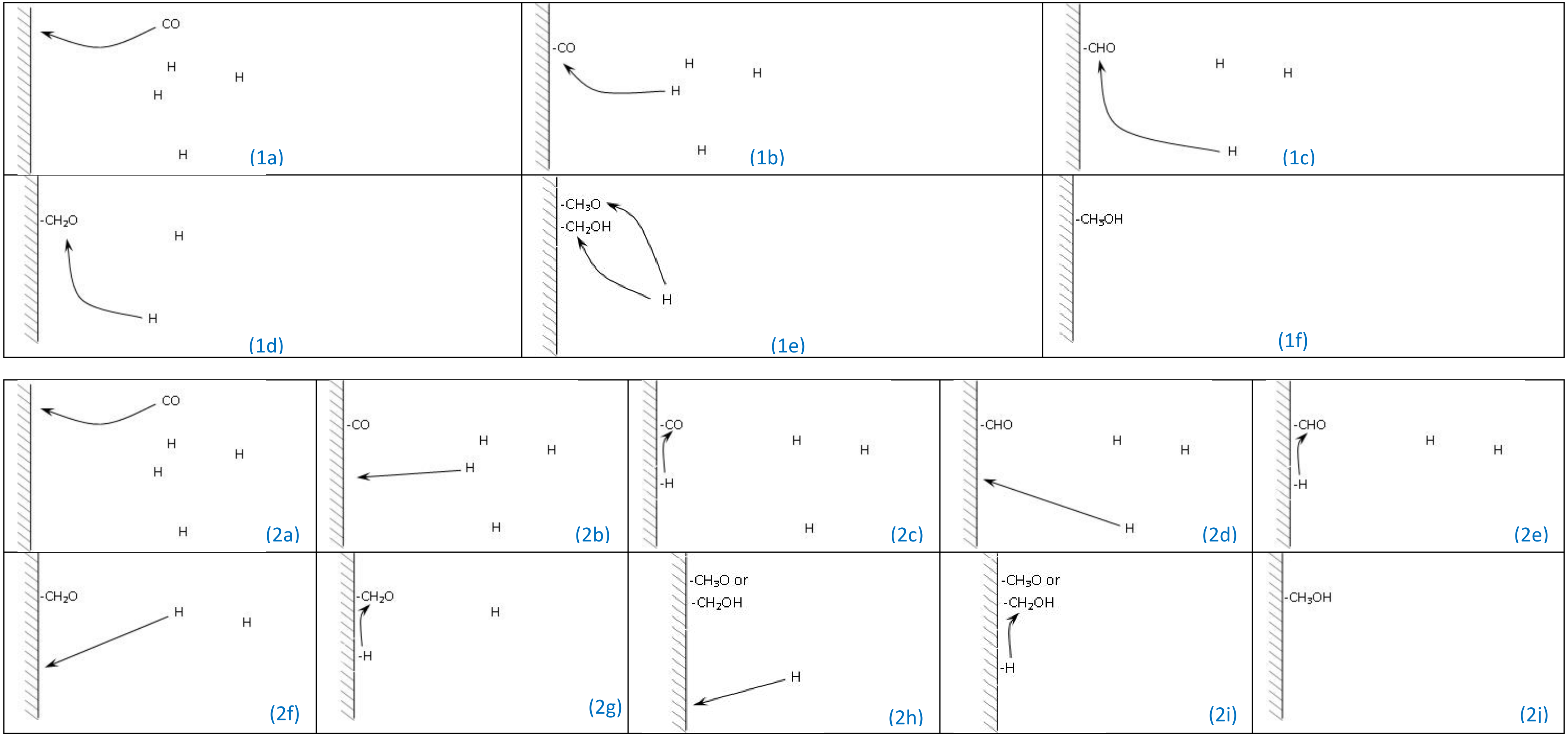

As shown in Table 4.4, the calculated adsorption energies are very close to previously reported energies, both experimental (27-30, 32) and theoretical (31), as seen in Table 4.3. However, the adsorption energies from this study are slightly higher than the ones previously reported. This could be due to several different factors, including computational factors (basis set superposition error, the use of the functional itself), and experimental errors (experimentally, many molecules are studied together, whereas computationally only one molecule adsorbs or desorbs; a real surface has defects as opposed to the computationally studied surface which is 'perfect', which will modify the adsorption energy, etc).

This is clearly supported by the fact that both Brown *et al.* (29) and Ulbricht *et al.* (30) show significantly different values for the monolayer and the multilayer desorption of methanol on HOPG, with the monolayer adsorbing more strongly than consequent layers. The good agreement between the computational results from this study and previous experimental and theoretical results validates the use of the PW1K functional.

4.3. Results and Discussion

4.3.1. Potential formation reactions of methanol from CO

As already discussed, the formation of methanol from CO is thought to occur via a stepwise addition of hydrogen. Both hydrogen molecules and hydrogen atoms can participate in these reactions. For a hydrogen molecule, it is extremely unlikely that both atoms would add simultaneously in one reaction step. More likely is that the hydrogen-hydrogen bond breaks, during which one hydrogen atom reacts to form the next product in the pathway to methanol formation. The full reaction pathway was pictorially represented in Figure 4.1, where every arrow represents the addition of one hydrogen atom, either from H or H_2.

Reactions which have H_2 as a reactant are all endothermic since a strong H—H bond is broken, whereas in general the newly formed bond is weaker. These results were confirmed in this research and are shown in Table 4.5. The only exception to this 'rule of thumb' is reaction (4a), which is in essence a thermoneutral reaction. The energy released by stabilising the CH_3O radical by forming methanol, is approximately equal to breaking the hydrogen–hydrogen bond; however the activation barrier which needs to be overcome for this reaction is far too high for it to proceed. For this reason, reactions (1) to (4) will from now on always be assumed to involve hydrogenation with hydrogen atoms rather than H_2 molecules, unless otherwise specified.

The hydrogenation of CO to formaldehyde proceeds exclusively via the CHO radical. The formation of the COH radical (1b) via CO + H or CO + H_2 is highly endothermic, as was shown computationally (4, 17). In addition, the gas phase activation barrier of CO + H → COH is much higher (in this study, a value of 243.24 kJ mol^{-1} was calculated) than the activation barrier of CO + H → CHO. Therefore it is reasonable to assume COH formation will not happen in the ISM, and that both reactions (1b) and (2c) can therefore be excluded from any further research. Figure 4.4 shows the possible reactions from CO to methanol, including the reverse reactions, via hydrogenation with H atoms.

Table 4.5: Gas phase reaction enthalpies for reactions involved in methanol formation, involving H_2 / kJ mol^{-1}.

	CCSD(T) [this study]	**PW1K [this study]**
$CO + H_2 \rightarrow CHO + H$	+368.68	+338.37
$CO + H_2 \rightarrow COH + H$	+540.70	+506.66
$CHO + H_2 \rightarrow CH_2O + H$	+67.80	+49.00
$CHO + H_2 \rightarrow CHOH + H$	+282.97	+268.93
$COH + H_2 \rightarrow CHOH + H$	+110.96	+100.64
$CH_2O + H_2 \rightarrow CH_3O + H$	+342.10	+295.34
$CH_2O + H_2 \rightarrow CH_2OH + H$	+308.67	+273.21
$CHOH + H_2 \rightarrow CH_2OH + H$	+75.26	+53.28
$CH_3O + H_2 \rightarrow CH_3OH + H$	+0.87	-1.54
$CH_2OH + H_2 \rightarrow CH_3OH + H$	+34.30	+20.58

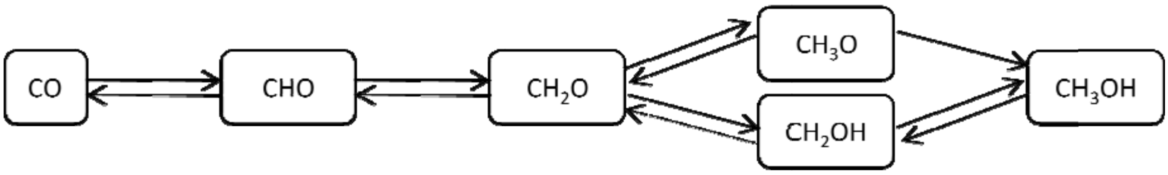

Figure 4.4: Uncharged hydrogenation pathway of CO to formaldehyde and methanol, both in the gas phase and on a surface.

4.3.2. Reactions

According to the present model, four consecutive hydrogenation reactions of CO lead to methanol; two of these reactions need to be catalysed at 10 – 20 K. Table 4.6 shows the calculated gas phase formation enthalpies for reactions involving H, whereas Table 4.5 showed similar reactions involving H_2. Although H_2 is very abundant in dark molecular clouds, reactions involving H_2 as a reactant are endothermic and therefore unlikely to happen in the ISM. However this does imply that the reverse reactions are exothermic, therefore the possibility exists that radicals like CHO, COH, CH_2OH and CH_3O could react backwards with a hydrogen atom (i.e. to the left with respect to Figure 4.4). This may be one possible mechanism for the destruction of methanol and formaldehyde, and could be an explanation for why the abundances of CO, formaldehyde and methanol are similar as shown before (Table 4.1).

In the suggested reaction pathway in Figure 4.4, two different types of addition reaction can be distinguished: addition of H to a radical, and addition of H to a molecule which does not have unpaired electrons. Some of the radical-radical additions are barrierless as shown before (4) and this has been verified in the current study. These include reactions (2a), (2c), (3c), (4a) and (4b). The other reactions shown in Figures 4.2 and 4.4 have activation barriers. Addition of a hydrogen atom to a molecule usually leads to a weaker bond within this molecule, and possibly a rearrangement of atoms relative to each other. Both of these effects, which are nearly absent in the above mentioned barrierless radical-radical reactions, are the physical reason for an activation barrier. Gas phase activation barriers have been calculated along with their adsorbed counterparts, in order to investigate any catalytic effect.

Table 4.6: Gas phase reaction energies for the methanol formation reactions. PW1K calculations performed in the current research are shown and compared with previous theoretical and experimental results where possible. PW1K and QCISD values are gas phase results. Hiraoka's results (17) involve solid formaldehyde and methanol. All values are in kJ mol^{-1}.

Reaction	**PW1K 6-311G** [This work]**	**QCISD (aug-)cc-pVDZ (4)**	***Experimental* (17) and references therein**
CO + H → CHO	-98.89	-69.2	-67.2
CO + H → COH	69.32		
CHO + H → CH_2O	-388.25		-371.0
CHO + H → CHOH	-88.21		
COH + H → CHOH	-256.43		
CH_2O + H → CH_3O	-141.37	-112.4	-94.0
CH_2O + H → CH_2OH	-164.53		-135.0
CHOH + H → CH_2OH	-464.39		
CH_3O + H → CH_3OH	-439.58		-435.0
CH_2OH + H → CH_3OH	-416.60		-393.0

CO + H → CHO

The first step in forming methanol is the addition of a hydrogen atom to CO, forming the formyl radical, with a gas phase activation barrier of 8.55 kJ mol^{-1} shown in Table 4.7. The activation barrier of CHO formation on a graphene surface following the Eley Rideal mechanism is 6.44 kJ mol^{-1}; a 25% reduction with respect to the gas phase. The Langmuir Hinshelwood activation barrier is 23% larger than the gas phase activation barrier. This is probably because hydrogen is forced to stay on the surface which leads to less freedom. The optimiser algorithm allows for every intermediate state to reach the optimal structure, only restricted by the boundary conditions that the structure remains between the previous and the next geometries of the same molecule. This means that the simulation of going from reactants to products allows for every small step to be optimised. Because this does not only minimise the energy (and the energy difference) but also the forces acting on every atom, this system is only representative for infinitely slow moving atoms. Once the atoms and molecules would move at higher velocities, it is much more appropriate to use molecular dynamics (MD) simulations, but this was beyond the scope of this project. MD could possibly find a reaction pathway with a lower transition state energy, but one where the “transition state” is not as the transition state definition, i.e. it is not a minimum of the energy in all but one coordinates, and a maximum in the remaining coordinate.

The adsorption energy of CHO is approximately 20 kJ mol^{-1} larger than the adsorption energy of CO, however the energy gain occurs after the H—C bond is formed, and CHO has rotated on the surface to have the hydrogen atom pointing downwards (see Figure 4.5). This means that CHO, upon formation on a graphene surface, needs a certain amount of time to rotate into the lowest energy position. The fact that CHO is stabilised more than CO on a graphene surface is also found in the distance to the surface: the distance from the surface to the carbon atom of CO (which is the closest to the surface) is 3.40 Å, for the HCO radical this distance is 3.17 Å. Figure 4.5 shows the reaction pathway (initial, transition and final geometries) for the ER and the LH mechanisms.

Previous studies examined the catalytic effect of neutral surfaces on CHO formation. Woon used water ice as the catalytic surface (4), and Goumans *et al.* used hydroxylated silica (33). In neither study was the gas phase activation barrier reduced significantly on the surface. These observations show that the very strong C—O bond in CO is only slightly affected by physisorption. Graphene, which provides low-energy empty orbitals (the graphene π^*-orbitals are only an infinitesimal energy higher than the bonding π^*-orbitals), can stabilise the intermediate (transition state) and final radicals, which leads to a decrease in activation energy.

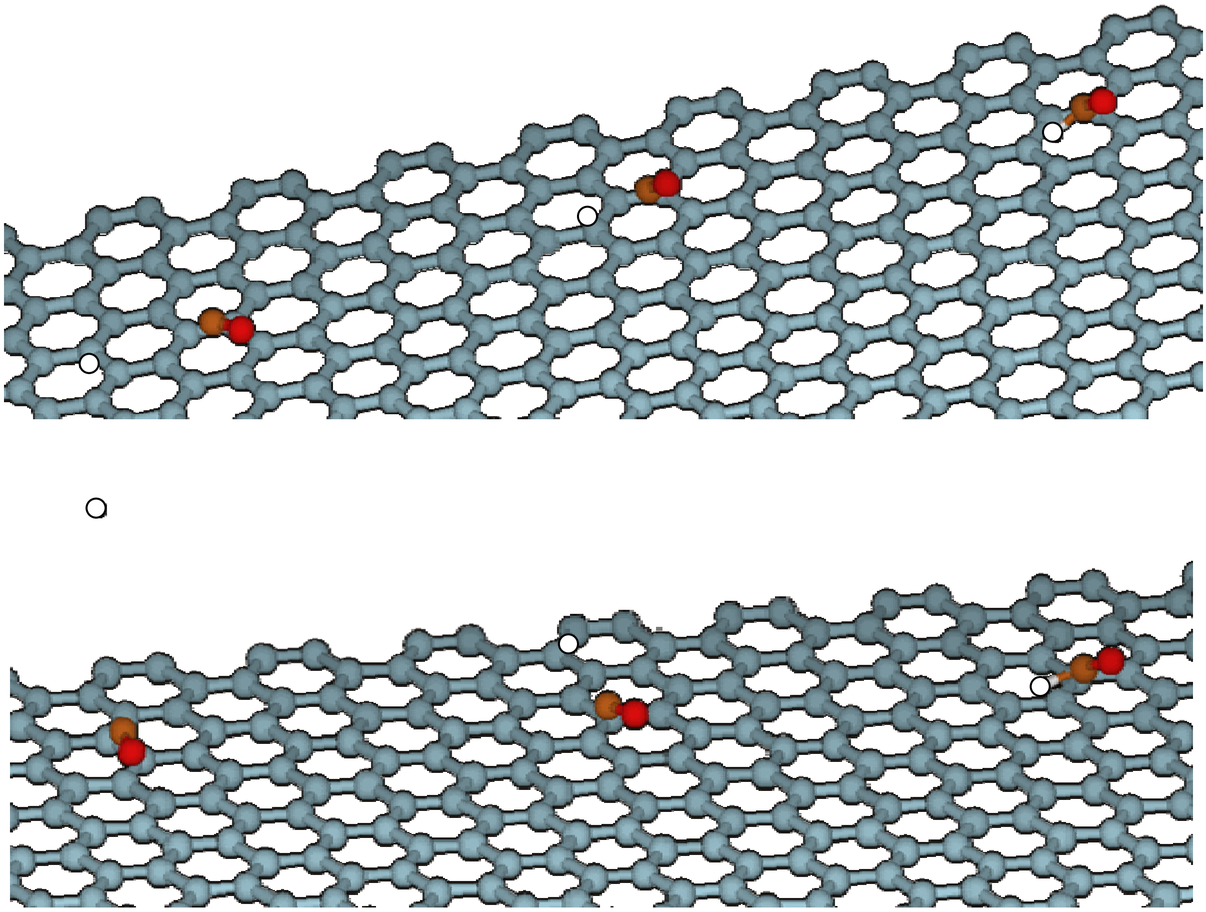

Figure 4.5: Reaction of H + CO_{ads} to give CHO_{ads}. Top: Langmuir Hinshelwood mechanism; bottom: Eley Rideal mechanism. Shown from left to right are the initial state, the transition state, and the final state geometries. Graphene is grey, carbon is brown, oxygen is red and hydrogen is white. For clarity, the graphene surface is shown terminated; the calculations were performed on 2D periodic surfaces.

A further improvement of the catalysis may be reached either when CO binds more strongly to the surface (comparable with organometallic bonding, where the backbonding destabilises the CO bond, or via radical interaction from a defected surface), or when a charged surface is involved. Another study by Goumans *et al.* researched the influence of a charged surface on different reactions of astrochemical importance (34). The general conclusion of the influence of the charged surface on the reactions is a lowering in activation barrier, and a more in depth discussion and comparison with these findings can be found at the end of this section.

Table 4.7: Comparison of calculated reaction energies and activation barriers (in italics) between gas phase and graphene. Energies are in kJ mol^{-1}.

Reaction	**Gas phase [This work]**	**Graphene [This work]**
$CO + H \rightarrow CHO$	-98.89	-117.62
	8.55	*10.48 (LH)*
		6.44 (ER)
$CO + H \rightarrow COH$	69.32	not calculated
	243.24	*not calculated*
$CHO + H \rightarrow CH_2O$	-388.25	-389.70

$CHO + H \rightarrow CHOH$	-88.21	not calculated
	202.65	*not calculated*
$COH + H \rightarrow CHOH$	-256.43	not calculated
	---	*not calculated*
$CH_2O + H \rightarrow CH_3O$	-141.37	-145.34
	12.29	*14.59 (LH)*
		14.48 (ER)
$CH_2O + H \rightarrow CH_2OH$	-164.53	-163.31
	41.81	*43.14 (LH)*
		25.72 (ER)
$CHOH + H \rightarrow CH_2OH$	-464.39	not calculated
	---	*not calculated*
$CH_3O + H \rightarrow CH_3OH$	-439.58	-447.46

$CH_2OH + H \rightarrow CH_3OH$	-416.60	-429.50

$CH_2O + H \rightarrow CH_3O$

The second activated step required for methanol formation is the addition of a hydrogen atom to formaldehyde. This can lead to two different products: CH_3O, the gas phase formation of which is activated by 12.29 kJ mol^{-1}, or CH_2OH, activated by 41.81 kJ mol^{-1}. On a graphene surface, the former is not catalysed as the ER activation barrier of 14.48 kJ mol^{-1} is of a similar height (see Table 4.7); the LH activation barrier is even slightly higher. Moreover, quite different from the formation of CHO, the addition of the hydrogen atom in this case does not lead to a large increase in adsorption energy. The explanation for this is that, since formaldehyde already has two hydrogen atoms, the third hydrogen atom adsorbs side on and will hence point upwards, away from the graphene surface, thus not contributing to the physisorption, as shown in Figure 4.6.

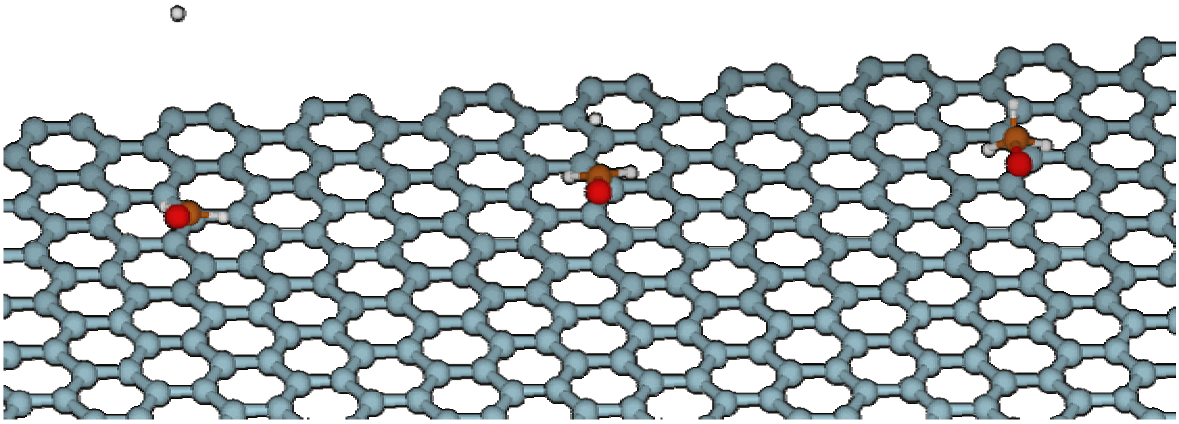

Figure 4.6: Surface reaction of $CH_2O + H \rightarrow CH_3O$. From left to right: the initial state geometry (formaldehyde plus a distant hydrogen atom), the transition state geometry, and the final state geometries (the methoxy radical adsorbed sideways on the graphene surface. The surface is shown terminated for clarity; the calculations were performed on 2D periodic surfaces. Also for clarity, the graphene carbon atoms are grey, the formaldehyde / methoxy carbon atom is brown. Oxygen is red and hydrogen is white.

Woon (4) has shown that the formation of CH_3O is catalysed by water ice, with the activation barrier being 27% lower than the gas phase activation barrier. However, no catalysis was found for this reaction in the present research. The most likely explanation is that the large dipole moment of water (1.85 Debye) catalyses the reaction with formaldehyde, which has an even larger dipole moment (2.33 Debye) (35). This also explains why there is no stronger catalysis of CO + H by water ice, compared to graphene catalysis. The dipole moment of CO is only 0.112 Debye and therefore the influence of a dipole moment is only minimal.

$CH_2O + H \rightarrow CH_2OH$

Hydrogen can alternatively react with formaldehyde to form the hydroxyl methyl radical, CH_2OH. This addition has a gas phase activation barrier of 41.81 kJ mol^{-1}, a barrier which is strongly reduced to 25.72 kJ mol^{-1} on a graphene surface with the ER mechanism; a reduction of almost 40%. Even though this barrier is still relatively high, it is in the neighbourhood of the CH_3O formation activation barrier, and therefore the contribution of this channel to methanol formation is important. Again, no reduction was observed using the LH mechanism, instead the barrier increased to 43.14 kJ mol^{-1}. Figure 4.7 shows the relative energies of CH_2O reacting with H, both in the gas phase and via the ER mechanism on a surface. The energy of CH_2O (in the gas phase or on a surface), and a hydrogen atom at infinity (i.e. far from the formaldehyde molecule) is set to zero.

Figure 4.8 shows gas phase reaction geometries at the initial, transition state and final points, and Figure 4.9 shows the same points for the surface catalysed reaction. From closely observing the reaction pathways as shown in these two figures, one can determine that two different mechanisms are followed in the two different situations. The reason for these two different mechanisms can be found in the orbitals of formaldehyde, and the stabilisation / destabilisation on the graphene surface.

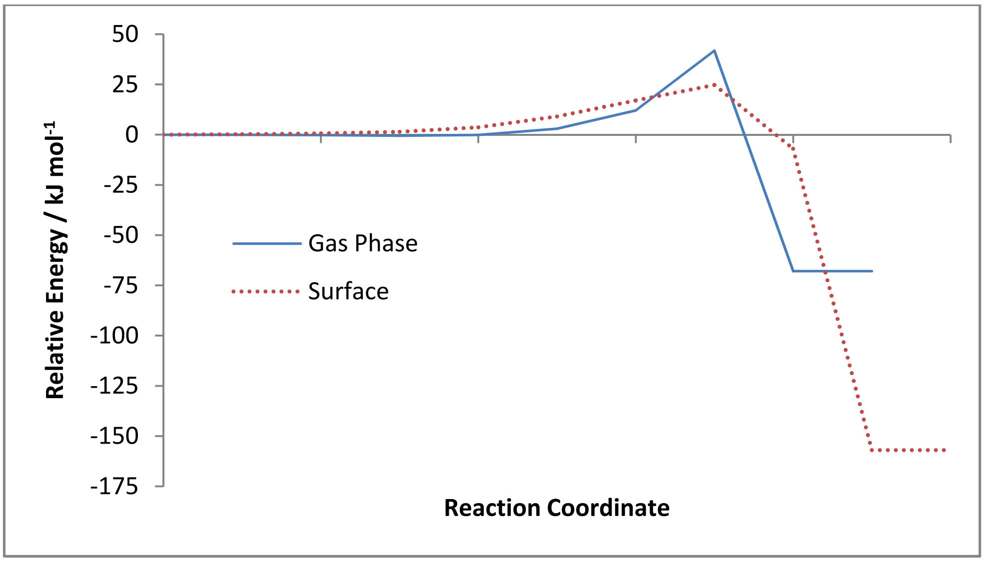

Figure 4.7: Relative energies (in kJ mol^{-1}) of formaldehyde reacting with a hydrogen atom to give the hydroxyl methyl radical. The full line shows the NEB reaction energies for the gas phase reaction; the dotted line is the surface catalysed NEB pathway. Figures 4.8 and 4.9 show the geometries corresponding to the initial, transition state and final energies.

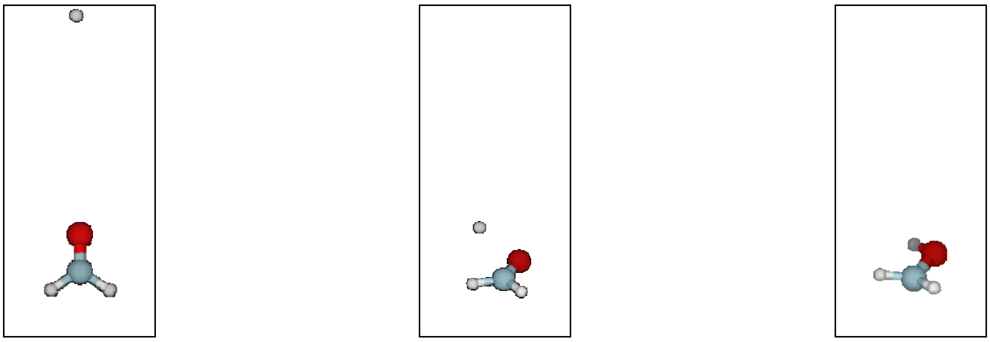

Figure 4.8: Gas phase geometries of the reaction CH_2O + H → CH_2OH. Shown from left to right: the initial geometry, the transition state geometry, and the final geometry. Carbon is grey, oxygen is red, hydrogen is white.

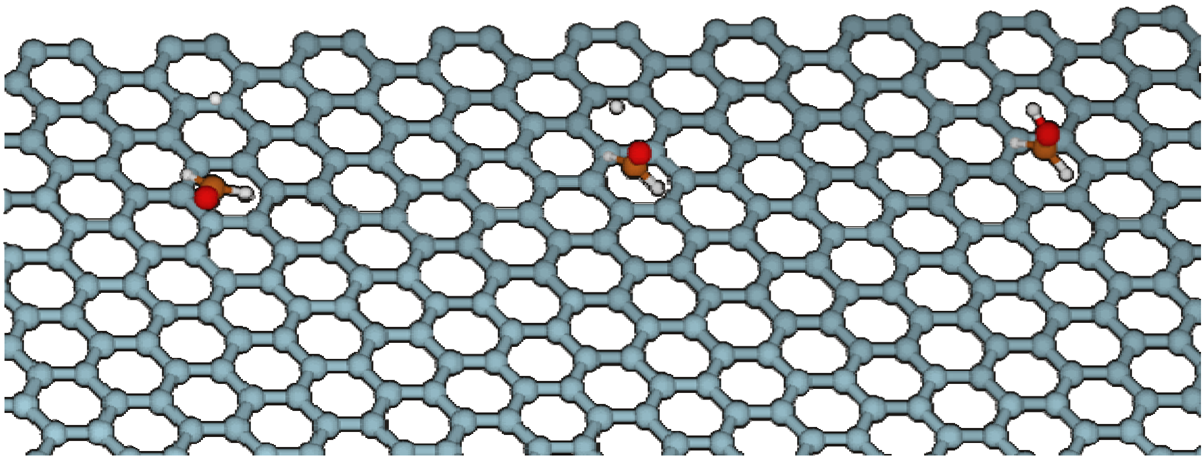

Figure 4.9: Surface catalysed formation of CH_2OH. The geometries shown are, from left to right: the initial geometry, the transition state geometry, and the final geometry. For clarity carbon is grey when it belongs to the graphene sheet, brown when it is part of the reactant. Oxygen is red, hydrogen is white.

In the following discussion, the molecular axis (the axis which connects the carbon and oxygen atoms) is labeled z; the molecule is in the yz plane, and hence the axis perpendicular to the plane of symmetry is the x axis. The hydrogen atom is expected to attack formaldehyde via the lowest unoccupied molecular orbital (LUMO), as this would require the least energy. In formaldehyde, the LUMO is a π^*-orbital, formed from the C and O p_x orbitals. Thus when an additional electron is added to this molecule (for example from the hydrogen atom), it is likely that in the first instance the hydrogen orbital overlaps with this virtual orbital. Calculations performed on formaldehyde show that the π^*-orbital is slightly larger on the carbon atom. Since this is a virtual orbital, there are no electrons occupying it, but electrons would reside more on the carbon atom should they occupy it.

Hence the gas phase activation barrier leading to CH_3O formation is lower than the activation barrier for CH_2OH formation: the hydrogen radical is more attracted and stabilised by the carbon-end of the π^*-orbital than the oxygen-end. The formaldehyde gas phase structure, π and π^*-orbitals are shown in Figure 4.10.

Structure	π-orbital	π^*-orbital
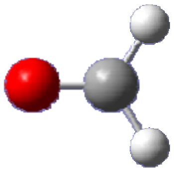	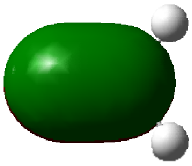	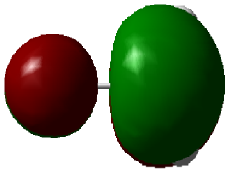
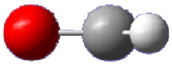	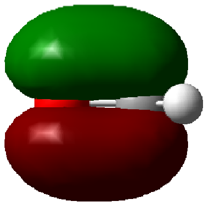	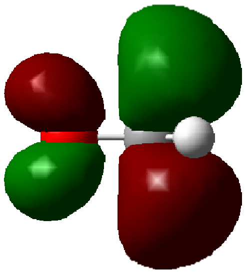

Figure 4.10: π and π^*-orbitals of formaldehyde (in the gas phase).

Graphene is a zero band gap semiconductor: there is a point of zero electron density which coincides with the Fermi-energy (the requirement for a band gap), but directly above and below this energy are bands which allow for electron density. On the surface, the formaldehyde π-orbital is stabilised by the proximity of empty graphene π^*-orbitals. Conversely, the formaldehyde π^*-orbital is destabilised. For this reason, attacking the formaldehyde π^*-orbital, when physisorbed on the fsurface, is less favourable for hydrogen than it was in the gas phase.

The formaldehyde oxygen atom has sp hybridisation in the gas phase; i.e. the atomic p_y orbital (in the plane of the molecule, perpendicular to the CO bond) retains most of its character in the formaldehyde molecule. On the surface, the oxygen hybridisation looks more like sp^2, which leads to a small increase in the C-O bonding distance (1.187 Å in the gas phase, 1.189 Å on the surface). The oxygen sp^2 orbitals can now delocalise their electrons on the graphene π^*-orbitals (similar to the formaldehyde π electrons), which lowers the energy (and is part of the source of the adsorption energy), but also leads to a partial vacancy in these orbitals. Since the oxygen sp^2 orbitals are lower in energy than the formaldehyde π-orbitals, and now have a partial vacancy, it is much more favourable for the hydrogen atom to attack the formaldehyde molecule via these orbitals, which is also seen in the transition state.

In the methanol formation pathway, reactions (3a) and (3b) have the higher activation barriers (12.29 and 41.81 kJ mol^{-1} respectively), hence this catalytic effect means an increase in the formation rate of methanol from CO by a factor of almost 2, compared to uncatalysed methanol formation. The fact that reaction (3a) is not catalysed by a graphene surface, and (3b) is catalysed, implies that the oxygen atom is more easily activated than the carbon atom. Since formaldehyde physisorbs on graphene with the hydrogen atoms pointing towards the graphene surface (with an angle of approximately 45°), the formaldehyde π-orbital is more localised on the carbon atom when the molecule is physisorbed. This results in an overlap with the graphene orbitals, and makes the oxygen side of the orbital more accessible for an incoming hydrogen atom.

Comparison with silica catalysis

Goumans *et al.* have studied the formation of methanol catalysed by a silica surface (33, 36). Dust grains, as mentioned in Chapter 1 and the beginning of this chapter, are most likely built up from an either siliceous or carbonaceous core, thus the results obtained in Goumans *et al.*'s research are very relevant to the present research. An uncharged, completely hydrogenated silicate surface was found to catalyse reactions (1a), $CO + H \rightarrow CHO$ and (3b), $CH_2O + H \rightarrow CH_2O$. Reaction (3a), $CH_2O + H \rightarrow CH_3O$, remains uncatalysed. The dust grains are likely to be negatively charged, and consequently the influence of a negatively charged surface was also studied in Goumans *et al.*'s studies. The activation barriers are reported to be lowered by small amounts, 6.4 kJ mol^{-1} for (1a), and 3.3 kJ mol^{-1} for (3a). This result is very important, as on a graphene surface the activation barrier of reaction (1a) is only reduced by 2.11 kJ mol^{-1} and the activation barrier of reaction (3a) is not reduced. On hydroxylated silica, neither activation barrier is reduced with respect to the gas phase. Therefore we may conclude that a mixture of polarised surfaces (like water ice) and aromatic surfaces (like graphene) can catalyse the methanol formation reactions; in addition, charged surfaces can also catalyse all reactions. The most logical explanation for the catalysis shown here is the weakening of the double bonds, which is more pronounced for very polar or (negatively) charged surfaces, as is indeed shown by another study of Goumans *et al.* (34). The study included completely apolar molecules like C_2H_2 and C_2H_4, hence not only the polarity of the catalysed molecule, but also the charge and/or polarity of surface are vital in catalysis.

4.4. Conclusions

The reactions of CO, CHO, CH_2O, CH_3O and CH_2OH with a hydrogen atom were shown to be exothermic, both in the gas phase and on a surface, with reaction energies ranging from around -100 kJ mol^{-1} to -400 kJ mol^{-1}. Three radical–radical additions (addition of H to CHO, CH_3O and CH_2OH) were shown not to have an activation barrier. For the remaining three reactions in the methanol formation pathway, it has been shown that pure physisorption, as provided by the graphene surface, significantly changes two activation barriers: following the Eley Rideal mechanism, the formation barriers of CHO and of CH_2OH are reduced by 25 % and 40 % respectively, with respect to the gas phase. No catalysis was observed for the other activated step, i.e. the formation barrier of CH_3O on the surface remained similar to the one observed in the gas phase. The Langmuir Hinshelwood mechanism was shown to be unfavourable, as the activation barriers increase slightly compared to the gas phase.

Catalysis for the formation of methanol from CO was seen in previous research (3, 4), where water was the catalyst. In the first step of this computational research, the water molecules surrounded the carbon atom of the CO molecule and the CHO radical. However, once formaldehyde was formed, the oxygen atom was found to be surrounded by the water molecules. It is possible that hydrogen bonding between the water molecules and the oxygen atom is more effective than that between the water molecules and the carbon atom, which is the case for formaldehyde. If this were the case with carbon monoxide, both hydrogen additions (CO + H and CH_2O + H) would be catalysed by water ice. The author remarked that in the performed research, trends rather than absolute barrier heights were shown. This leaves the possibility for water to catalyse the first reaction more effectively, were the oxygen atom hydrogen bonded. Hydrogen bonding does not only polarise the molecule, but also reduces the triple (CO) or double (CH_2O) bond, effectively reducing the activation barrier. Charged surfaces, as seen in studies by Goumans *et al*. (34), do catalyse the hydrogenation of unsaturated molecules, including the hydrogenation of CO and CH_2O. Since charges may be present in the ISM, their catalytic effect is clearly important in methanol formation.

It was observed in this research that graphene has a high affinity for the hydrogen atoms in hydrogen-bearing molecules. Adsorbates having hydrogen atoms in their structures physisorb to the surface with the hydrogen atoms pointing downwards (at an angle between 45 and 90°), leading to a high adsorption energy on the surface. This adsorption energy leads to an increase in the amount of accreted material which in turn leads to a higher encounter probability, and therefore a higher reaction rate than in the gas phase. Moreover, the preferred adsorption orientation is a kinetic form of catalysis which can increase the reaction rate. In the case of methanol formation via Eley Rideal for example, the activated reactions (3a) and (3b) will proceed faster since the probability of formaldehyde being oriented correctly on the surface is much higher, such that an encounter with a gas phase hydrogen atom is more probable to successfully lead to either CH_3O or CH_2OH.

The graphene surface was shown to be catalytic in four senses. Firstly, two out of the three reactions have their gas phase barriers reduced by almost 25% and 40% for Eley Rideal reactions.

Secondly, all species are shown to adsorb on the surface, which implies an increase in encounter probability. The adsorption energies are sufficiently low to allow for mobile species. Thirdly, the adsorption energies are high enough for energy to be transferred to the surface, which thus acts as a third body. Finally the surface orients the hydrogen bearing molecules such that a higher reaction rate is expected for Eley Rideal reactions.

4.5. References

1. Dartois, E., *Space Sci Rev*, 2005, **119**, 293.
2. Dhendecourt, L. B., Allamandola, L. J., Baas, F., et al., *Astron Astrophys*, 1982, **109**, L12.
3. Woon, D., *J. Chem. Phys.*, 1996, **105**, 9921.
4. Woon, D. E., *Astrophys. J.*, 2002, **569**, 541.
5. Garrod, R., Park, I. H., Caselli, P., et al., *Faraday Discuss*, 2006, **133**, 51.
6. Ohishi, M., Irvine, W. M. and Kaifu, N., *Iau Symposia*, 1992, 171.
7. Gibb, E. L., Whittet, D. C. B., Schutte, W. A., et al., *Astrophys. J.*, 2000, **536**, 347.
8. Williams, D. A., *Surf. Sci.*, 2002, **500**, 823.
9. Hidaka, H., *AIP Conf. Proc.*, 2006, **855**, 107.
10. Tielens, A., *Astron Astrophys*, 1983, **119**, 177.
11. Hidaka, H. and Hidaka, *Chem. Phys. Lett.*, 2008, **456**, 36.
12. van Dishoeck, E., *Annu Rev Astron Astr*, 1998, **36**, 317.
13. Rizzo, J. R., Fuente, A. and Garcia-Burillo, S., *Astrophys. J.*, 2005, **634**, 1133.
14. Herbst, E. and Woon, D. E., *Astrophys. J.*, 1996, **463**, L113.
15. Hiraoka, K., Sato, T., Sato, S., et al., *Astrophys. J.*, 2002, **577**, 265.
16. Hidaka, H., Watanabe, N., Shiraki, T., et al., *Astrophys. J.*, 2004, **614**, 1124.
17. Hiraoka, K., Wada, A., Kitagawa, H., et al., *Astrophys. J.*, 2005, **620**, 542.
18. Garrod, R. T., Wakelam, V. and Herbst, E., *Astron Astrophys*, 2007, **467**, 1103.
19. Watanabe, N., Nagaoka, A., Shiraki, T., et al., *Astrophys. J.*, 2004, **616**, 638.
20. Oberg, K. I., van Broekhuizen, F., Fraser, H. J., et al., *Astrophys J Supp*, 2005, **621**, L33.
21. Werner, H.-J., Knowles, P. J., Lindh, R., et al., *MOLPRO, version 2006.1, a package of ab initio programmes*.
22. Dovesi, R., Saunders, V. R., Roetti, C., et al., ed. Torino, U. o., Torino, Editon edn., 2006.
23. Sandford, S. A. and Allamandola, L. J., *Astrophys. J.*, 1993, **417**, 815.
24. Brown, W. A., Viti, S., Wolff, A. J., et al., *Faraday Discuss*, 2006, **133**, 113.
25. Mautner, M. N., Abdelsayed, V., El-Shall, M. S., et al., *Faraday Discuss*, 2006, **133**, 103.
26. Fuchs, G. W., Acharyya, K., Bisschop, S. E., et al., *Faraday Discuss*, 2006, **133**, 331.
27. Piper, J., Morrison, J. A. and Peters, C., *Mol. Phys.*, 1984, **53**, 1463.
28. Hansen, F. Y., Bruch, L. W. and Roosevelt, S. E., *Phys Rev B*, 1992, **45**, 11238.
29. Brown, W. A. and Bolina, A. S., *Mon. Not. R. Astron. Soc.*, 2007, **374**, 1006.
30. Ulbricht, H., Zacharia, R., Cindir, N., et al., *Carbon*, 2006, **44**, 2931.
31. Vidali, G., *Surf Sci Rep*, 1991, **12**, 133.
32. Wolff, A. J., Carlstedt, C. and Brown, W. A., *J Phys Chem C*, 2007, **111**, 5990.
33. Goumans, T. P. M., Catlow, C. R. A. and Brown, W. A., *J. Chem. Phys.*, 2008, **128**.
34. Goumans, T. P. M., Catlow, C. R. A. and Brown, W. A., *J Phys Chem C*, 2008, **112**, 15419.
35. Johnson, R. D., Editon edn., Sept 2006.
36. Goumans, T. P. M., Wander, A., Catlow, C. R. A., et al., *Mon. Not. R. Astron. Soc.*, 2007, **382**, 1829.

Carbonyl Sulphide

Chapter 5

5.1. Astronomical importance of OCS

5.1.1. Importance of OCS and astronomical abundances of its reactants

Sulphur-bearing species have been proposed as good evolutionary chemical tracers of star forming regions (1). Their abundances vary by substantial amounts during the evolution of a proto-star, therefore astronomical models are very sensitive to the amount of sulphur present and to its chemical composition. However, uncertainties regarding the form that sulphur takes, as well as its highly reactive nature (2), mean that particular attention must be paid to reactions involving sulphur. Moreover, as was mentioned in Chapter 1, the activation barrier of a gas phase reaction is often too high for the reaction to happen in dark clouds because the temperature in these clouds is lower than 20 K. The present research will focus firstly on the gas phase activation barriers for reactions containing sulphur bearing species. Secondly it will investigate the possibility of catalysis of these reactions by a carbonaceous surface.

Although the most abundant species in the interstellar medium (ISM) are hydrogen atoms and hydrogen gas, and therefore hydrogenation reactions can be considered to be the most important, the assumption that hydrogenation is the only type of reaction (and more specifically the only type of surface reaction) occurring during the formation of a star is probably an oversimplification. For sulphur this is clearly the case, as hydrogenation would lead to H_2S formation, but there has been no detection of H_2S ices in the ISM (3, 4). In contrast to H_2S, both solid (5) and gaseous (6) carbonyl sulphide, OCS, have been detected in the ISM. The detection of solid OCS raises the possibility that it may be the main reservoir of sulphur on the dust grains (7). However, it is not clear how OCS is formed in the ISM. Since H_2S is present in the gas phase and CO is abundant in ices (8), there is the possibility that H_2S photo-dissociates, so that its dissociation products can then react with physisorbed or icy CO to form OCS. Reaction can either occur with the sulphur component reacting immediately from the gas phase (Eley Rideal mechanism). Alternatively, H_2S can freeze out on an icy dust grain, but photo-dissociate and react with molecules present on the ice as well (Langmuir Hinshelwood mechanism). In this case, destruction of H_2S could be fast enough such that only a small amount of solid H_2S is present, which is under the threshold limit for detection. This could also explain the non-detection of solid H_2S.

An alternative way to form OCS is to start from H_2O, which can yield either O or OH upon photo-dissociation or by cosmic ray irradiation. These products can then react with CS to form OCS. Water ice, the second most abundant molecular species after H_2 (9), CO and CS have all been detected both in the gas phase and on dust grains (e.g. (10-13)) in the ISM. The reaction pathways, starting from the photo-dissociation products of H_2O and H_2S and leading to OCS, are summarised below and will be discussed in more detail in section 5.1.2. These reactions were studied both in the gas phase and on a coronene surface which, as described in Chapters 1 and 2, acts as a model for a carbonaceous dust grain surface. Even though the radicals mentioned in (1) – (4), formed upon photo-dissociation, can be hydrogenated back to H_2S or H_2O, competitive reactions (e.g. to OCS formation) are also possible.

$H_2S \xrightarrow{h\nu}$ HS and S radicals (+ hydrogen)

$$CO + S \rightarrow OCS \qquad (1)$$

$$CO + HS \rightarrow [\ldots] \rightarrow OCS \qquad (2)$$

$H_2O \xrightarrow{h\nu}$ OH and O radicals (+ hydrogen)

$$CS + O \rightarrow OCS \qquad (3)$$

$$CS + OH \rightarrow [\ldots] \rightarrow OCS \qquad (4)$$

Reactions (1) – (4) show possible routes to OCS formation, starting from the photo-dissociation of H_2S and H_2O. The minimum photo-dissociation energy to break the H-OH bond is 468 kJ mol^{-1}, whereas the next step (breaking the O-H bond) only requires 401 kJ mol^{-1}. Photo-dissociation of H_2S requires 370 kJ mol^{-1} of energy and forms HS. Further photo-dissociation from HS into H and S only requires 343 kJ mol^{-1}. All of these energies lie well below the Lyman-α emission line of hydrogen (984.0 kJ mol^{-1} or 121.6 nm), which is the most abundant energy quantum in the universe, and hence Lyman-α radiation can initiate these reactions. *In situ* generation of UV photons within a dark cloud is also possible (14) and encounters of these photons with molecules will happen frequently enough for photo-dissociation to occur (e.g. (15, 16)).

In dark interstellar clouds, the total density is lower than 10^7 atoms cm^{-3} and can be as low as 10^4 or even 10^3 atoms cm^{-3}. Collisions therefore happen much less frequently compared to standard conditions (1 bar, 298 K); hence the lifetime of radicals and free atoms is increased in dark clouds. Eventually, atoms, radicals and molecules can accrete onto a dust grain and during the process of physisorption they can transfer most of the kinetic energy they might have to the dust grain.

In order to assess the relative importance of each of these reactions, the reaction rates and the relative amounts of the reactants need to be determined. TMC-1 (Taurus Molecular Cloud 1) is regarded as a standard molecular cloud and, as it is relatively close to our solar system (450 light years), it is a heavily studied object. The abundances in TMC-1 (relative to the H_2 abundance) of CO, CS, OH, HS and OCS are shown in Table 5.1. The measurements were taken from reference (17) and data from a gas phase astrochemical computational model were taken from reference (18). The product of the relative OH and CS abundances is ~5 x 10^{-15}; for HS and CO this is ~1.36 x 10^{-15}. These products are of comparable magnitude, hence the relative contribution of reactions (1) – (4) to the formation of OCS will mostly depend on the activation barrier of each individual reaction.

The column density of OCS is only one order of magnitude less than the abundance of formaldehyde (H_2CO) and ammonia (NH_3) (17), which can also be seen in Table 5.1. In TMC-1, a dark molecular cloud, the OCS column density is only about two orders of magnitude less than that of OH and about 4 orders of magnitude less than that of CO (17-20).

OCS also plays an important role in other scientific areas. For example, it is reported to be the major sulphur containing molecule present in the Earth's atmosphere (21, 22). In addition Leman *et al.* (23) found that OCS can catalyse the formation of oligopeptides, starting from single amino acids;

hence it may play a key role in explaining the origin of life. OCS is a linear, colourless molecule with its first electronic excited state at 466 kJ mol^{-1} (24). OCS is isovalent with CO_2 and, as such, the differences between the formation of OCS and the formation of CO_2 (25) can tell us about the specific chemical influences of sulphur and oxygen, and the difference in reactivity of the two congeners.

Table 5.1: Measured and calculated relative abundances (R.A.) of OCS and relevant reaction products in TMC-1. The abundance is relative to that of H_2, ~4 × 10^4 molecules cm^{-3}.

Species	**Measured R. A. (17)**	**Calculated R. A. (18)**
CO	8 x 10^{-5}	---
CS	1 x 10^{-8}	3.4 x 10^{-8}
S	---	3.9 x 10^{-8}
OH	3 x 10^{-7}	---
HS	---	1.7 x 10^{-11}
H_2S	< 5 x 10^{-10}	9.9 x 10^{-11}
OCS	2 x 10^{-9}	1.3 x 10^{-9}
H_2CO	2 x 10^{-8}	---
H_2CS	3 x 10^{-9}	2.6 x 10^{-10}
NH_3	2 x 10^{-8}	---
CH_3OH	2 x 10^{-9}	---
HCOOH	< 2 x 10^{-10}	---
SO	5 x 10^{-9}	9.2 x 10^{-9}

The chemical network leading to the formation of OCS in the ISM is not known, and an understanding of the formation of OCS and the relative energies of reactants, products and transition states will therefore help us to understand the chemical evolution of the universe and to date certain regions within the ISM.

5.1.2. Potential formation reactions of OCS

In this study of the formation of OCS, four possible reaction pathways are investigated, shown in (1) – (4). Oxygen and sulphur atoms in the ground state have a triplet electronic configuration, and since OCS has a singlet configuration in the ground state, it is important to study both triplet and singlet reaction pathways for the first and third reactions, as there will be a state crossover somewhere along the reaction path. The location of the crossover dictates the point at which the excited product (^3OCS) can fall back to the ground state (^1OCS) without the input or output of additional energy. Note that because of selection rules for spin transition, unless there is spin-orbit coupling, this transition is a forbidden transition. The position of the crossover relative to the position of the transition states will determine which factors need to be investigated to assess the reaction rate and the overall activation barrier.

Upon reaction of HS + CO or OH + CS, different four-atom intermediates can be formed, which can react further to yield OCS. These intermediates each have two energetic minima, denoted *cis* and *trans*, explained later. Spontaneous dissociation of the intermediates into OCS + H is a plausible pathway. A second possibility involves another hydrogen atom reacting with the intermediate, yielding OCS + H_2. Therefore reactions (2) and (4) are in fact multi-step reactions, with different potential reaction pathways. The full reaction pathways of (1) to (4) , as shown pictorially in Figure 5.1, can hence be written as:

• $CO + S \rightarrow OCS$ $\quad CO + {}^1S \rightarrow {}^1OCS$ (1a)

$CO + {}^3S \rightarrow {}^3OCS$ (1b)

• $CO + HS \rightarrow OCS + \ldots$ $\quad CO + HS \rightarrow$ *cis*-HSCO $\rightarrow {}^1OCS + H$ (2a)

$CO + HS \rightarrow$ *trans*-HSCO $\rightarrow {}^1OCS + H$ (2b)

$CO + HS \rightarrow$ *cis*-HSCO (+ H) $\rightarrow {}^1OCS + H_2$ (2c)

$CO + HS \rightarrow$ *trans*-HSCO (+ H) $\rightarrow {}^1OCS + H_2$ (2d)

• $CS + O \rightarrow OCS$ $\quad CS + {}^1O \rightarrow {}^1OCS$ (3a)

$CS + {}^3O \rightarrow {}^3OCS$ (3b)

• $CS + OH \rightarrow OCS + \ldots$ $\quad CS + OH \rightarrow$ *cis*-HOCS $\rightarrow {}^1OCS + H$ (4a)

$CS + OH \rightarrow$ *trans*-HOCS $\rightarrow {}^1OCS + H$ (4b)

$CS + OH \rightarrow$ *cis*-HOCS (+ H) $\rightarrow {}^1OCS + H_2$ (4c)

$CS + OH \rightarrow$ *trans*-HOCS (+ H) $\rightarrow {}^1OCS + H_2$ (4d)

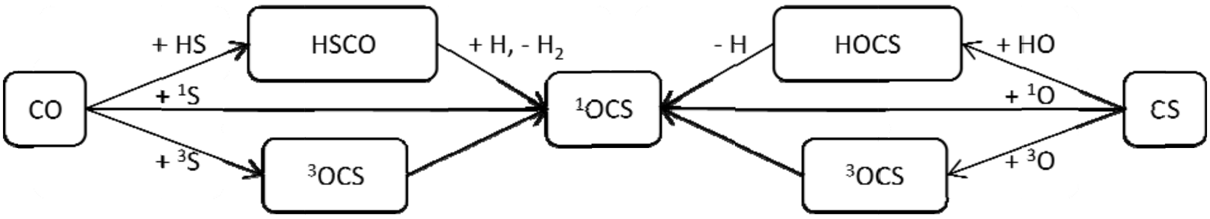

Figure 5.1: The studied reaction pathways to OCS formation, starting from CO and H_2S photo-dissociation products (left hand side), and from CS and H_2O photo-dissociation products (right hand side).

5.2. Previous work

Previous studies of OCS formation and reaction, both experimental and theoretical, have been limited to gas phase reactions (26-40), with the exception of one very recent study (41). Earlier investigations of the OCS system include kinetic studies and the determination of formation reaction rates (35-40), investigations of reaction enthalpies (26-34), and astronomical observations (17-20, 42). Table 5.2 shows a summary of both experimental and theoretical reaction energies determined previously. Experimental work on the CS + O system has been mainly limited to the determination of the rate constant for the formation of CO via reaction (3b').

$$CS + {}^3O \prod [{}^3OCS] \prod CO^* + {}^3S \qquad (3b')$$

The OCS intermediate has not been reported in experimental studies which investigate reaction (3b'), which leads to the conclusion that it is probably short lived. In theoretical work (27-29), however, the intermediate has been investigated and for consistency it was included in the above equation. The experimental work was performed by Slagle *et al.* (35) and Lilenfeld *et al.* (40). Their interest in this reaction lay in the fact that it produced CO with an inverted vibrational population, and hence it could be used for a CO chemical laser. The rate constants reported for CO formation from CS + ^{3}O are 1.24×10^7 m^3 mol^{-1} s^{-1} (35) and 1.57×10^8 m^3 mol^{-1} s^{-1} (40). Slagle *et al.* reported a negligibly small activation energy for this reaction (35). Lilenfeld *et al.* measured an activation barrier for the reaction of CS + ^{3}O → CO + S of 6.3 kJ mol^{-1} (40). Neither publication mentioned OCS, suggesting that if formed at all it would be in the triplet state, which is very unstable and will immediately dissociate to give CO. Hall *et al.* studied photo-dissociation of OCS and report a dissociation energy of +301.0 kJ mol^{-1} into CO + ^{3}S and a dissociation energy of +411.6 kJ mol^{-1} into CO + ^{1}S $^{(26)}$. A study by Ferrante et al. $^{(41)}$ showed that upon irradiation of a mixture of CO and H_2S with protons at low temperatures (10 K), a significant amount of OCS was formed. Moreover the presence of water increased the amount of OCS produced. The study also showed that OCS will be destroyed upon continued irradiation. However the flux of protons which was used was rather high, and shows an OCS half-life of 7 million years in the ISM.

Table 5.2: Energies for gas phase OCS formation from CX + Y, as reported by previous studies. All energies are reported in kJ mol^{-1}. The excitation from ^{1}OCS to ^{3}OCS in this table was calculated using the reported ^{3}S + CO energy and the fact that it was reported to be very close to the ^{3}OCS energy.
*Only a very small barrier was reported without numerical value.

	Lilenfeld $^{(40)}$	**Hall** $^{(26)}$	**Sayós** $^{(28)}$	**Hijazo** $^{(27)}$	**González** $^{(29)}$
^{3}S + CO → ^{3}OCS **Formation energy**	---	---	-144.3	0 *	---
^{3}S + CO → ^{3}OCS **Activation barrier**	---	---	6.7	0 *	---
^{3}O + CS → ^{3}OCS **Formation energy**	---	---	-577.4	0 *	---
^{3}O + CS → ^{3}OCS **Activation barrier**	6.3 *(to CO + S)*	---	50.6	0 *	9.5
^{3}O + CS → ^{3}S + CO **Reaction energy**	---	---	-433.0	-309.7	-379.1
^{1}OCS → ^{3}S + CO	---	+301.0	---	---	---
^{1}OCS → ^{1}S + CO	---	+411.6	---	---	---
^{3}S → ^{1}S	---	110.6	---	93.6	---
^{3}O → ^{1}O	---	---	---	161.1	---
^{1}OCS → ^{3}OCS	---	---	---	~209.4	---

Theoretical studies of the CO + S ∏ OCS ∏ CS + O reaction usually regard OCS as an intermediate, highly reactive, complex. The group of Sayós and González studied the calculated potential energy surface for the reaction ^{3}O + CS → ^{3}S + CO $^{(27-29)}$. Initially it was found that ^{3}OCS is more stable than either ^{3}O + CS or ^{3}S + CO, and that ^{3}OCS in a linear form was the more favourable structure over an angular one. The calculated overall reaction energy for reaction (3b’) was 433.0 kJ mol^{-1}, with a forward activation barrier for $^3O + CS \rightarrow {}^3OCS$ of 50.6 kJ mol^{-1}, and a backwards barrier for the reaction of $^3S + CO \rightarrow {}^3OCS$ of 6.7 kJ mol^{-1}. ^3OCS was found to be 577.4 kJ mol^{-1} more stable than $^3O + CS$, and 144.3 kJ mol^{-1} more stable than $^3S + CO$ (see Table 5.2). Later the group revisited the same reaction pathway (27) and found that ^3OCS was close in energy to $^3S + CO$, with a low activation barrier. Similarly the activation barrier from $^3O + CS \rightarrow {}^3OCS$ was reported to be nearly zero. Moreover, energies of singlet state reactions were also included, from which excitation energies can be calculated. No transition states were found for the formation of ^1OCS starting from either $^1S + CO$ or $^1O + CS$. Their most recent study (29) used high level calculations (UMP4) to calculate the potential energy surface (PES) of eq. (3b') in order to determine the rate constant for the reaction $^3O + CS \rightarrow {}^3S + CO$. About 150 different functions were fitted to the PES, and it was found that a nonlinear approach of the reaction (i.e. a bent ^3OCS) was energetically more favourable. One of their main conclusions was, however, that it was not possible to obtain a PES which would both reproduce the activation energy and the rate constant. Their reported energy barrier at the highest available level of theory (PUMP4/6-311G(2d)) was 9.5 kJ mol^{-1}, in disagreement with their original findings where a very low barrier was reported (27). The overall reaction energy was -379.1 kJ mol^{-1}, a value which lies in between both previously reported values.

Note that the ^3OCS intermediate was not studied in detail in the studies mentioned above, mainly because it has about the same energy as $^3S + CO$, and hence the entropic factor will drive the reaction strongly to the right. However in situations where energy can be transferred, on a dust grain or trapped in ice for example, it may live long enough to thermalise via vibrational energy transfer to the surface or ice.

One experimental study of the formation reaction of OCS, starting from H_2S + CO in an argon matrix, showed the existence of *trans*-HSCO (43). No other experimental studies exist on the formation reactions of OCS starting from either HS + CO or from OH + CS. However the reverse reactions, i.e. reaction of a hydrogen atom with OCS, have been studied and the relevant activation barriers and reaction energies are summarised in Table 5.3, and discussed further below.

Table 5.3: Experimental and theoretical energies for gas phase OCS formation from CX + HY, as reported by previous studies. All energies are reported in kJ mol^{-1}.

	Oldershaw (31)	**Nickolaisen** (30)	**Tsunashima** (36)	**Lee** (37)	**Häusler** (38)	**Rice** (34)
H + OCS → CO + HS Reaction energy	-41	-47.1	-41.0	-46.0	-43	-44.4
H + OCS → CO + HS Activation barrier	---	+16.1	+16.3	+16.1	---	+28.5
H + OCS → CS + OH Reaction energy	+188	+189.5	---	---	+230	+242.7

Nickolaisen *et al.* (30) investigated the collision of a hot hydrogen atom with OCS and obtained an experimental reaction enthalpy of -47.1 kJ mol^{-1} for the H + OCS → CO + HS reaction, with an activation energy of +16.1 kJ mol^{-1}. The second possible reaction, H + OCS → CS + OH, is endothermic by +189.5 kJ mol^{-1} and is consequently much less important. The excess energy of the first reaction was distributed into translational energy (more than 38 %) and into SH and CO internal ro-vibrational excitation. The same system had already been studied by Oldershaw *et al.* (31); however they investigated the influence of different moderator gases and not the energy distribution. They reported a reaction enthalpy of -41 kJ mol^{-1} for H + OCS → CO + SH, and +188 kJ mol^{-1} for H + OCS → CS + OH. However, hot hydrogen atoms were used, implying a source of high energy. Because the environment of dark molecular clouds is cold and quite impenetrable for UV light, the second reaction is of lesser importance to this study. Tsunashima *et al.* (36) studied the kinetics of the abstraction of sulphur atoms from OCS by hydrogen atoms, where they reported a pre-exponential factor of $A = 9.1 \times 10^6$ m^3 mol^{-1} s^{-1} and an Arrhenius activation energy of E_a = +16.3 kJ mol^{-1}, with an overall reaction energy of -41.0 kJ mol^{-1}. Lee *et al.* (37) performed the same reaction, and reported a pre-exponential factor of $A = 5.46 \times 10^6$ m^3 mol^{-1} s^{-1}, an activation barrier of E_a = +16.1 kJ mol^{-1}, and an overall reaction energy of -46.0 kJ mol^{-1}. Häusler *et al.* (38) used deuterium atoms with a kinetic energy of 250 kJ mol^{-1} to dissociate OCS. The formation of CO with a dissociation energy of -43 kJ mol^{-1} was favoured over endothermic formation of CS, where a dissociation energy of +230 kJ mol^{-1} was required. From the measured non-statistical distribution of

DS it was suggested that there is no long-lived HSCO (in this study DSCO) intermediate. In the ISM however, even so-called short-lived radicals can survive for a relatively long period of time.

The group of Rice (32-34) has published three separate theoretical studies of increasing accuracy where the PES of the H + OCS reaction was analysed. The first of their publications (32) used MP4 with a 6-31G** basis set to obtain energies and geometries of various stationary points, intermediates, and transition states. Their second publication (33) used MP4 and QCISD(T) with the 6-311+G(2df,2p) and the aug-cc-pVTZ basis sets, which showed only minor differences from their first study. The PES was reasonably reproduced by DFT using the aug-cc-pVTZ basis, when the B3LYP functional was used. However, significant differences between the *ab initio* results and DFT were obtained with other DFT functionals (including BLYP, BPW91, B3PW91, BP86 and B3P86) (34). The best available energies from their studies at the QCISD(T)/6-311+G(2df,2p) level are shown in Table 5.3. An overall reaction energy for the reaction H + OCS → HS + CO of -44.4 kJ mol^{-1} was calculated. The highest activation barrier on the complex pathway was +28.5 kJ mol^{-1}. The formation of OH + CS was found to be a highly endothermic reaction, with a total energy of +242.7 kJ mol^{-1} with respect to H + OCS.

Finally, in an experimental study performed by Lo *et al.* (43), H_2S is photo-dissociated into H and HS, which then reacts with CO within an argon matrix to form *trans*-HSCO. Their theoretical calculations predict *t*-HSCO to have a similar energy to HS + CO, between -33.0 to +2.5 kJ mol^{-1}, with an activation barrier between +2 to +14 kJ mol^{-1} for the formation of *t*-HSCO. *c*-HSCO is predicted to have a higher energy (9 kJ mol^{-1} higher than *t*-HSCO) and an activation barrier of over +28 kJ mol^{-1}.

5.3. Validation and benchmarking

5.3.1. Methodology

Since differences were noticed in the previously published density functional theory (DFT) results, the DFT functional used here needs to be benchmarked against high-level *ab initio* calculations. The functional used was MPWB1K which is able to reproduce long range interactions and saddle-point energies, as described by Zhao *et al.* (44). The gas-phase molecules and radicals used here have been benchmarked against CCSD(T)/aug-cc-pVTZ calculations with the Molpro program (45). Coronene was used as a carbonaceous dust grain model, and the reactions involving coronene were studied using Gaussian03 (46), with the MPWB1K functional and the 6-311G** basis set, as described in Chapter 2.

5.3.2. Validation and benchmarking

As mentioned above, the functional used was benchmarked against high level calculations. When experimental values are available, functionals can be validated to verify that these values are adequately reproduced by the calculations. Finally, the results obtained were also compared with previous findings of other authors. For computational results, high-level *ab initio* calculations are only available in the gas phase, since calculations on systems including surfaces are not feasible within a reasonable time.

Since most available experimental results were obtained from gas phase reactions, these results were compared with the calculated gas phase results obtained in this work and are shown in Table 5.4.

Table 5.4: Gas phase reaction energies, activation barriers, excitation energies and formation enthalpies for the OCS system. Values in italics refer to activation barriers and all values are in kJ mol^{-1}. Comparison with high-level *ab initio* values and literature values are also included.
s.a. denotes a submerged activation barrier. no ts. Indicates that no transition state was found for this reaction. The energies in the CCCBDB column are experimental enthalpies at 0 K and include formation and excitation enthalpies.

	MPWB1K 6-311G [this study]**	**CCSD(T) aug-cc-pVTZ [this study]**	**Rice (34)**	**CCCBDB (24)**
CO + ^{1}S → ^{1}OCS	-470.03	-352.02	---	-413.47
	no ts.			
CO + ^{3}S → ^{3}OCS	+6.90	+96.48	---	+163.59
	+18.68			
CO + ^{3}S → ^{1}OCS	-301.27	-130.71	---	-302.95
CS + ^{1}O → ^{1}OCS	-946.52	-792.01	---	-851.66
	no ts.			
CS + ^{3}O → ^{3}OCS	-359.27	-230.13	---	-195.30
	s.a.			
CS + ^{3}O → ^{1}OCS	-667.45	-457.32	---	-661.84
CO + HS → H + OCS	+42.08	+121.79	+44.35	+48.04
CO + HS → *t*HSCO	-13.65	+64.26	+2.51	---
	+6.73		*+14.23*	
CO + HS → *c*HSCO	-4.92	+74.13	+11.30	---
	+15.43		*+22.59*	
CO + HS → *i*HSCO	-1.50	---	+10.46	---
	no path		*no path*	
***t*HSCO → *c*HSCO**	+8.73	+9.87	+8.79	---
	+32.01		*+28.45*	
***t*HSCO → *i*HSCO**	+12.15	---	+7.95	---
	+136.22		*+131.80*	
CS + OH → H + OCS	-266.31	-172.01	-242.67	-236.01
CS + OH → *t*HOCS	-260.15		-220.92	---
	s.a.		*s.a*	
CS + OH → *c*HOCS	-259.66	-171.90	-218.40	---
	s.a.		*no ts.*	
CS + OH → *i*HSCO	-309.89	-169.19	-276.56	---
	no path		*no path*	
***t*HOCS → *c*HOCS**	+0.50	-2.71	+2.51	---
	+39.17		*+41.84*	
***t*HOCS → *i*HSCO**	-49.73	---	-55.65	---
	+142.51		*+135.14*	
^{1}OCS → ^{3}OCS	308.18	227.19	---	466.54
^{3}S → ^{1}S	168.76	221.31	---	110.52
^{3}O → ^{1}O	279.07	334.70	---	189.82
H_2 + ^{3}S → H_2S	-292.02	-186.24	---	-292.60
H_2 + ^{3}O → H_2O	-447.30	-300.13	---	-485.71

The table also includes results from the computational chemistry comparison benchmark database (CCCBDB) (24). There is a disagreement between the values calculated here and the high-level *ab initio* calculations, however general trends are well reproduced. The correlation between

CCSD(T) and MPWB1K results has a coefficient of determination R^2=0.9276, with a scaling factor of 1.26 (i.e. DFT values are on average 26% larger than CCSD(T) values). However, the agreement with experimental values is much better. On comparing DFT and CCSD(T) with the experiment, the scaling factor obtained for DFT is 0.9447, whereas the scaling factor of CCSD(T) is 1.1704. The coefficient of determination for DFT is 0.9343, R^2 for CCSD(T) is 0.8868. Because the agreement with the experiments is so good, and because there is a good agreement between our values and the previously reported values by Rice *et al.* **(34)**, the research was performed with the method and functional described here.

5.4. Results and Discussion

Four astrochemically relevant reaction pathways (1) – (4) for the formation of OCS were investigated. The radicals involved in the reactions (S, HS, O, OH) are assumed to be formed by photo-dissociation of saturated molecules (H_2S, H_2O), which are either in the gas phase or have frozen out on an icy dust grain; photo-dissociation of physisorbed H_2S or H_2O may lead to desorption. However, the newly formed molecules may remain in the gas phase, or adsorb onto a dust grain. Hence three mechanisms have been investigated: the Eley Rideal (ER) mechanism, in which case one of the reactants reacts directly from the gas phase; the Langmuir Hinshelwood (LH) mechanism, in which case both reactants are in thermal equilibrium with the surface and react whilst on the surface; and the hot atom (HA) mechanism, in which case one reactant adsorbs on the surface, but reacts before it loses its adsorption energy. In order to investigate the possible reaction pathways, first the adsorption of reactants on the surface is investigated. A high adsorption energy will increase the time a reactant stays on the surface and therefore increase the coverage of reactants. However, if the adsorption energy is so high that a chemical bond is formed between a species and the surface, this species will be immobilised, and the barrier to activation or desorption will be high, such that further reactions may not happen in dark clouds.

In the ISM, one of the important functions of a dust grain surface is the absorption of excess energy from exothermic reactions. Several experimental and theoretical studies (47-56) (see also Chapter 1) have demonstrated the possibility of a grain surface absorbing a part of the excess formation energy. In fact, the formation of H_2 cannot happen in the gas phase under ISM conditions, and it is now believed to occur mainly on dust grains (and not via charged species, as was the case in the early universe, e.g. (57)) . Absorption of excess energy by a surface can proceed via coupling with the phonon modes or coupling with the electronic states of the surface. The adsorption energies of all species involved in (1) – (4) on a coronene surface are shown in Table 5.5 and are compared to available experimental and theoretical values. Results for adsorption on coronene are not always readily available and the experimental and theoretical results refer to adsorption on graphite (highly oriented pyrolitic graphite, HOPG) (denoted with ^{HOPG}), coronene-like PAHs (^{PAH}) and amorphous carbon (^{aC}).

Comparison of the calculated values with experimental values shows that DFT does not perform well for adsorption energies, and the calculated adsorption energies are substantially lower than the experimentally determined values (58-61). This discrepancy could be due to the measured values also including inter-adsorbate interactions on the surface, to the nature of the surface (coronene vs. graphite), as well as to an underestimation of the weak physisorption interactions by the methodology used. Since this computational model appears to underestimate physisorption energies, any effect on catalysis could be enlarged if the true, stronger, interaction is considered, which is especially the case in the HA mechanism. Where this model predicts a positive catalytic effect, it is expected that the actual barrier will be reduced more if the physisorption of the molecules is enhanced. In other words every barrier given here can be seen as an upper boundary to the effective barrier, and thus reactions will happen faster than implied by the present results.

Table 5.5: Calculated adsorption energies using DFT, for relevant species physisorbed on coronene, except for ^1S and ^1O which are chemisorbed. Comparison with experimental results was made where possible, however experimental data is mostly unavailable. Experimental data includes adsorption on HOPG and amorphous carbon (denoted ^{HOPG} and ^{aC}). Theoretical results are adsorption energies on HOPG or coronene-like PAHs such as ovalene (^{HOPG} and ^{PAH}).

	Calculated adsorption energy / kJ mol^{-1} [MPWB1K, this work]	**Experimental adsorption energy / kJ mol^{-1}**	**Previously calculated adsorption energy / kJ mol^{-1}**
^1S	-173.56	---	---
^3S	-8.56	---	---
^1O	-388.89	---	-166.89 – -183.79 $^{HOPG\ (62)}$
^3O	-5.91	---	---
H	+3.14	---	-3.05 – -4.23 $^{HOPG\ (63)}$
CS	-6.25	---	---
CO	-2.56	-13 $^{HOPG\ (61)}$	-10.54 – -20.36 $^{HOPG\ (63)}$
HS	-6.91	---	---
OH	-8.46	---	---
H_2	+2.57	-4.99 $^{HOPG\ (59)}$ < -7 $^{(64,\ 65)}$	-3.78 – -5.02 $^{HOPG\ (63)}$ -5.31 $^{PAH\ (66)}$
H_2S	-6.15	-33.47 $^{aC\ (60)}$	---
H_2O	-9.36	-46 $^{HOPG\ (61)}$ -39.90 $^{HOPG\ (58)}$	-12.06 – -17.85 $^{HOPG\ (63)}$
^1OCS	-7.49	-29.1 $^{HOPG\ (67)}$	---
^3OCS	-17.21	---	---
***cis*-HSCO**	-7.38	---	---
***trans*-HSCO**	-15.13	---	---
***cis*-HOCS**	-17.09	---	---
***trans*-HOCS**	-22.17	---	---

It is also clear from Table 5.5, that most species are physisorbed on the surface, through van der Waals interactions with coronene. Both sulphur and oxygen in their respective first excited ^1D state chemisorb onto coronene, forming three-membered rings including two carbon atoms (an epoxide or thiirane ring respectively). Hence reactions involving these species will not contribute to OCS formation as the species are immobilised on the surface and will no longer be reactive. The calculated negative adsorption energy of both hydrogen (H) and hydrogen gas (H_2) shows that there is a weak interaction with the surface, and that physisorption energies calculated with DFT are to be treated with caution – even when the functional is optimised for weak interactions such as the one employed here. Experimental evidence (59, 64, 65), however, shows that the binding energy of H_2 on a graphene surface is indeed very low – less than 7 kJ mol^{-1}. The calculated value is nearly zero, which agrees with the experimental data. The table also shows that less stable products (i.e. radicals like HS, HSCO and S) are relatively strongly bound to the surface, which means that they can live long enough to accumulate, and eventually react with other particles. Once the reactant or reactants – depending on whether an LH or an ER mechanism is studied – have adsorbed on a surface, the surface can have three different influences on the reaction, as described in Chapter 1. It can cause thermodynamical catalysis by lowering the activation barrier, and it can act as a third body and absorb part of the formation energy. It can also orient the reactants in a more or a less favourable position, which will kinetically catalyse the reactions. The results of the influence of the coronene surface on reactions (1) – (4) are reported below.

5.4.1. CO + S

The sulphur atom in the ground state has the triplet [Ne]$3s^2 3p^4$ electronic configuration. When it associates with CO to form OCS, the singlet state is favoured and thus there will be a crossover somewhere along the reaction path from ^{3}S + CO to ^{1}OCS. A barrierless reaction path was obtained for the gas phase singlet addition reaction (1a), which was exothermic by -168.76 kJ mol^{-1}. ^{1}S chemisorbs on coronene and both the activation barriers for desorption and for reaction with CO are higher than +150 kJ mol^{-1}, therefore the surface reaction (1a) is unimportant in the ISM. For the same reason, the surface reaction (3a) was not studied in further detail. The triplet state reaction (1b) has a gas phase formation energy of +6.90 kJ mol^{-1} and an activation barrier of +18.68 kJ mol^{-1}. Because there will be a triplet – singlet crossover for the formation of ^{1}OCS from ^{3}S + CO, both spin states were calculated to evaluate the actual minimum energy path. Even though it is possible to calculate this very accurately with a multi-reference method (e.g. CASSCF), a more rapid evaluation of the singlet-triplet energy difference clearly showed that the triplet transition state is still about 30 kJ mol^{-1} lower in energy than the same geometry in a singlet state. This is shown in Figure 5.2: the crossover occurs after the activation barrier on the PES, which means that the activation energy on the triplet PES is the rate-limiting step. Therefore reaction (1a) was not further investigated.

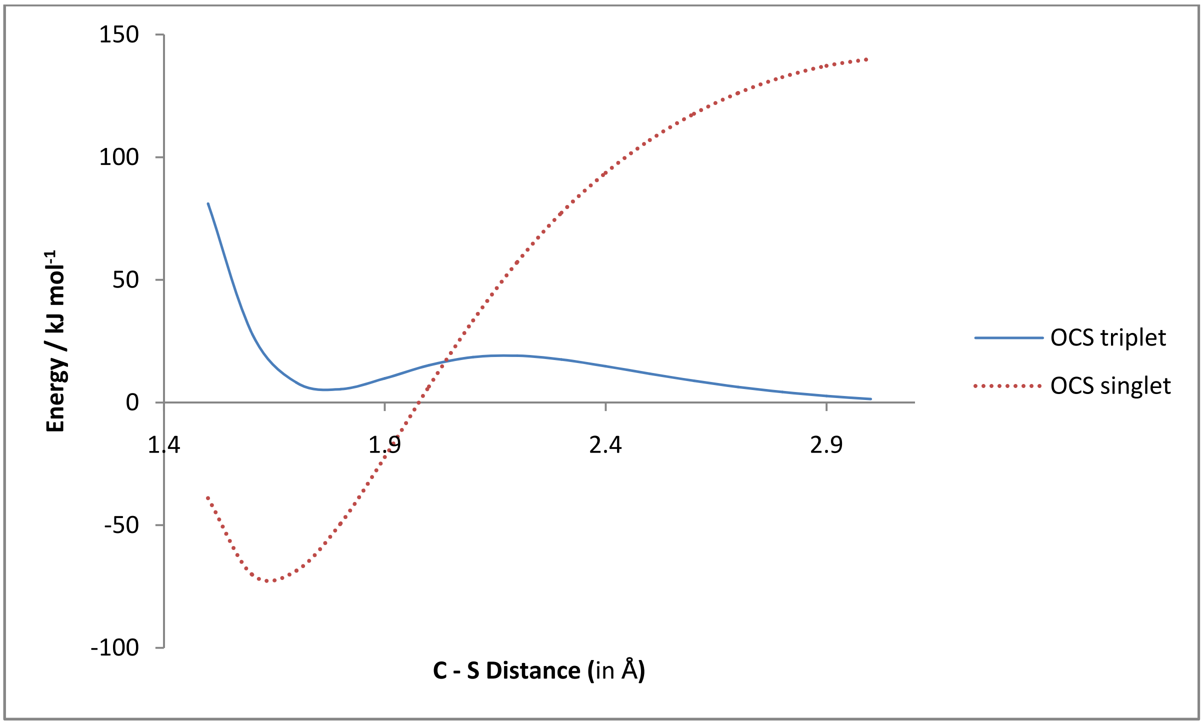

Figure 5.2: Gas phase OCS formation from CO + S. The full line shows ^{3}OCS formation from ^{3}S and CO; the dotted line shows the calculated energy (in kJ mol^{-1}) of ^{1}S + CO → ^{1}OCS. The energy of ^{3}S + CO at infinite distance is set to 0 kJ mol^{-1}. As the distance between C and S, shown on the horizontal axis, decreases (from right to left), the ground state (triplet) curve shows an activation barrier. It is only past this activation barrier (i.e. to its left) that the singlet state crosses the triplet state and becomes more favoured.

As is shown above, a ground state sulphur atom reacting with a CO molecule cannot directly form OCS in the ISM gas phase, as the activation barrier of +18.68 kJ mol^{-1} is too high and the temperature is too low. Thus the influence of a coronene surface could be of major importance. The LH, the HA and the ER reaction pathways were investigated and in all cases the activation barrier was found to be reduced. A 16% reduction down to 15.63 kJ mol^{-1} was seen when both reactants are physisorbed onto coronene (an LH reaction), and a reduction of over 60% to 7.09 kJ mol^{-1} was observed when physisorbed CO reacts with ^{3}S coming from the gas phase (an ER reaction). The HA activation barrier is reduced to 7.07 kJ mol^{-1}, comparable to the ER activation barrier. These values are summarised in Table 5.6. Even though ^3S and CO only physisorb on coronene, it is shown later that this will nevertheless increase the relative amount of successful encounters, and in the specific case of CO + ^3S the activation barrier is reduced enough to allow the reaction to happen in the ISM.

Table 5.6: Gas phase reaction energies and barrier heights for the CO + $^3S \rightarrow {}^3OCS$ reaction. The energies are expressed in kJ mol^{-1}.

Species	Reaction energy	Barrier height
Gas phase	+6.90	+18.68
Langmuir Hinshelwood	+0.81	+15.63
Eley Rideal	-7.74	+7.09
Hot Atom	-7.75	+7.07

5.4.2. CO + HS

The second pathway, shown in reactions (2a) – (2d), starts from CO and HS. The HS radical can be formed from the reaction of a sulphur atom with a hydrogen atom, or from photo-dissociation of H_2S. The reaction of sulphur (^3S) with a hydrogen atom is barrierless, both in the gas phase and on the surface. Hence the limiting factors for a successful reaction are the probability of an encounter and the efficiency of stabilising the product, either by energy transfer to the surface in the case of a surface reaction, or via radiative processes otherwise. As HS has a relatively strong dipole moment (0.76 Debye, compare with 1.85 Debye for water) it can easily radiate away any excess energy in the infrared.

An HS radical, formed either on a surface or in the gas phase, can react with CO, similar to S reacting with CO. Three possible reaction products were studied, referred to as *cis*, *trans*, and *iso*, as shown in Figure 5.3. All three structures are minima on the PES. Forming the *iso*-HSCO isomer involves breaking the HS bond, and hence the activation barrier for its formation is very high. *Iso*-HSCO will therefore not be formed from HS + CO in the ISM. One might argue that *cis*- or *trans*-HSCO could isomerise to *iso*-HSCO. These barriers were therefore evaluated, but they are found to be much higher than the barrier for dissociation of either HSCO radical into HS + CO. Thus *iso*-HSCO will not be formed, and hence it will not contribute to OCS formation. Therefore *iso*-HSCO formation was not studied on the surface.

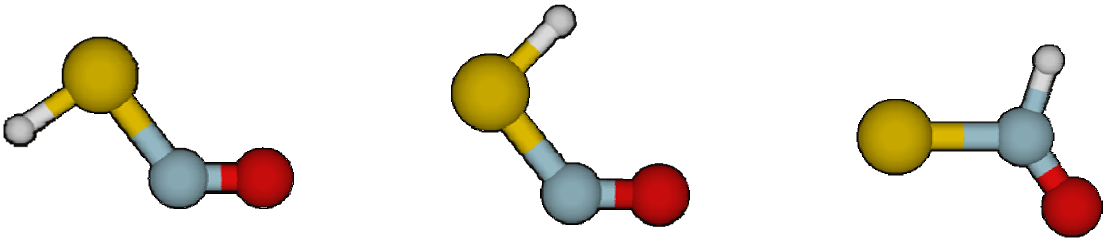

Figure 5.3: Three possible HSCO orientations are shown: from left to right *trans*-HSCO, *cis*-HSCO, *iso*-HSCO. Carbon is grey, oxygen is red, sulphur is yellow and hydrogen is white.

The reaction pathways for reactions (2a) and (2b) are shown in Figure 5.4. The reaction profiles for ER, LH, HA and gas phase reactions are very similar; reaction energies and activation barriers are reported in Table 5.7. The calculations indicate that both the formation of *cis*- and *trans*-HSCO are catalysed on a surface; the activation barriers are reduced by a few kJ mol^{-1}. When the formation of either *cis*-HSCO or *trans*-HSCO proceeds via the ER mechanism, the CO molecule is required to tilt over in order to reach the optimal transition state. This process requires less than 1 kJ mol^{-1}, which shows that CO is only loosely bound to the surface, and that the orientation of CO on a carbonaceous surface will be very random, at least at extremely low coverage, in agreement with experiments (68).

Even though the catalytic effect of coronene is insufficient for *cis*-HSCO to be formed in the ISM, the reduced barrier does increase the speed of formation of *trans*-HSCO appreciably. It should also be noted that for the LH formation of *cis*-HSCO, an increase in the activation barrier height is found, which is mainly due to the fact that the HS radical strongly physisorbs on the surface, stabilising the reactant more strongly than the transition state. Isomerisation in the gas phase from *trans*- to *cis*-HSCO is activated by 32.01 kJ mol^{-1}, and from *cis*- to *trans*-HSCO is activated by 23.28 kJ mol^{-1}. On a surface, these energies are increased, since now there will also be steric hindrance.

Isomerisation from *cis*-HSCO to *trans*-HSCO and vice versa will therefore not happen. Hence, once *trans*-HSCO or *cis*-HSCO is formed, the radical will not transform to the other isomer.

Table 5.7: Calculated reaction energies and barrier heights for the CO + HS reaction, forming each of the three HSCO intermediates. The energies are expressed in kJ mol^{-1}. Barrier heights are in italics.
**The *trans*- isomer is formed via an LH type reaction.

Species		**Gas Phase**	**Langmuir Hinshelwood (LH)**	**Eley Rideal (ER)**	**Hot Atom (HA)**
CO + HS →	ΔE	-4.92	-2.83	-9.74	-9.74
***cis*-HSCO**	$\Delta E^{\neq}$	*+15.43*	*+16.23*	*+13.27*	*+9.32*
CO + HS →	ΔE	-13.65	-19.30	-26.21	-26.21
trans-HSCO	$\Delta E^{\neq}$	*+6.73*	*+3.30*	**	*-3.61*
CO + HS →	ΔE	-1.49	*Not calculated –*	*Not calculated –*	*Not calculated –*
***iso*-HSCO**	$\Delta E^{\neq}$	*>100*	*see text*	*see text*	*see text*

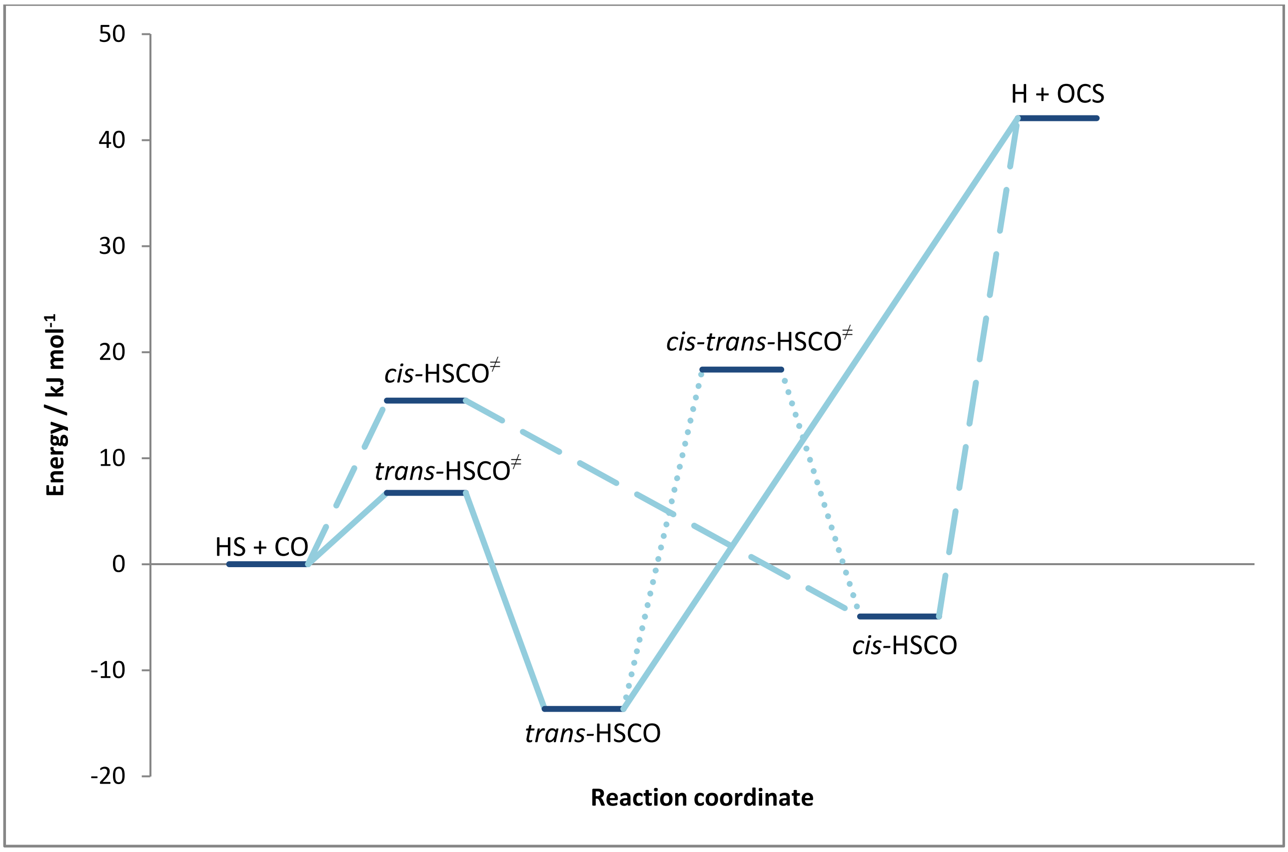

Figure 5.4: Reaction energy path for OCS formation from HS and CO. The energies shown on the graph are valid for the gas phase, ER and LH reactions. The effective values for the gas phase, LH and ER reactions are reported in Table 5.7.

OCS can now be formed, either from *cis*- or *trans*-HSCO. To form OCS, the radical has to lose a hydrogen atom, which is endothermic by +55.73 kJ mol^{-1} for *trans*- and +47.00 kJ mol^{-1} for *cis*-HSCO (see Figure 5.4 and Table 5.7); hence spontaneous dissociation into OCS + H can be excluded as a possible reaction in the ISM.

An alternative possibility for OCS formation from HSCO is an encounter with a hydrogen atom. The outcome of a reaction of HSCO with a hydrogen atom depends on how this hydrogen atom approaches the HSCO radical. In the gas phase, hydrogen can attack any of the four atoms of HSCO. However, since attack via the oxygen atom would yield a very unstable HSCOH structure, and since on the surface steric hindrance (see Figure 5.5) prevents attack of the carbon atom, only two possible reactions can occur. Both reactions are entirely barrierless and strongly exothermic, and in the gas phase they are approximately equally likely to happen. One of the reactions leads to OCS formation, whereas the other one destroys the HSCO radical to yield the starting products again. Both reactions are shown below in (5a) and (5b).

- $H + HSCO \rightarrow H_2 + OCS$ (5a)
- $H + HSCO \rightarrow H_2S + CO$ (5b)

On a surface, however, the relative orientation of the HSCO intermediate with respect to the surface will have a strong influence on how the incoming hydrogen atom can attack. For *cis*-HSCO, the more stable HSCO orientation has carbon and sulphur closest to the surface, with both hydrogen and oxygen pointing away from the surface. Formation of H_2 and OCS is hence favoured in the ER case, whereas LH and HA would favour CO + H_2S formation. The *trans*- isomer of HSCO has a similar general structure to *cis*-HSCO, with the obvious difference that hydrogen is pointing down towards the surface. Here, H_2S formation is favoured in the ER case and OCS formation is more likely formed in the LH and HA cases. Figure 5.5 shows, for both *cis*- and *trans*-HSCO, the most stable orientations on a coronene surface.

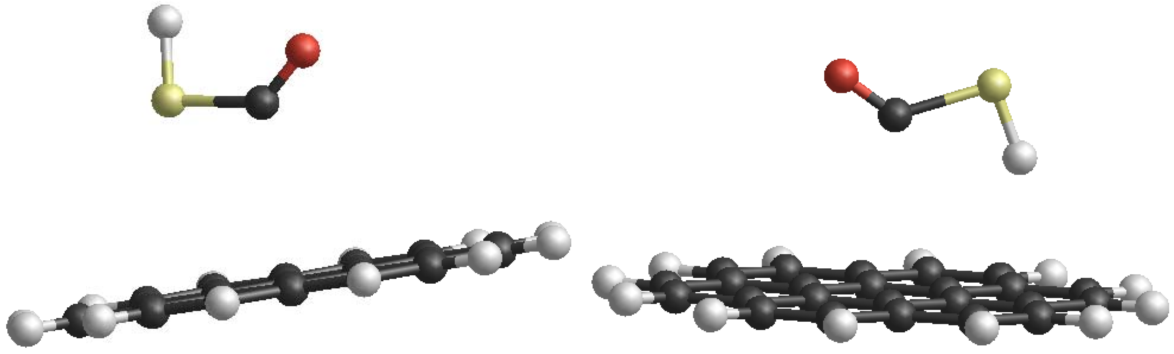

Figure 5.5: Most stable orientations of *cis*-HSCO (left) and *trans*-HSCO (right) on a coronene surface.

The calculations have shown that, either coming from the gas phase or first freezing out on a surface, HS can react with CO to form an HSCO intermediate. This radical intermediate will be in the form of one of two isomers and will be physisorbed until it reacts with another species. Both in the gas phase and on the surface, the *trans*-isomer is both the kinetic and the thermodynamic product: both the activation barrier and the reaction energy are lower for this isomer. For ER and LH reactions, the *trans*-isomer is favoured strongly. The most probable species that will encounter and react with this intermediate is a hydrogen atom. This reaction is barrierless and yields CO and H_2S or H_2 and OCS.

5.4.3. CS + O

The reaction of CS + O differs significantly from the previously studied reaction of CO + S. The CO bonding distance is a lot shorter than the CS distance (1.12 Å vs. 1.52 Å) because overlap between the carbon 2p and sulphur 3p orbitals is not as effective as that between carbon 2s + 2p and oxygen 2s + 2p orbitals. Secondly the sulphur atom is larger and is therefore a more stable radical than oxygen. In the gas phase, these two differences result in the fact that when CS reacts with a ^3O atom, a complex is initially formed. In this complex, oxygen is still relatively far away from the carbon atom (around 2.7 Å); however there is a stabilisation of -3.66 kJ mol^{-1}, which is probably due to overlap between the oxygen 2p- and CS π^*-orbitals. When oxygen moves closer to the carbon atom, the transition state towards ^{3}OCS is 0.97 kJ mol^{-1} higher in energy than the complex. Overall the formation of ^{3}OCS from CS and ^{3}O is not activated as the transition state is 2.69 kJ mol^{-1} lower in energy than the gas phase separated reactants. This barrier is referred to as submerged (69). The catalytic effect of the surface reduces the submerged activation barrier below the computational numerical accuracy. Table 5.8 shows the formation energies and activation energies for reaction (3b): CS + ^{3}O → ^{3}OCS. Figure 5.6 shows, as with CO + ^{3}S, the difference in energy between CS + ^{1}O and CS + ^{3}O, when the distance between C and S changes.

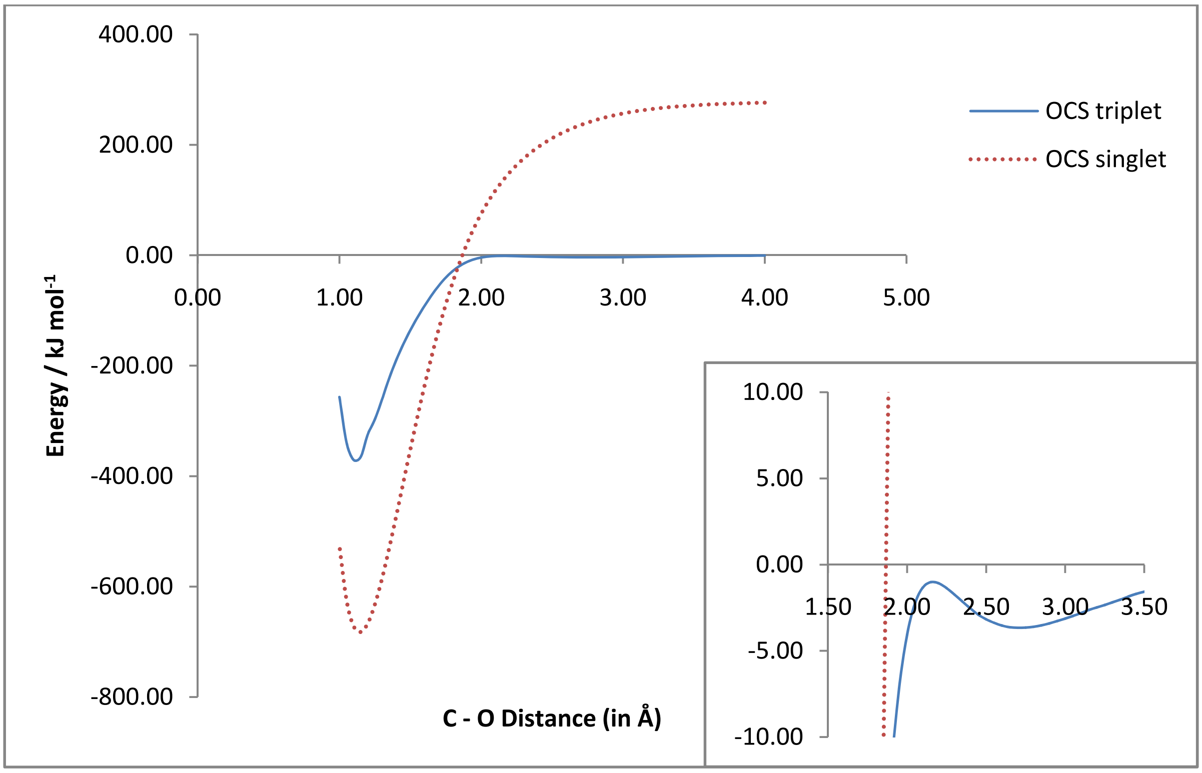

Figure 5.6: Gas phase OCS formation from CS + O. The full line shows ^{3}OCS formation from ^{3}O and CS; the dotted line shows the calculated energy (in kJ mol^{-1}) of ^{1}O + CS → ^{1}OCS. The energy of ^{3}O + CS at infinite distance is set to 0 kJ mol^{-1}. As the distance between C and O, shown on the horizontal axis, decreases (from right to left), the ground state (triplet) curve shows a submerged activation barrier. It is only past this activation barrier (i.e. to its left) that the singlet state crosses the triplet state and becomes more favoured. The inset shows a zoom-in of the transition state area, to show the submerged barrier.

The importance of the surface now lies not in reducing the activation barrier, since the gas phase activation barrier is submerged. However, the formation energy is larger than 350 kJ mol^{-1}; therefore stabilisation of the ^{3}OCS molecule and an immediate removal of the formation energy are of major importance, otherwise the molecule will immediately dissociate into ^{3}S and CO. The adsorption energy of CS is more than twice as large as that of CO; thus desorption will be less effective, leading to a higher reaction rate. Catalysis in the classical way is commonly viewed as a reduction of the (Arrhenius) activation barrier of a reaction. In view of the ISM environment and the effect dust grains have on reactions, it is more appropriate to broaden the definition of catalysis, since clearly physisorption of the reactants on a dust grain, and the dust grain acting as a heat sink, will lead to an increase of the reaction rate. Thus, at the extremely low pressure of the ISM, catalysis includes both of these physisorption influences in addition to classical catalysis. Finally, a surface can increase or decrease the probability of a successful encounter, depending on the geometry of adsorption. When a molecule is adsorbed with its reactive site pointing towards the surface, the probability of a reactive encounter with gas phase species is reduced. When a molecule is adsorbed the other way around, the probability of a reactive encounter increases. This can be referred to as kinetic catalysis, in contrast to thermodynamic catalysis where the activation barrier is lowered.

Table 5.8: Calculated reaction energies and barrier heights for the CS + ^{3}O → ^{3}OCS reaction. The energies are expressed in kJ mol^{-1}.

[*] All activation barriers are submerged. The values given for the gas phase formation are the complexation energy and the submerged activation barrier with respect to the starting products at infinite distance.

Species	Reaction energy	Barrier height*
Gas phase	-359.27	*-3.66* *-1.02*
Langmuir Hinshelwood	-364.33	*Submerged*
Eley Rideal	-370.23	*Submerged*
Hot Atom	-370.23	*Submerged*

Table 5.9 summarises, for reactions (1) and (3), the geometrical and energetic properties of CO, CS, OCS, and the transition states in the gas phase. From this table it can be seen that the CS bonding distance does not vary substantially on going from the free CS molecule to the complex and

the transition state. This, however, is not the case for CO reacting with ^3S, where the CO bonding distance clearly stretches, the explanation for which can be found in the weaker overlap between the carbon and sulphur orbitals.

Table 5.9: Properties of OCS and OCS transition states. Distances are in Å (1 Å = 10^{-10} m), energies are in kJ mol^{-1} and relative to ^3OCS. CO and CS are assumed to include a ^3S and a ^3O atom respectively. The geometries are gas phase geometries.

		CO (+^3S)	CS (+^3O)	^1OCS	^3OCS	$^3S..CO^‡$	$^3O..CS^{cpl}$	$^3O..CS^‡$
r_{CO} / Å		1.1161	∞	1.1417	1.1652	1.1276	2.7163	2.2638
r_{CS} / Å		∞	1.5236	1.5552	1.7726	2.1720	1.5219	1.5224
a_{OCS} / °		----	----	180.0	121.9	122.1	139.8	125.6
Relative energy (to ^3OCS) / kJ mol^{-1}	Gas phase	-6.90	359.27	-308.18	0.00	11.77	355.61	356.58
	LH	-0.81	364.33	-298.46	0.00	14.81	---	---
	ER (and HA)	7.74	370.23	-295.96	0.00	14.83	---	---
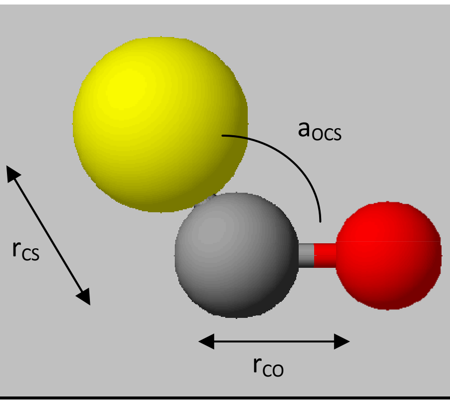								

Upon reaction of ^3O with CS, 360 kJ mol^{-1} of energy is released, which can either be absorbed by the surface as vibrational energy, or can be used to dissociate ^3OCS into ^3S and CO. Moreover, a similar amount of energy is released when ^3OCS falls back to the ^1OCS ground state, which may lead to OCS desorption.

5.4.4. CS + OH

When an OH radical is formed, either from oxygen reacting with hydrogen or directly upon photo-dissociation of water, it can react with CS on a dust grain. Contrary to the formation of HSCO, spontaneous dissociation of H from the HOCS intermediate to give OCS is exothermic. Therefore OH

+ CS can yield OCS + H directly. As with the reaction of CS + ^{3}O, an intermediate complex is formed, which will then lead to either *cis*- or *trans*-HOCS. The gas-phase activation barrier towards *trans*-HOCS, starting from the complex, is only +3.64 kJ mol^{-1}, which can easily be overcome by the energy released upon formation of the complex (-14.47 kJ mol^{-1}). *Trans*-HOCS can subsequently isomerise to *cis*-HOCS with a reaction barrier of +39.17 kJ mol^{-1}. The formation energy of the *trans*-isomer (> 260 kJ mol^{-1}) is sufficient to overcome the activation barrier to isomerisation to the *cis*-isomer in a near-thermoneutral reaction. *Cis*-HOCS can then continue to yield H + OCS with a gas phase activation energy of +86.81 kJ mol^{-1}. This barrier can easily be overcome if the internal redistribution of energy is faster than intramolecular energy transfer.

The catalytic influence of a coronene surface for this reaction is similar to that in the CS + O reaction. The activation energy to *trans*-HOCS is submerged, and thus the adsorption of HOCS on the surface, plus the third-body effect of the surface, are more important than any catalytic effect. However, it should be noted that in this sequence of reactions, the last step (formation of OCS from *cis*-HOCS) is slightly endothermic on a surface because of the large adsorption energy of the HOCS intermediate.

Table 5.10 shows the relative energies of HOCS formation in the gas phase and for both the LH and ER surface reaction mechanisms. It is noted that the activation barriers are very large; therefore, if dissociation does not happen immediately after formation of HOCS, the radical will not dissociate spontaneously but will continue to exist on the surface. As with the case of HSCO, another hydrogen atom can react with either *cis*- or *trans*-HOCS; these reactions are shown in (6a) and (6b). Again, there is an approximately 50% chance of H_2 + OCS formation, depending on the angle of approach of the hydrogen atom. When the hydrogen atom approaches from the oxygen end, H_2O and CS are formed instead. Reactions of HOCS + H are all barrierless; thus the outcome of the reaction mainly depends on the angle of approach.

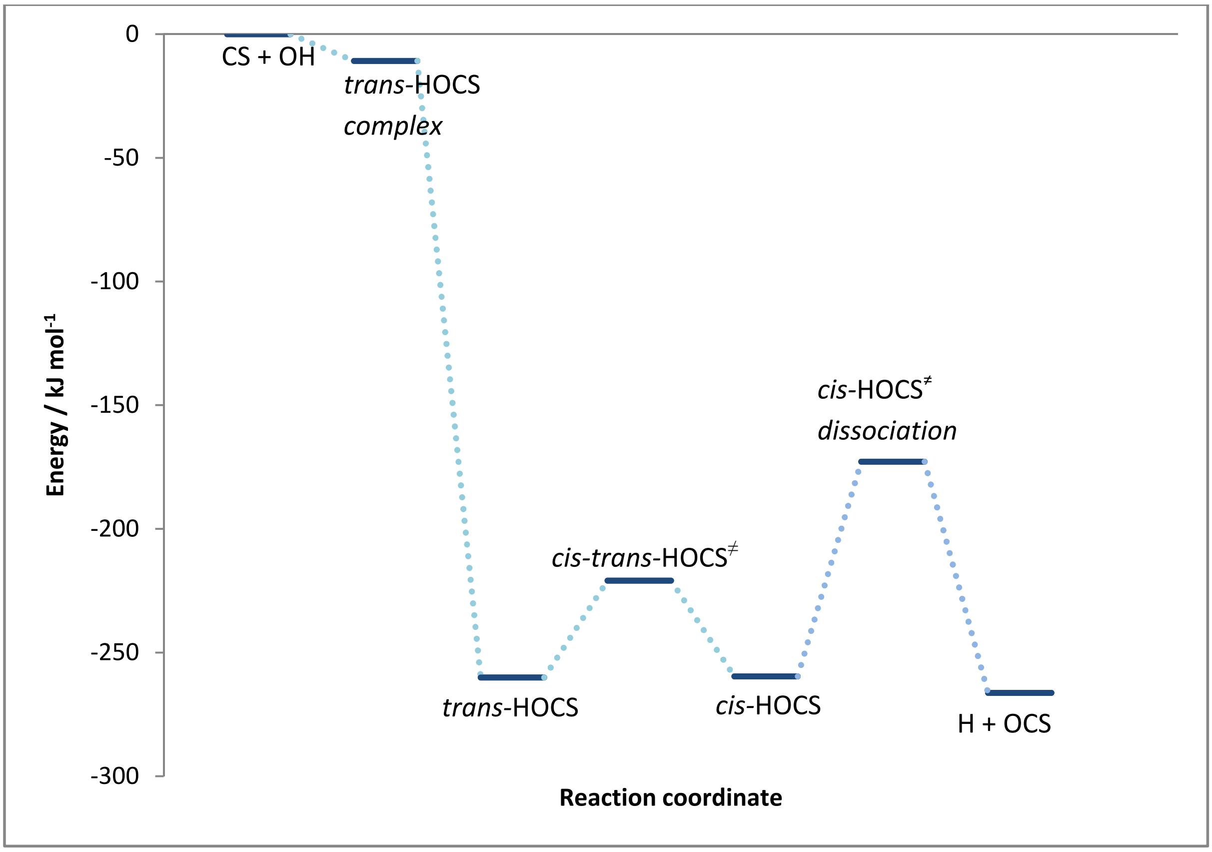

Figure 5.7: Gas phase reaction energy path for OCS formation from CS and OH. The energies shown on the graph are valid for the gas phase, ER and LH reactions. The effective values for the gas phase, LH and ER reactions are reported in Table 5.10.

- $H + HOCS \longrightarrow H_2 + OCS$ (6a)
- $H + HOCS \longrightarrow H_2O + CS$ (6b)

Table 5.10: Calculated reaction energies and barrier heights for the CS + OH reaction. The energies are expressed in kJ mol^{-1}. Barrier heights are in italics.

[*] The isomerisation of *trans*- to *cis*-HOCS is written as a LH reaction, as is the transition state for *cis*-HOCS dissociation.

Reaction	**Gas Phase**	**Langmuir Hinshelwood (LH)**	**Eley Rideal (LH)**
CS + OH ⟶ *trans*-HOCS	-10.83 *(complex)* -260.15	-267.61	-276.08
***trans*-HOCS ⟶ *cis*-HOCS**	+0.49 *+39.17*	+5.58 *+39.60*	* *
***cis*-HOCS ⟶ H + OCS**	-6.65 *+86.81*	+6.08 *+94.70*	+5.45 *

Clearly OCS can be formed in two ways from CS + OH: without an additional hydrogen atom, if the reaction proceeds fast enough, or similar to the formation from CO + HS with an additional hydrogen atom, in which case most reactions leading to OCS formation are barrierless, both in the gas phase and on the surface.

5.4.5. Comparison with CO_2 formation reactions

Previous work in our group investigated the effect of coronene on CO_2 formation via similar pathways to those which led to the formation of OCS (25). Here a direct comparison is made between the two sets of reactions, namely:

- $CX + {}^3Y \rightarrow {}^3CXY$ (7)

  $CO + S \rightarrow OCS$ (7a)

  $CS + O \rightarrow OCS$ (7b)

  $CO + O \rightarrow CO_2$ (7c)

- $CX + HY \rightarrow CXY + \ldots$ (8)

  $CO + HS \rightarrow [\ldots] \rightarrow OCS$ (8a)

  $CS + OH \rightarrow [\ldots] \rightarrow OCS$ (8b)

  $CO + OH \rightarrow [\ldots] \rightarrow CO_2$ (8c)

As was mentioned at the beginning of this chapter, OCS and CO_2 are isovalent and therefore comparison of the reactions can tell us about the difference in reactivity between oxygen and sulphur. Figure 5.8 shows the reaction energy profiles of reactions (7) (see also Tables 5.6, 5.8 and 5.9), and Figure 5.9 shows all three reactions (8) (see also Tables 5.7 and 5.10; Figures 5.4 and 5.7). All of the reactions are firstly compared in the gas phase. In a second stage, comparison of the catalytic effects of a coronene surface will be made. The energies of the resultant products have been set to zero for comparison purposes.

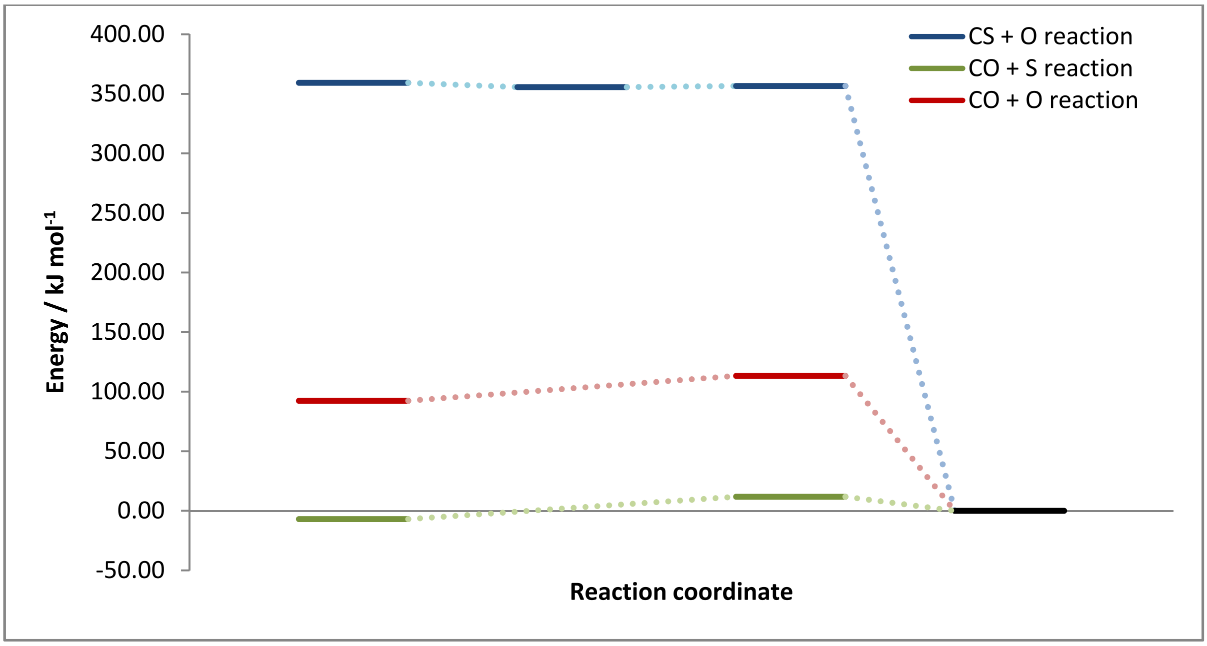

Figure 5.8: Gas phase reaction energy path for CX + Y reactions. Energies are reported in kJ mol^{-1}.

From the first set of reactions, it can be seen that the CO + O reaction behaves similarly to the CO + S reaction. No intermediate complex is formed, but a transition state must be overcome in order for the reaction to proceed to the products. The reaction of OH + CO is more comparable with that of OH + CS. First a complex is formed, leading to the *trans*-isomer. This will in turn isomerise to the *cis*-form, in both (7b) and (7c), which can then dissociate to give the product plus a hydrogen atom.

Comparison of these two sets of reactions leads to two conclusions: firstly, the OH radical is more reactive than the HS radical, hence OH forms complexes before reaction. OH is more reactive, since oxygen is a smaller atom than S, and can therefore less easily accommodate an unpaired electron. Secondly, the CO molecule is less reactive than the CS molecule, and therefore does not form complexes as easily as CS. This conclusion can be understood in terms of orbital overlapping: S is a third-row element whereas O and C are second-row elements, hence providing a better and more effective overlap and thus a stronger bond.

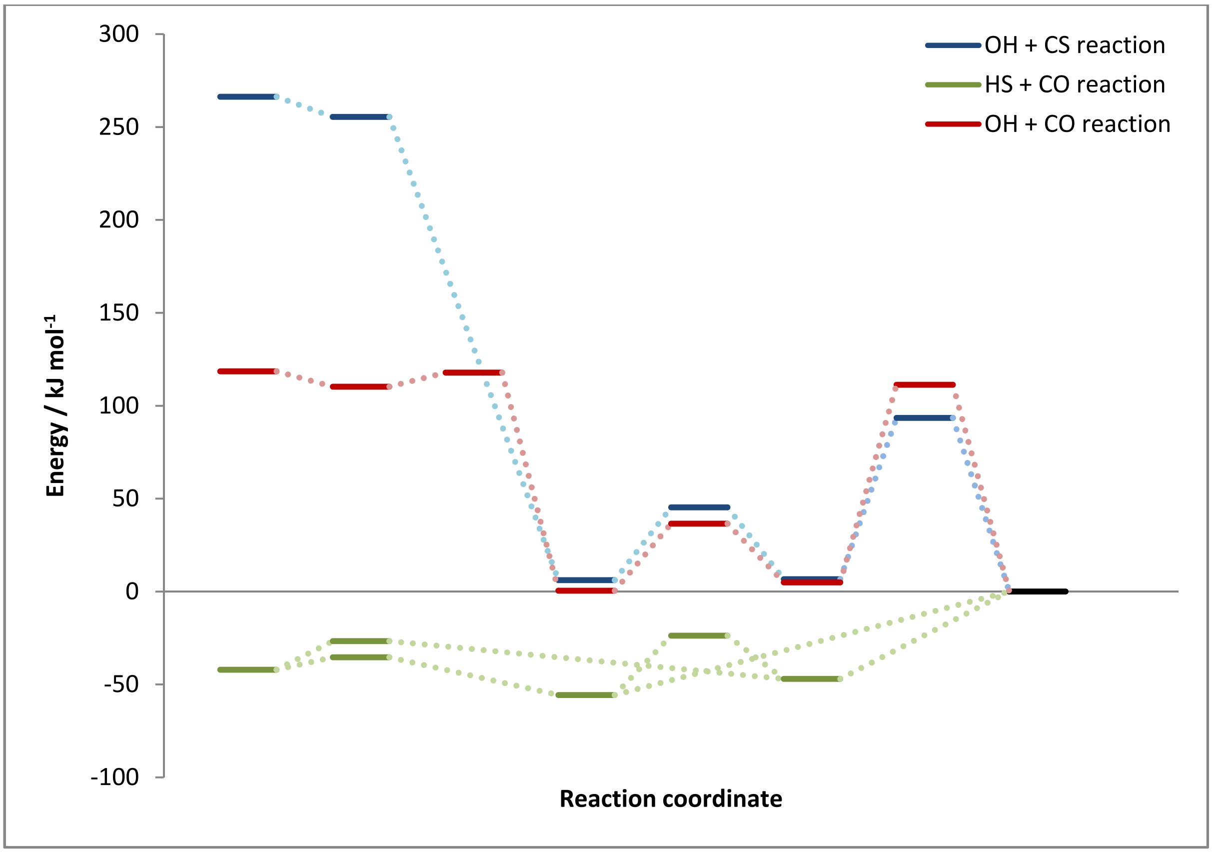

Figure 5.9: Gas phase reaction energy path for CX +HY reactions. Energies are reported in kJ mol^{-1}.

A catalytic effect is observed for the CO + O reaction on coronene: the ER activation barrier is 10% lower than the gas phase barrier (+19 kJ mol^{-1} instead of +22 kJ mol^{-1}), and the hot atom mechanism has an even lower activation barrier (of only about +13 kJ mol^{-1}). The CO + S reaction studied in this research experiences a stronger catalytic effect (a reduction of the gas phase activation barrier from +18.68 kJ mol^{-1} to +7.09 kJ mol^{-1}, 62%). In both cases CO is adsorbed on the surface, and reacts with the other atom (O, S) from the gas phase (ER mechanism). Therefore, it is the transition state geometry which is stabilised more in the formation of OCS than the formation of CO_2. The OH + CO reaction, which in the gas phase has a submerged activation barrier of -0.68 kJ mol^{-1} to *t*-HOCO formation, has an even more submerged activation barrier of -1.90 kJ mol^{-1} on a coronene surface. In comparison, the CO + HS barrier is reduced from +6.73 kJ mol^{-1} to +3.30 kJ mol^{-1}, a 51% reduction; the CS + OH reaction has no barrier.

The explanation for the catalytic behaviour of the surface is twofold. Firstly, CO has a strong bond and only a small dipole moment. Only a large electronic perturbation, as is provided by the sulphur atom, in combination with the electronically stabilising π-orbitals of coronene, can disrupt the double π-bond of CO enough for a strong catalysis to happen. An approaching oxygen atom does not change the π-electrons of CO enough, and coronene alone does not substantially modify the electron cloud either. Secondly, CS has a large bond and a relatively large dipole moment (around 1.51 Debye), which makes it much more easy to influence the electron cloud around it. An approaching atom or radical can hence easily associate with it, which is shown in the submerged activation barriers. The nearby coronene surface will facilitate this effect by stabilising a larger dipole and by accommodating electrons in its π-orbitals. Therefore, the catalytic effect of coronene on OCS formation is larger than its effect on CO_2 formation.

5.5. Astrochemical implications

In order to predict protostellar and interstellar evolution, astrochemical models use chemical rate equations, which allow for chemical species to evolve through time. The parameters used in these rate equations are the pre-exponential factor, the activation energy, and an eventual temperature dependency. As was mentioned in Chapter 2, from transition state theory and frequency calculations the pre-exponential factor of a reaction can be obtained. The calculated values of the rate constants, pre-exponential factors and barrier heights for the formation reactions of OCS are displayed in Tables 5.11 and Table 5.12, at a temperature of 10 K. The reaction rates are dependent on the coverage θ of physisorbed species (expressed in mol m^{-2}) and, in the Eley Rideal case, on the concentration of the gas phase species. These values are calculated as described in Chapter 2.

Table 5.11: Reaction rates (r), pre-exponential factors (A) and activation barriers ($\Delta E^{\neq}$) for Langmuir Hinshelwood type reactions at temperature T = 0 K. The reaction rates are dependent on the surface coverage θ_X of chemical species.

Reaction	**r / mol m^{-2} s^{-1}**	**A / m^2 mol^{-1} s^{-1}**	**$\Delta E^{\neq}$ / kJ mol^{-1}**
CO + ^{3}S → ^{3}OCS	$8.706 \times 10^{14}\ \theta_{CO}\ \theta_S$	1.051×10^{15}	15.63
CO + HS → *trans*-HSCO	$1.010 \times 10^{15}\ \theta_{CO}\ \theta_{HS}$	1.051×10^{15}	3.30
CO + HS → *cis*-HSCO	$8.919 \times 10^{14}\ \theta_{CO}\ \theta_{HS}$	1.084×10^{15}	16.23
CS + ^{3}O → ^{3}OCS	$2.396 \times 10^{15}\ \theta_{CS}\ \theta_O$	2.396×10^{15}	*s.a.*
CS + OH → *trans*-HSCO	$1.818 \times 10^{15}\ \theta_{CS}\ \theta_{OH}$	1.818×10^{15}	*s.a.*
***trans*-HSCO → *cis*-HSCO**	$1.418 \times 10^{16}\ \theta_{HSCO}$	2.283×10^{16}	39.60
***cis*-HSCO → H + OCS**	$9.763 \times 10^{15}\ \theta_{HSCO}$	3.050×10^{16}	94.70

Table 5.12: Reaction rates (r), pre-exponential factors (A) and activation barriers ($\Delta E^{\neq}$) for Eley Rideal type reactions at temperature T = 0 K. The reaction rates are dependent on the surface coverage θ_X and the gas phase concentration [Y] of chemical species.

Reaction	**r / mol m^{-2} s^{-1}**	**A / m^3 mol^{-1} s^{-1}**	**$\Delta E^{\neq}$ / kJ mol^{-1}**
CO + ^{3}S → ^{3}OCS	$9.513 \times 10^{4}\ \theta_{CO}$ [S]	1.148×10^{5}	7.09
CO + HS → *trans*-HSCO	$1.094 \times 10^{5}\ \theta_{CO}$ [HS]	1.138×10^{5}	3.30
CO + HS → *cis*-HSCO	$8.579 \times 10^{4}\ \theta_{CO}$ [HS]	1.043×10^{5}	13.27
CS + ^{3}O → ^{3}OCS	$3.357 \times 10^{5}\ \theta_{CS}$ [O]	3.357×10^{5}	*s.a.*
CS + OH → *trans*-HSCO	$2.970 \times 10^{5}\ \theta_{CS}$ [OH]	2.970×10^{5}	*s.a.*

Equation 2.28 is repeated here (symbols are explained in Chapter 2) and shows how a pre-exponential factor can be calculated from the vibrational frequencies:

$$A = \frac{hN_A}{2\pi m} \frac{\exp\left(\sum_i \ln\left(1 - \exp\frac{-v_i}{T}\right)^{-1}\right)^{\neq}}{\exp\left(\sum_i \ln\left(1 - \exp\frac{-v_i}{T}\right)^{-1}\right)^{R}} \tag{5.1}$$

Equation (5.1) shows that the (Langmuir Hinshelwood) pre-exponential factor A is dependent on the temperature T. The (Arrhenius) rate constant of a reaction is given by equation (5.2).

$$k = A\exp\left(-\frac{\Delta E^{\neq}}{RT}\right) \tag{5.2}$$

The rate constant k is hence also dependent on the temperature. From equations (5.1) and (5.2), one can see that the temperature dependence of the rate constant is not a simple expression.

At every temperature, there is a certain rate of reaction, dependent on the coverage and (in the case of ER) the H_2 gas pressure. The reaction rate competes with the rate of desorption, which, as in the case of H_2O, is assumed to be a first-order desorption for every adsorbed species.

$$\frac{r_{rxn}}{r_{des}} = \frac{A_{rxn}}{A_{des}} \exp\left(\frac{\Delta E_{des} - \Delta E^{\neq}_{rxn}}{RT}\right)\{X\} \tag{5.3}$$

In equation (5.3), r_{rxn} and r_{des} are the rate of reaction and the rate of desorption respectively. A_{rxn} and A_{des} are the respective pre-exponential factors, ΔE_{des} is the adsorption energy and $\Delta E^{\neq}_{rxn}$ is the activation barrier. T is the temperature, and finally $\{X\}$ is the coverage of *X* in the case of LH reactions, and the partial pressure of *X* in the case of ER reactions, where *X* is one of the two reactants, usually assumed to be the most volatile; i.e. with the species with the lowest adsorption energy. This ratio (5.3) will show, at each temperature, how likely reaction is before desorption happens. These numbers give us more insight into the processes happening inside dark, molecular clouds. Figures 5.10 and 5.11 show, for the LH and ER mechanisms, the temperature dependence shown in (5.3) for temperatures ranging from 1 to 100 K.

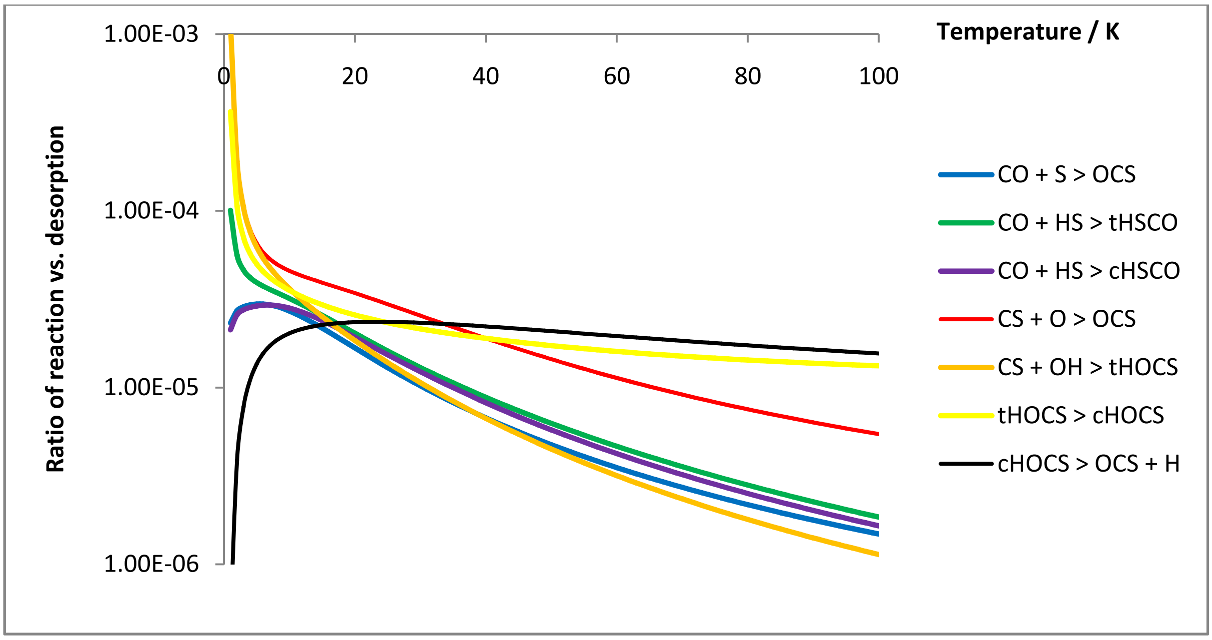

Figure 5.10: Temperature dependency of the ratio of reaction vs. desorption for the reactions shown in Table 5.11 (LH).

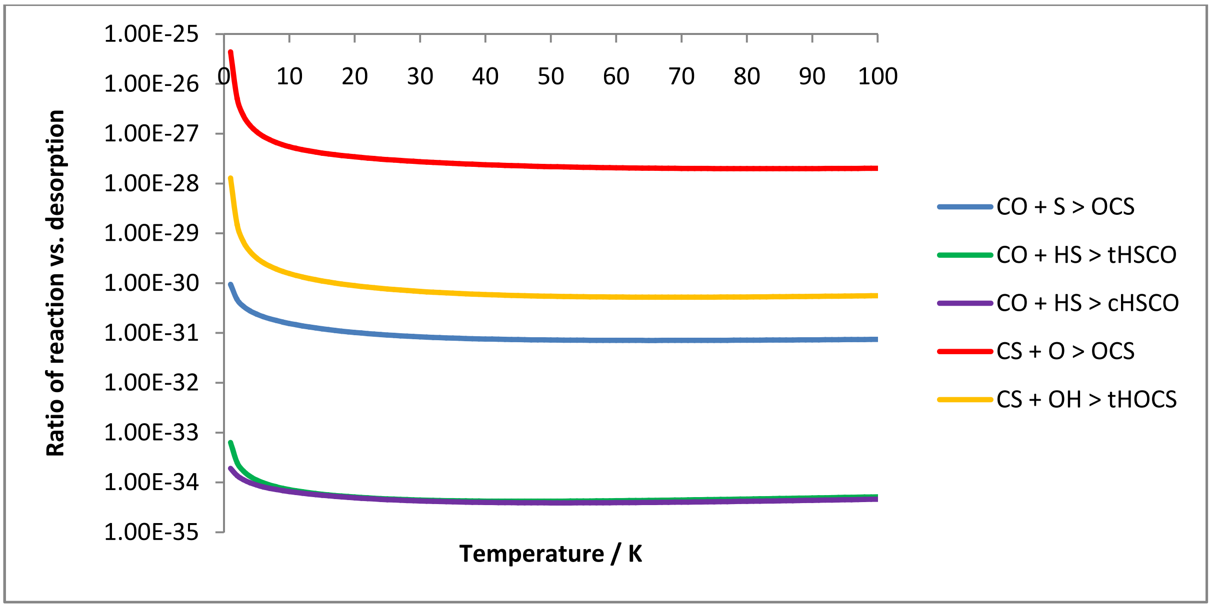

Figure 5.11: Temperature dependency of the ratio of reaction vs. desorption for the reactions shown in Table 5.12 (ER).

These results, as shown in Tables 5.11 and 5.12, and Figures 5.10 and 5.11, using equation (5.3) and the parameters calculated in this research were implemented in an astrochemical network. They have shown that the inclusion of these reactions increases the concentration of OCS by 3 orders of magnitude, with the newly predicted value very close to observed values (70).

5.6. Conclusions

The formation reaction of OCS via four different reaction pathways in the gas phase and on a coronene surface was studied. Coronene was shown to have a catalytic influence on OCS formation reactions. Activation barriers are reduced by 62% (CO + S), 51% (CO + HS) or disappear entirely (CS + O, CS + OH), which considerably speeds up these reactions in the ISM. For two reaction pathways, CO + S and CO + HS, the reduction in activation energy is the most important role of the surface. Without this reduction, the barriers are too high and the reactions will not contribute significantly to OCS formation. All species are physisorbed, which not only reduces the activation barrier; it also allows reactants and products to diffuse on a surface, and to eventually desorb back into the gas phase. Excited oxygen and sulphur (^{1}O and ^{1}S) will be too strongly bound for further reactions to occur, as they are chemisorbed on the surface.

S + CO, reaction (1), is the most strongly catalysed reaction, with the activation barrier reduced from 18.68 kJ mol^{-1} in the gas phase to 7.09 kJ mol^{-1} on a surface, thus potentially contributing to OCS formation in the ISM. Coronene catalyses the formation of both *cis*- and *trans*-HSCO, reactions (2). The *trans*-form is strongly favoured, and assuming that the pre-exponential factors do not differ too much, no *cis*-HSCO will be formed. Once *trans*-HSCO is formed on coronene and stays adsorbed, it can react with another species, most likely a hydrogen atom, forming H_2 and OCS, or H_2S and CO, depending on how the hydrogen atom approaches the HSCO radical.

CS + O, reaction (3), is also catalysed and the submerged activation barrier in the gas phase could not be located for the surface reaction. As with reaction (4), OH + CS, the surface's main catalytic effect is now to absorb the excess formation energy, before the reaction continues to yield CO and S or CO and HS.

In the research on CO_2-formation (25), it was shown that the Eley Rideal mechanism is usually favoured over the Langmuir Hinshelwood mechanism, for two reasons. Firstly, the gas phase activation barriers are more catalysed in the ER case than they are in the LH case. Secondly, when no activation barrier is present, the diffusion barrier effectively plays this role in the LH case, where still no barrier is present in the ER case. However, because dust grains can physisorb the reactants, and because the relative abundances of sulphur bearing species is much smaller than the abundance of O, OH and water (the reactants in CO_2 formation), the LH reaction is dominant over the ER mechanism for OCS formation.

In the present research, the Langmuir Hinshelwood mechanism is the most probable one, since the activation barriers are clearly strongly catalysed and low enough to be overcome in dark, molecular clouds.

5.7. References

1. Codella, C., Viti, S., Williams, D. A., et al., *Astrophys. J.*, 2006, **644**, L41.
2. Greenwood, E., *Chemistry of the Elements*, 2001.
3. Gibb, E. L., Whittet, D. C. B., Schutte, W. A., et al., *Astrophys. J.*, 2000, **536**, 347.
4. Boogert, A. C. A., Tielens, A., Ceccarelli, C., et al., *Astron Astrophys*, 2000, **360**, 683.
5. Palumbo, M. E., Geballe, T. R. and Tielens, A., *Astrophys. J.*, 1997, **479**, 839.
6. Jefferts, K., *Astrophys. J.*, 1971, **168**, L111.
7. Codella, C., Bachiller, R., Benedettini, M., et al., *Mon. Not. R. Astron. Soc.*, 2005, **361**, 244.
8. Tielens, A., *Astron Astrophys*, 1982, **114**, 245.
9. Dartois, E., *Space Sci Rev*, 2005, **119**, 293.
10. Papoular, R., *Mon Nor R Astron Soc*, 2005, **362**, 489.
11. Phillips, T. G., Scoville, N. Z., Kwan, J., et al., *Astrophys. J.*, 1978, **222**, L59.
12. Henkel, C., *Astron Astrophys*, 1985, **150**, L25.
13. Wilson, R. W., Penzias, A. A., Wannier, P. G., et al., *Astrophys. J.*, 1976, **204**, L135.
14. Prasad, S., *Astrophys. J.*, 1983, **267**, 603.
15. van Hemert, M. and Vanhemert, *J. Chem. Phys.*, 2008, **343**, 292.
16. Millar, T. J. and Williams, D. A., Manchester, U.K., 1987.
17. Ohishi, M., Irvine, W. M. and Kaifu, N., *Iau Symposia*, 1992, 171.
18. Millar, T. J. and Herbst, E., *Astron Astrophys*, 1990, **231**, 466.
19. Ohishi, M. and Kaifu, N., *Faraday Discuss*, 1998, 205.
20. Harju, J., Winnberg, A. and Wouterloot, J. G. A., *Astron Astrophys*, 2000, **353**, 1065.
21. Geng, C. and Mu, Y., *Atmos Environ*, 2006, **40**, 1373.
22. Demello, W., *J Geophys Res*, 1994, **99**, 14601.
23. Leman, L., Orgel, L. and Ghadiri, M. R., *Science*, 2004, **306**, 283.
24. Johnson, R. D., Editon edn., Sept 2006.
25. Goumans, T. P. M., Uppal, M. A. and Brown, W. A., *Mon. Not. R. Astron. Soc.*, 2008, **384**, 1158.
26. Hall, G. E., Sivakumar, N., Houston, P. L., et al., *Phys. Rev. Lett.*, 1986, **56**, 1671.
27. Hijazo, J., *Chem. Phys. Lett.*, 1994, **222**, 15.
28. Sayós, R., Gonzalez, M. and Aguilar, A., *J. Chem. Phys.*, 1990, **141**, 401.
29. Gonzalez, M., *J. Chem. Phys.*, 1996, **105**, 10999.
30. Nickolaisen, S. L. and Cartland, H. E., *J. Chem. Phys.*, 1993, **99**, 1145.
31. Oldershaw, G. A. and Porter, D. A., *J Chem Soc Faraday Trans*, 1972, **68**, 709.
32. Rice, B. M., Cartland, H. E. and Chabalowski, C. F., *Chem. Phys. Lett.*, 1993, **211**, 283.
33. Rice, B. M. and Chabalowski, C. F., *J. Phys. Chem.*, 1994, **98**, 9488.
34. Rice, B. M., Pai, S. V. and Chabalowski, C. F., *J Phys Chem A*, 1998, **102**, 6950.
35. Slagle, I. R., Graham, R. E., Gilbert, J. R., et al., *Chem. Phys. Lett.*, 1975, **32**, 184.
36. Tsunashima, S., Yokota, T., Safarik, I., et al., *J. Phys. Chem.*, 1975, **79**, 775.
37. Lee, J. H., Stief, L. J. and Timmons, R. B., *J. Chem. Phys.*, 1977, **67**, 1705.
38. Häusler, D., Rice, J. and Wittig, C., *J. Phys. Chem.*, 1987, **91**, 5413.
39. Singleton, D., *J. Phys. Chem. Ref. Data*, 1988, **17**, 1377.
40. Lilenfeld, H. V. and Richardson, R. J., *J. Chem. Phys.*, 1977, **67**, 3991.
41. Ferrante, R., *Astrophys. J.*, 2008, **684**, 1210.
42. Liszt, H. S., Wilson, R. W., Penzias, A. A., et al., *Astrophys. J.*, 1974, **190**, 557.
43. Lo, W., *J. Chem. Phys.*, 2004, **120**, 5717.
44. Zhao, Y. and Truhlar, D. G., *J Phys Chem A*, 2004, **108**, 6908.
45. Werner, H.-J., Knowles, P. J., Lindh, R., et al., *MOLPRO, version 2006.1, a package of ab initio programmes*.
46. Frisch, M. J., Trucks, G. W., Schlegel, H. B., et al., *Gaussian, Inc., Wallingford CT*, 2004.
47. Chang, Q., *Astron Astrophys*, 2006, **458**, 497.

48. Chang, Q., Cuppen, H. M. and Herbst, E., *Astron Astrophys*, 2005, **434**, 599.
49. Greenberg, J. M., *Surf. Sci.*, 2002, **500**, 793.
50. Islam, F., Latimer, E. R. and Price, S. D., *J. Chem. Phys.*, 2007, **127**.
51. Meijer, A., Farebrother, A. J. and Clary, D. C., *J Phys Chem A*, 2002, **106**, 8996.
52. Meijer, A., Farebrother, A. J., Clary, D. C., et al., *J Phys Chem A*, 2001, **105**, 2173.
53. Meijer, A. J. H. M., Fisher, A. J. and Clary, D. C., *J Phys Chem A*, 2003, **107**, 10862.
54. Morisset, S., Aguillon, F., Sizun, M., et al., *Phys Chem Chem Phys*, 2003, **5**, 506.
55. Morisset, S., Aguillon, F., Sizun, M., et al., *J. Chem. Phys.*, 2005, **122**.
56. Rutigliano, M., Cacciatore, M. and Billing, G. D., *Chem. Phys. Lett.*, 2001, **340**, 13.
57. Williams, D. A., *Surf. Sci.*, 2002, **500**, 823.
58. Brown, W. A., Viti, S., Wolff, A. J., et al., *Faraday Discuss*, 2006, **133**, 113.
59. Mattera, L., Rosatelli, F., Salvo, C., et al., *Surface Sci*, 1980, **93**, 515.
60. Miller, J. B., Broitman, E., Michalak, W., et al., in *http://aiche.confex.com/aiche/2007/techprogram/P96062.HTM*, Editon edn.
61. Ulbricht, H., Zacharia, R., Cindir, N., et al., *Carbon*, 2006, **44**, 2931.
62. Ferro, Y., Allouche, A., Marinelli, F., et al., *Surf. Sci.*, 2004, **559**, 158.
63. Vidali, G., *Surf Sci Rep*, 1991, **12**, 133.
64. Dericbourg, J., *Surf. Sci.*, 1976, **59**, 565.
65. Matsumoto, T., *Phys Rev E*, 2008, **77**, 031611.
66. Tran, F., Weber, J., Wesolowski, T. A., et al., *J Phys Chem B*, 2002, **106**, 8689.
67. Burke, D. J., Belbin, S. and Brown, W. A., 2009.
68. Boyd, D. A., Hess, F. M. and Hess, G. B., *Surf. Sci.*, 2002, **519**, 125.
69. Sabbah, H., Biennier, L., Sims, I. R., et al., *Science*, 2007, **317**, 102.
70. Viti, S., *Personal Communication*, 2008.

Conclusions and Future Work

Chapter 6

6.1. Conclusions

The work presented here employed two models for carbonaceous dust grains, graphene and coronene, to investigate their catalytic influence on reactions of astronomical importance. A theoretical approach was chosen to calculate adsorption energies, activation barriers, pre-exponential factors and reaction rates. Two different computational programs were used, Crystal06 and Gaussian03, in each of which the best available DFT functional was chosen to reproduce long-range interactions accurately. The difference between these two functionals, PW1K and MPWB1K, was shown to be significant, but the results were still reasonably close to each other. The MPWB1K functional, a hybrid meta-GGA functional which includes the second derivative of the density, was shown to perform better than the PW1K functional, a hybrid GGA functional.

All the molecules and atoms in the ground state were shown to physisorb on the surfaces. Hydrogen-bearing molecules like water and methanol physisorb on the surfaces with the hydrogen atoms pointing towards the surface. This causes methanol to adsorb side on, and introduces an ordering in the molecules. Physisorption and chemisorption on graphene and coronene are very similar; therefore either surface can be used as a model for perfect carbonaceous dust grains.

Three different surface reactions were studied: the Langmuir Hinshelwood (LH) mechanism, where both reactants are physisorbed on the surface; the Eley Rideal (ER) mechanism, where one of the reactants is physisorbed and the second one is in the gas phase; and the Hot Atom (HA) mechanism, where one reactant is physisorbed on the surface and the second one is in the gas phase, physisorbs on the surface, but reacts before losing its adsorption energy. The ER mechanism was shown to catalyse most reactions, including $OH + H_2 \rightarrow H_2O + H$, $CO + H \rightarrow CHO$, $CH_2O + H \rightarrow CH_2OH$, $CO + {}^3S \rightarrow {}^3OCS$, $CO + HS \rightarrow c$HSCO and $CO + HS \rightarrow t$HSCO. The LH mechanism was shown to catalyse only a few reactions, including $CO + {}^3S \rightarrow {}^3OCS$. Steric hindrance forces the transition state on the surface to take a different, less favourable geometry than in the gas phase, which works against catalysis. The HA mechanism was only investigated in the carbonyl sulfide research and was shown to catalyse the reactions even more than was already the case for the ER mechanism.

Even though the LH mechanism does not substantially reduce most activation barriers, it is still the most probable reaction in the interstellar medium (ISM). The gas phase density is extremely low in dark molecular clouds, only ~ 10^4 species cm^{-3}, and for this reason the probability of two reactants encountering each other and reacting is much higher on the surface. Calculations of the ratio of reaction versus the ratio of desorption have shown that, with more than 20 orders of magnitude difference, the LH mechanism dominates over the ER mechanism for e.g. the water formation reaction ($OH + H_2 \rightarrow H_2O + H$), and the OCS forming reactions.

The catalysis by the surfaces can be separated into two different contributions. For both coronene and graphene, physisorption through pure van der Waals forces is present. For graphene however, the difference in energy between the occupied and unoccupied orbitals, the HOMO and the LUMO, is 0 kJ mol^{-1}. Thus, a very efficient overlap of orbitals with any species physisorbed on graphene is possible, with graphene able to accommodate additional electrons or even to donate electrons back to orbitals of the adsorbate. The gap between the HOMO and the LUMO of coronene was calculated to be around 500 kJ mol^{-1}, which does not allow for this effect. The band gap of PAHs decreases with increasing size, thus larger PAHs can probably catalyse the reactions more efficiently. Based on previous results from our group (1, 2), it is believed that polar or charged surfaces may have a stronger catalytic influence.

6.2. Future Work

Research never truly finishes and during the course of this investigation, many other research possibilities arose, which could promise to be of major importance to both the chemical and the astronomical communities.

In this work, perfect graphite and coronene were used as models for dust grains. Even though both structures are valid models for interstellar carbonaceous dust grains, it is very unlikely that these grains are exclusively built up from 'perfect' structures. In fact, given that the atom density in the ISM is very low (~ 10,000 atoms cm^{-3} in dark molecular clouds), it is very probable that defects are ubiquitous on dust grains, without getting annealed. Hence the models used here could be improved by introducing defects.

Defects can come in many different shapes and forms; they can be classified as deformations, adatoms, vacancies, charge defects, and combinations thereof. Deformations of a surface will not change the chemical formula of this surface, but will change the relative orientation of atoms with respect to each other. The 5,7,7,5 defect (via Stone-Wales deformation) has been observed previously in the formation of carbon nanotubes, but is rather unstable in a stressless graphitic system (3, 4). Other deformations include the 5,7 defect, the 5,8,5 defect (divacancy) and the lip-lip interaction (folding).

Adatoms and vacancies are similar defects from a different angle. When considering graphite, vacancy formation requires energies of over 700 kJ/mol (3). Preliminary investigations were performed on vacancy annihilation with hydrogen atoms. A defective graphene sheet was created by removing one carbon atom. The resulting structure does not create a 5-membered ring structure, which would be expected, but instead keeps its vacancy, in agreement with previous research on large polycyclic aromatic hydrocarbons (5).

Hydrogenation of this defect with hydrogen atoms is barrierless, and continues until the entire defect is annealed. The carbon atom which was removed had 4 bonds, thus 4 hydrogen atoms can sequentially hydrogenate the surface and entirely remove this vacancy. Every single hydrogenation step is barrierless, which suggests that, since hydrogen is available in the ISM, vacancies will be hydrogenated and a PAH will be created from a defective graphene surface. A similar procedure is expected to happen for adatoms, eventually either removing light hydrocarbons (e.g. a carbon adatom will be hydrogenated to form CH_4), or forming a PAH layer on top of the graphene sheet.

Dust grains may be negatively charged, and a charge defect has been investigated very briefly during the research of OCS on coronene. Sulfur however migrated on the coronene surface, to form a six-membered ring with two of coronene's hydrogen atoms, and three carbon atoms. This effect was seen for both the sulphur atom (^3S), and for HS. Other authors have already shown that edge effects of coronene or graphene play an important role (6), but since this is an effect which was not considered relevant to this study, charged species were not investigated further. A larger PAH would have to be used to calculate reactions involving charged species, i.e. ovalene or circumcoronene (resp. $C_{32}H_{14}$ and $C_{54}H_{18}$, both molecules are closely related to coronene). Graphene can unfortunately not be used as a charged surface, due to charge problems for periodic systems. However, charges will be delocalised over the entire PAH conjugated ring system (7), therefore these reactions are considered to be of lesser importance than when the charge is localised, as is the case on e.g. siliceous surfaces (1).

6.3 References

1. Goumans, T. P. M., Catlow, C. R. A. and Brown, W. A., *J Phys Chem C*, 2008, **112**, 15419.
2. Goumans, T. P. M., Wander, A., Catlow, C. R. A., et al., *Mon. Not. R. Astron. Soc.*, 2007, **382**, 1829.
3. Li, L., Reich, S. and Robertson, J., *Phys Rev B*, 2005, **72**.
4. Bernholc, J., Brabec, C., Nardelli, M. B., et al., *Appl Phys A - Matter*, 1998, **67**, 39.
5. Forte, G., Grassi, A., Lombardo, G. M., et al., *Phys. Lett. A*, 2008, **372**, 6168.
6. Rauls, E. and Hornekaer, L., *Astrophys. J.*, 2008, **679**, 531.
7. Jelea, A., Marinelli, F., Ferro, Y., et al., *Carbon*, 2004, **42**, 3189.